

Mass reconstruction techniques and
cross section measurement for
 $Z \rightarrow \tau\tau \rightarrow e\mu + 4\nu$
with the ATLAS experiment

DISSERTATION

zur Erlangung des akademischen Grades

Doctor rerum naturalium
(Dr. rer. nat.)

vorgelegt

der Fakultät Mathematik und Naturwissenschaften
der Technischen Universität Dresden

von

Dipl.-Phys. Kathrin Kormoll (geb. Leonhardt)

geboren am 24. 01. 1985 in Karl-Marx-Stadt
(jetzt Chemnitz)

eingereicht am 07. Januar 2013

verteidigt am 25. Februar 2013

Die Dissertation wurde in der Zeit von 01/2009 bis 12/2012 am
Institut für Kern- und Teilchenphysik der TU Dresden angefertigt.

1. Gutachter: Prof. Dr. M. Kobel
2. Gutachter: Prof. Dr. D. Stöckinger

Kurzdarstellung

Die Suche nach dem Higgs Boson ist ein zentraler Forschungsschwerpunkt der modernen Teilchenphysik. Zum einen ist das Higgs Boson das einzige bislang unentdeckte Teilchen des Standard Modells. Zum anderen gibt seine mögliche Entdeckung eine bessere Einsicht in die Natur neuer Physik. Mit der Inbetriebnahme des Large Hadron Colliders, LHC, am europäischen Kernforschungszentrum CERN bei Genf konnten Proton-Proton Kollisionen mit bislang unerreichten Schwerpunktsenergien von $\sqrt{s} = 7$ TeV beziehungsweise $\sqrt{s} = 8$ TeV erzielt werden.

In der vorliegenden Arbeit wird die Messung des Wechselwirkungsquerschnitts $pp \rightarrow Z^0/\gamma^* \rightarrow \tau^+\tau^-$ im gemischten leptonischen Endzustand mit Daten des ATLAS Detektors durchgeführt. Der Zerfall der kohärenten Summe aus Photon, γ^* , und Z^0 Boson in zwei τ -Leptonen ist ein irreduzibler Untergrund von Higgs Boson Zerfällen in zwei τ -Leptonen. Eine genaue Kenntniss des Massenspektrums sowie dessen Normierung ist deswegen für die Higgs Boson Suche essentiell. Die verwendeten Daten entsprechen einer integrierten Luminosität von $L = 35.51 \text{ pb}^{-1}$ bei einer Schwerpunktsenergie von $\sqrt{s} = 7$ TeV. Die Messung erzielt einen Wechselwirkungsquerschnitt von $\sigma_{Z/\gamma^*}^{\text{tot.}} \times \text{BR}(Z \rightarrow \tau\tau) = (1041 \pm 143 \pm 74 \pm 35) \text{ pb}$. Die angegebenen Unsicherheiten entsprechen den statistischen, den systematischen und den Unsicherheiten aus Luminositätsmessungen. Das Ergebnis stimmt mit dem theoretisch bestimmten Wert sowie dem Ergebnis anderer Experimente innerhalb seiner Unsicherheiten überein.

Im zweiten Teil der Arbeit werden verschiedene Massenrekonstruktionsmethoden von Zerfällen in zwei τ -Leptonen untersucht. Die Analyse konzentriert sich dabei auf Higgs Bosonen, ϕ , der minimalen supersymmetrischen Erweiterung des Standard Modells; insbesondere auf deren Zerfall in zwei τ -Leptonen und weiter in den gemischten leptonischen Endzustand, $\phi \rightarrow \tau^+\tau^- \rightarrow e\mu + 4\nu$. Die untersuchten Massenrekonstruktionsmethoden sind die sichtbare Masse, die effektive Masse, sowie die früh- und spät-projizierte transversale Masse. Weiterhin werden Abhängigkeiten der Massenverteilungen vom transversalen Impuls der Leptonen des Endzustandes, sowie der fehlenden transversalen Energie festgestellt. Eine Abhängigkeit vom transversalen Impuls des energiereichsten Jets hingegen konnte nicht nachgewiesen werden. Eine mögliche Eliminierung der Variablenabhängigkeiten wird untersucht, zeigt jedoch dass sie zu einer schlechteren Trennung zwischen Signal und Untergrundprozessen sowie einer schlechteren Auflösung unterschiedlicher Higgs Boson Massen führt. Mit der Kalibrierung der berechneten Massen der verschiedenen Rekonstruktionstechniken wird die Arbeit abgeschlossen.

Abstract

A central aspect of modern particle physics is the search for the Higgs boson. First, the Higgs boson remains the only particle of the Standard Model not being proven experimentally. Secondly, its possible observation may improve our understanding of new physics. With the start of operation of the LHC at the European Organization for Nuclear Research (CERN), proton-proton collisions with a centre of mass energy being as high as $\sqrt{s} = 7$ TeV and $\sqrt{s} = 8$ TeV could be achieved

This work measures the cross section of the process $pp \rightarrow Z^0/\gamma^* \rightarrow \tau^+\tau^-$ in the mixed leptonic final state with data of the ATLAS detector. The decay of the coherent sum of the photon, γ^* , and the Z^0 boson is an irreducible background for Higgs boson decays into two τ -leptons. For the Higgs boson search a precise knowledge of its mass spectrum and its normalisation is essential. The data used are equal to an integrated luminosity of $L = 35.51 \text{ pb}^{-1}$ with a centre of mass energy of $\sqrt{s} = 7$ TeV. A cross section of $\sigma_{Z/\gamma^*}^{\text{tot.}} \times \text{BR}(Z \rightarrow \tau\tau) = (1041 \pm 143 \pm 74 \pm 35) \text{ pb}$ is yielded, with its statistical and systematic uncertainties as well as uncertainties from luminosity determination. The result is compatible with the results from theoretical calculations and that from other experiments within their uncertainties.

The second part of this work examines mass reconstruction methods of decays into two τ -leptons. The analysis concentrates on Higgs bosons, ϕ , of the minimal supersymmetric extension of the Standard Model, the MSSM. In particular, the decay of Higgs bosons to two τ -leptons and further into an electron, a muon and four neutrinos is examined, $\phi \rightarrow \tau^+\tau^- \rightarrow e\mu + 4\nu$. The appropriate mass reconstruction techniques being investigated are the visible mass, the effective mass and the early and late projected transverse mass. Furthermore, a dependency of the mass distributions on the transverse momentum of the leptons and on the missing transverse energy is observed. However, a dependency on the transverse momentum of the highest p_T jet was not found. The elimination of the variable dependencies leads to a worse separation power between the signal and background processes as well as a worse resolution between different Higgs boson masses. The work concludes with a calibration of the masses calculated with the analysed mass reconstruction techniques.

Table of Contents

1	Introduction	1
2	Theoretical framework	3
2.1	The Standard Model of particle physics	3
2.1.1	Phenomenological overview	3
2.1.2	Electroweak theory	6
2.1.3	The Higgs mechanism	7
2.2	Supersymmetry	9
2.2.1	The MSSM	10
2.3	Experimental limits on the Higgs boson mass	11
3	Monte Carlo event generation and detector simulation	13
3.1	Monte Carlo event generation	13
3.2	Detector simulation	15
4	The ATLAS experiment at the LHC	17
4.1	The Large Hadron Collider	17
4.1.1	Injection Chain	18
4.1.2	Beam conditions	19
4.2	The ATLAS detector	21
4.2.1	The magnet system	23
4.2.2	The inner tracking system	23
4.2.3	The calorimetry system	25
4.2.4	The Muon Spectrometer	29
4.3	Trigger system	30
4.4	Luminosity determination	31
4.5	Particle reconstruction	32
4.5.1	Electron candidates	32
4.5.2	Muon candidates	35
4.5.3	Heavy lepton candidates	35
4.5.4	Jet reconstruction	35
4.5.5	Transverse missing energy	36
5	Observation and Cross section measurement	39
5.1	Motivation	39
5.2	Signal and background processes	40
5.2.1	Signal process	40

5.2.2	Physics background	43
5.2.3	Monte Carlo simulation	45
5.3	Analysis strategy	45
5.4	Experimental data and quality criteria	47
5.5	Object selection	48
5.6	Event selection	51
5.6.1	Vertex multiplicity	51
5.6.2	Trigger	51
5.6.3	Jet cleaning	51
5.6.4	Selection of a lepton pair	53
5.6.5	Electron energy scale correction	54
5.6.6	Isolation of leptons	55
5.6.7	Monte Carlo corrections	59
5.6.8	Rejection of W + jets events	65
5.6.9	Rejection of top-quark pair events	67
5.6.10	Visible mass window	67
5.7	Cut summary	68
5.8	Estimation of background processes from data	71
5.8.1	QCD multijet processes	71
5.8.2	Electroweak processes	75
5.8.3	Background from top-quark pairs	77
5.9	Determination of the cross section	84
5.10	Systematic uncertainties	86
5.10.1	Uncertainty on signal and background events	86
5.10.2	Uncertainty on the correction factor	92
5.10.3	Uncertainty on the acceptance factor	92
5.11	Results	94
5.11.1	Observation	94
5.11.2	Cross section measurement	94
5.12	Discussion	95
5.12.1	Comparison with other ATLAS results	97
6	Comparison of mass reconstruction techniques	99
6.1	Motivation	99
6.2	Mass reconstruction methods	100
6.2.1	Visible mass	100
6.2.2	Effective mass	101
6.2.3	Projected transverse mass	101
6.3	Signal and background processes	103
6.3.1	Signal process	103
6.3.2	Background processes	105
6.4	Selection strategy	106
6.4.1	Object selection	106
6.4.2	Event Selection	107

6.5	Comparison of mass reconstruction methods	109
6.6	Variable dependence	112
6.6.1	Dependency on event variables	112
6.6.2	Elimination of variable dependence	117
6.7	Calibration	121
6.8	Discussion	124
A	Cross section measurement	125
A.1	Monte Carlo corrections	125
A.2	Systematic uncertainty of the method for QCD multijet estimation .	126
B	Comparison of mass reconstruction techniques	129
B.1	Dependency on event variables	129
B.2	Elimination of variable dependence	133

1 Introduction

The question “What is matter built of?” has concerned mankind for several thousand years. During the last century a theory was formed, describing the smallest building blocks of matter, the elementary particles, and the forces they interact through. They are combined in the Standard Model of elementary particle physics. This theory includes the electromagnetic force, the weak and the strong force, as well as leptons and quarks. The Standard Model has been tested and confirmed at a high level of precision in numerous experiments. The only missing element of the Standard Model is the observation of the Higgs boson, responsible for the masses of particles. Although being extremely successful, several open questions remain which cannot be answered satisfyingly with the Standard Model. Instead they indicate new physics beyond the Standard Model.

With the start of stable operation of the LHC in 2010 new opportunities arose in particle physics experiments. The world’s largest particle accelerator was originally designed to collide protons at a centre of mass energy of 14 TeV. In the beginning phase the centre of mass energy was set to 7 TeV for 2010 and 2011 and to 8 TeV for 2012. The LHC was built to discover the Standard Model Higgs boson or physics beyond the Standard Model like supersymmetric particles. In 2012 the two all-purpose detectors at the LHC, the ATLAS and the CMS detector, observed a new boson at a mass of $m \approx 126$ GeV which is consistent with the expected signal of a Standard Model Higgs boson [1–4]. Following measurements need to show whether the observed boson really is the Higgs boson as predicted by the Standard Model. The observed boson might also be one of the predicted Higgs bosons from supersymmetric theories or even a different new physics phenomenon.

This work is separated into two parts. In the first part of this work, the cross section of the process $pp \rightarrow Z^0/\gamma^* \rightarrow \tau^+\tau^- \rightarrow e\mu + 4\nu$ is measured with data collected by the ATLAS detector. This process is a direct and irreducible background for the Higgs boson decay into two τ -leptons. For this reason, its differential mass spectrum and normalisation have to be known precisely and must be well understood for searches of new physics. The measurement further offers the possibility to test Standard Model predictions by comparison to theoretical calculations of production cross sections and other measurements. The analysis concentrates on the mixed-leptonic decay into an electron, a muon and four neutrinos. Furthermore, it is restricted to the mass range of the intermediate vector boson of $66 \text{ GeV} \leq m \leq 116 \text{ GeV}$. The analysis covers the early phase of ATLAS data taking, using data equal to an integrated luminosity of $L = 35.51 \text{ pb}^{-1}$ at a centre of mass energy of $\sqrt{s} = 7 \text{ TeV}$.

The second part of this work concentrates on the comparison of different mass reconstruction techniques of decays into τ -lepton pairs. For this, simulated events of Higgs boson decays within the supersymmetric theory are used. The separation of Higgs boson and background mass distributions is analysed. Furthermore, the dependency on event variables and its elimination is investigated. The results will help future Higgs boson searches in the $\tau^+\tau^-$ -decay channel.

This thesis starts with an introduction of elementary particle physics of the Standard Model and the Higgs mechanism. Furthermore, Supersymmetry is described as well as the minimal supersymmetric extension of the Standard Model, the MSSM. The chapter concludes with experimental limits being set on the Higgs boson mass. The second chapter gives an overview on the Monte Carlo event generation and the simulation of the ATLAS detector. In the third chapter the technical details of the LHC and the ATLAS detector are described. This includes the trigger system and the luminosity determination of the ATLAS detector as well as the reconstruction of objects from detector signals. Chapter 4 specifies the cross section determination of the process $pp \rightarrow Z^0/\gamma^* \rightarrow \tau^+\tau^- \rightarrow e\mu + 4\nu$. In particular, the analysis strategy with its object and event selection and the accomplished calculation of the cross section is emphasised. Furthermore, the estimation of background processes from data is described in detail. The results of the analysis are being compared to the theoretical value as well as to other experimentally gained results. The last chapter of this thesis concentrates on the comparison of different mass reconstruction techniques for the invariant mass of $\tau^+\tau^-$ final states, $m_{\tau\tau}$. After the introduction of the methods, the selection strategy for MSSM Higgs boson decays into two τ -leptons follows. Subsequently, the mass distributions are compared quantitatively and their dependency on event variables is examined. The chapter concludes with the possible elimination of the variable dependencies and the calibration of the gained masses.

2 Theoretical framework

2.1 The Standard Model of particle physics

2.1.1 Phenomenological overview

The Standard Model of elementary particle physics involves three of the known four forces together with a content of 12 particles plus their anti-particles and 6 bosons. The Standard Model is the best tested model describing the interactions of particles with high precision. It is described as a quantum field theory based on the gauge symmetry $SU(3)_C \times SU(2)_L \times U(1)_Y$.

The particle content can be divided into particles with half-integer spin and integer spin¹. The first are denoted as fermions. They deliver the building blocks of matter. The latter are gauge bosons with a spin of $s = 1$. The gauge bosons are force carriers, responsible for the interaction of particles. This interaction is a direct consequence of local gauge symmetries. The forces being described within the Standard Model are the electromagnetic, the weak and the strong force. Their force carriers are the massless photon, γ , the massive W^\pm and Z^0 bosons and the eight massless gluons, g_k with $k \in \{1 \dots 8\}$, respectively. Table 2.1 gives an overview of the gauge bosons, their mass and the range of the appropriate force.

Table 2.1: Gauge bosons of the Standard Model of elementary particle physics with their experimentally measured mass and the range of the appropriate force. [5].

force	boson	mass	range
electromagnetic	γ	$< 1 \cdot 10^{-18} \text{ eV}$	∞
weak	W^\pm	$80.40 \pm 0.02 \text{ GeV}$	$\approx 10^{-18} \text{ m}$
weak	Z^0	$91.188 \pm 0.002 \text{ GeV}$	$\approx 10^{-18} \text{ m}$
strong	g_k	$< 7 \cdot 10^{-32} \text{ eV}$	$\approx 10^{-15} \text{ m}$

The fermionic content of the Standard Model is divided into leptons and quarks. They are fundamental point-like particles. Quarks are the only fermions which interact through the strong force, meaning that they carry so-called colour charge.

¹The spin is given in units of \hbar . Nevertheless, in elementary particle physics the Planck's constant, \hbar , as well as the velocity of light, c , is set to one and therefore unitless; $\hbar = c = 1$. With this, the mass, momentum, and energy all have units of electron volts. This is also applied to this work.

Furthermore, they have an electric charge² of either $2/3$, which are denoted as up-type quarks, or $-1/3$, the down-type quarks. Their mass ranges from some MeV for the up- and the down-quark, to some GeV for the charm-, the strange- and the bottom-quark and finally to the order of ~ 100 GeV for the top-quark. The ensemble of leptons is divided into particles with electric charge and electrically neutral particles. The first mentioned are the electron, e^- , the muon, μ^- , and the τ^- -lepton. All of them have an electric charge of -1 . To each of the electrically charged leptons an electrically neutral neutrino can be assigned. These are the electron neutrino, ν_e , the muon neutrino, ν_μ , and the τ -neutrino, ν_τ . Within the Standard Model of elementary particle physics they are massless. However, in neutrino oscillation experiments it was proven, that their mass is non-zero [6]. Measurements based on the β -decay, cosmological nucleosynthesis and other cosmological data can set upper limits on their mass [5].

All fermions of the Standard Model carry a weak charge. They are grouped into families, each containing an electrically charged lepton, its corresponding neutrino and a pair of quarks. Presently, three families are known. Nonetheless, there are investigations ongoing considering a fourth family [7, 8]. All particles matter is built of belong to the first family. The total fermionic content is presented in table 2.2 with its electric charge and its experimentally measured mass. To each of the fermions there exists an anti-particle. Its attributes are characterised by the opposite of the particle's quantum numbers but the same mass. Neutrinos, however, play a special role. Depending on the underlying model, neutrinos can be described as their own anti-particle, i.e. Majorana particles, in contrast to Dirac particles which have distinct anti-particles. Experiments were not successful yet in verifying or falsifying one of the theories.

Table 2.2: Fermionic content of the Standard Model of elementary particle physics with its electric charge and its experimentally measured mass [5].

family	leptons	el. charge	mass	quarks	el. charge	mass
I	ν_e	0	< 2 eV	u	$+2/3$	$2.3^{+0.7}_{-0.5}$ MeV
	e^-	-1	511 keV	d	$-1/3$	$4.8^{+0.7}_{-0.3}$ MeV
II	ν_μ	0	< 2 eV	c	$+2/3$	1.275 ± 0.025 GeV
	μ^-	-1	105.6 MeV	s	$-1/3$	95 ± 5 MeV
III	ν_τ	0	< 2 eV	t	$+2/3$	173.5 ± 1 GeV
	τ^-	-1	1.78 GeV	b	$-1/3$	4.18 ± 0.03 GeV

The electromagnetic force is mediated by the massless photon³. Its range is therefore infinite. Photons can be mediated among particles carrying an electric charge. This is a characteristic for gauge fields, which means that the interaction of gauge bosons with fermions or gauge bosons is governed by their charges. Consequently,

²The electric charge is given in units of the electron charge.

³Measurements give an upper limit on the photon mass of $< 10^{-18}$ eV [5].

the photon interacts with all quarks as well as with electrons, muons and τ -leptons. Also the gauge bosons W^\pm carry an electric charge, whereas the photon itself does not carry any charge, meaning that there is no self-coupling. The coupling strength of the electromagnetic force is given by the coupling constant $\alpha = e^2/4\pi$, where e is the electromagnetic coupling constant. At low energies, the Thomson limit, the value of α is given by the fine structure constant $\alpha \approx 1/137$. Since its value is dependent on the energy scale Q of the interaction, α is a so-called running coupling constant, $\alpha(Q)$. This fact is valid for all coupling constants of the Standard Model.

The gauge bosons of the weak force are the massive Z^0 and W^\pm bosons⁴. Because of their comparatively high mass, the range of the weak force is limited to $\approx 10^{-18}$ m. The coupling constant can be calculated as $\alpha_W = g_W^2/4\pi$. At energies much lower than the mass of their gauge bosons, the weak coupling constant has a value of $\alpha_W \approx 1/30$. Gauge bosons of the weak force couple to particles having a charge corresponding to the weak isospin I . All fermions carry a weak charge. The character of the interaction is of vector minus axial-vector type. Consequently, the gauge bosons of the weak force interact only with left-handed chiral fermions and right-handed chiral anti-fermions. The electromagnetic and the weak forces can be combined to the electroweak theory. Its underlying symmetry group is of the character $SU(2)_L \times U(1)_Y$, where $U(1)_Y$ is the symmetry group of the weak hypercharge and $SU(2)_L$ the symmetry group of the weak isospin. With the Gell-Man Nishijima formula a correlation between the electric charge, the third component of the weak charge, I_3 , and the hypercharge, Y , can be formulated:

$$Q = I_3 + \frac{Y}{2}. \quad (2.1)$$

The strong force is mediated through massless⁵ gluons, g_k with $k \in \{1 \dots 8\}$. They couple to particles having a colour charge. These are in particular the quarks. However, also the gluons carry colour charge, leading to self-coupling. This fact is responsible for the so-called confinement, which says that quarks cannot be regarded as free particles at scales larger than the hadron diameter, which is the inverse of $\Lambda_{QCD} = 200$ MeV. At these energy scales the strong coupling constant is approximately $\alpha_s = g_s^2/4\pi \approx 1$. This sets the range of the strong force to approximately $\approx 10^{-15}$ m. At small distances on the other hand, asymptotic freedom takes control, reducing α_s to a nearly vanishing value, where quarks can be regarded as free particles. Due to the confinement, quarks and gluons appear in nature only in the form of hadrons. They are referred to as partons.

The theoretical formulation of the Standard Model is based on gauge invariance. The formulation of this quantum field theory is achieved with a Lagrange density,

⁴The mass distributions of the Z^0 and W^\pm bosons have a finite width. This arises the possibility of interactions happening with the mass of the gauge bosons different than the peak of the mass distribution. These bosons are called off-shell, while the respective gauge bosons of nominal mass are called on-shell.

⁵Measurements set an upper limit on the gluons' mass of $< 7 \cdot 10^{-32}$ eV [5].

combining interaction fields as well as terms of propagating particles. Such a formulation connects the theory of special relativity and quantum mechanics. The Lagrangian is formulated as follows:

$$\mathcal{L}_{SM} = \mathcal{L}_{EW} + \mathcal{L}_{QCD} + \mathcal{L}_{Higgs} + \mathcal{L}_{Yukawa} . \quad (2.2)$$

Its individual terms describe the electroweak theory, \mathcal{L}_{EW} , Quantum Chromodynamics, \mathcal{L}_{QCD} , the gauge theory of the strong force, and the formulation of mass terms for fermions and gauge bosons, $\mathcal{L}_{Higgs} + \mathcal{L}_{Yukawa}$.

2.1.2 Electroweak theory

The electroweak theory is a gauge theory combining Quantum Electrodynamics with the weak force. It can be described with the $U(1)_Y \times SU(2)_L$ symmetry group with $U(1)_Y$ being the symmetry group of the weak hypercharge and $SU(2)_L$ the symmetry group of the weak isospin. Whereas the former symmetry group applies to all fermions, the latter affects only the left-handed chiral components of a spinor⁶, Ψ_L . The fermionic content of the Standard Model is therefore formulated as left-handed chiral doublets, having a weak isospin of $I_3 = \pm 1/2$, and right-handed chiral singlets with $I_3 = 0$. It is presented in table 2.3 with the weak isospin and hypercharge quantum numbers⁷. The generator of the $U(1)_Y$ group is denoted as Y with its gauge field B_μ and its coupling constant g_1 . The generator of the $SU(2)_L$ group are \vec{T} with their three gauge fields W_μ^k , $k = 1, 2, 3$, and the coupling constant g_2 .

Table 2.3: Quantum numbers of the fermionic content of the Standard Model displayed as electroweak multiplets.

families						
I	II	III	$ \vec{T} $	I_3	Q	Y
$\begin{pmatrix} \nu_{eL} \\ e_L^- \end{pmatrix}$	$\begin{pmatrix} \nu_{\mu L} \\ \mu_L^- \end{pmatrix}$	$\begin{pmatrix} \nu_{\tau L} \\ \tau_L^- \end{pmatrix}$	1/2	$\begin{pmatrix} +1/2 \\ -1/2 \end{pmatrix}$	0	-1
			1/2		-1	-1
ν_{eR}	$\nu_{\mu R}$	$\nu_{\tau R}$	0	0	0	0
e_R^-	μ_R^-	τ_R^-	0	0	-1	-2
$\begin{pmatrix} u_L \\ d_L' \end{pmatrix}$	$\begin{pmatrix} c_L \\ s_L' \end{pmatrix}$	$\begin{pmatrix} t_L \\ b_L' \end{pmatrix}$	1/2	$\begin{pmatrix} +1/2 \\ -1/2 \end{pmatrix}$	+2/3	+1/3
			1/2		-1/3	+1/3
u_R	c_R	t_R	0	0	+2/3	+4/3
d_R'	s_R'	b_R'	0	0	-1/3	-2/3

⁶A spinor, Ψ , can be separated into a left-handed chiral component and a right-handed chiral component with the projection operators P_L and P_R : $\Psi_L = P_L \Psi$ and $\Psi_R = P_R \Psi$.

⁷The quarks listed in the table represent the flavour eigenstates.

The Lagrangian of the electroweak theory is formulated as follows:

$$\mathcal{L}_{EW} = i\bar{\Psi}_L\gamma^\mu D_\mu\Psi_L + i\bar{\Psi}_R\gamma^\mu D_\mu\Psi_R - \frac{1}{4}W_{\mu\nu}^k W^{k,\mu\nu} - \frac{1}{4}B_{\mu\nu}B^{\mu\nu} \quad (2.3)$$

Hereby, Einstein's sum convention must be followed. D_μ is the covariant derivative of this particular symmetry group. It is formulated as:

$$D_\mu = \partial_\mu + ig_1 \frac{Y}{2} B_\mu + ig_2 W_\mu^k I_k. \quad (2.4)$$

The experimentally observed gauge bosons of the weak and the electromagnetic force can be introduced by linear combinations of the gauge fields B_μ and W_μ^k , $k = 1, 2, 3$. With the weak mixing angle θ_W the charged bosons W^\pm are described through:

$$W_\mu^\pm = \sqrt{\frac{1}{2}}(W_\mu^1 \mp iW_\mu^2), \quad (2.5)$$

while the electrically neutral gauge bosons are represented by:

$$A_\mu = B_\mu \cos \theta_W + W_\mu^3 \sin \theta_W \quad (2.6)$$

$$Z_\mu = -B_\mu \sin \theta_W + W_\mu^3 \cos \theta_W. \quad (2.7)$$

The quanta of the field A_μ can be associated with the photon, that of the field Z_μ with the Z^0 boson.

2.1.3 The Higgs mechanism

Any introduction of mass terms for either fermions,

$$\mathcal{L}_{fermion\ mass} \propto m\bar{\Psi}\Psi,$$

or bosons,

$$\mathcal{L}_{boson\ mass} \propto M^2 V^\mu V_\mu,$$

with $V \in \{W^k, B\}$, would destroy local gauge invariance. Nonetheless, experiments have shown that the mentioned particles indeed have masses ranging from 511 keV for the electron to some ~ 100 GeV for the top-quark. Mass terms can be formulated through the mechanism of the spontaneous symmetry breaking. For this, an $SU(2)_L$ doublet of complex scalar fields is introduced:

$$\phi = \begin{pmatrix} \phi_\alpha \\ \phi_\beta \end{pmatrix} = \sqrt{\frac{1}{2}} \begin{pmatrix} \phi_1 + i\phi_2 \\ \phi_3 + i\phi_4 \end{pmatrix}. \quad (2.8)$$

This field is commonly called the Higgs-field [9–12]. The Lagrangian of the field is given as:

$$\mathcal{L}_{Higgs} = (D_\mu\phi)^\dagger(D^\mu\phi) - V(\phi), \quad (2.9)$$

where D_μ is the covariant derivative of the $U(1)_Y \times SU(2)_L$ symmetry group, defined in equation (2.4). The hypercharge is chosen such that the upper component of the doublet (2.8) carries a positive electric charge, whereas the lower component is electrically neutral. This Lagrange density is naturally gauge invariant. The first term describes the interaction of the Higgs field with other gauge fields, whereas the second term represents the potential, equal to the energy yield of the Lagrangian. It is formulated in terms of two parameters:

$$V(\phi) = -\mu^2 \phi^\dagger \phi + \lambda (\phi^\dagger \phi)^2, \quad (2.10)$$

with the particular choice $\lambda > 0$. Through $\partial V / \partial \phi = 0$ the minimum of the potential is found to be:

$$|\phi_{min}| = \begin{cases} 0 & \text{for } \mu^2 \leq 0 \\ \sqrt{\frac{\mu^2}{2\lambda}} \equiv \frac{v}{\sqrt{2}} & \text{for } \mu^2 > 0 \end{cases} \quad (2.11)$$

For values $\mu^2 \leq 0$ the vacuum expectation value $\langle 0 | \phi | 0 \rangle$ is zero, making the ground-state of the Higgs field invariant under $U(1)_Y \times SU(2)_L$ transformation. Values of $\mu^2 > 0$ lead to a non-zero vacuum expectation value $v = \mu / \sqrt{\lambda}$, violating the $U(1)_Y \times SU(2)_L$ symmetry or in other words leads to spontaneous symmetry breaking. Since no Higgs field of positive electric charge is observed, the ground state has to be:

$$\phi_0 = \frac{1}{\sqrt{2}} \begin{pmatrix} 0 \\ v \end{pmatrix}. \quad (2.12)$$

An expansion of the Higgs field around its minimum leads to four real scalar fields. Three of them represent massless Goldstone boson fields, which can be linked to the weak gauge bosons and the photon. As the Lagrangian is now locally $SU(2)$ invariant, a gauge rotation is possible, leading to extra degrees of freedom which can be associated with the masses of the weak gauge bosons. The photon remains massless. The mass terms are written as:

$$m_{W^\pm} = \frac{1}{2} v g_2 \quad (2.13)$$

$$m_{Z^0} = \frac{1}{2} \sqrt{g_1^2 + g_2^2} \cdot v. \quad (2.14)$$

The fourth scalar field of the expansion, $h(x)$, remains. It is called the Higgs-field, whose excitation is a massive gauge boson of the mass $m_H = v \sqrt{2\lambda}$. The so-called Higgs boson is a neutral scalar particle and appears to have cubic and quartic self-couplings. Interactions of the Higgs field with the gauge fields lead to masses of gauge bosons and fermions. The latter interactions need to be included into the Lagrangian of the Standard Model manually. This is achieved by adding Yukawa terms as done in equation (2.2). Hereby, the masses of the fermions are proportional to the Higgs coupling to fermions, λ_f :

$$m_f = \lambda_f \frac{v}{\sqrt{2}}. \quad (2.15)$$

Presently, only limits were set on the Higgs boson mass, making the Higgs boson the only missing particle of the Standard Model of elementary particle physics.

2.2 Supersymmetry

The Standard Model of elementary particle physics describes the interaction of particles with high precision and even predicted the existence of several high-mass particles which were discovered in experiments. Still, there are a lot of open questions remaining which cannot be answered by the Standard Model. On the one hand, several experimental observations are not included. In particular, the Standard Model

- cannot explain the neutrino masses being verified in neutrino oscillation experiments,
- does not incorporate the theory of gravitation, which is based on general relativity,
- does not involve any dark matter candidate or dark energy as deduced from observational cosmology,
- cannot explain the matter-antimatter asymmetry.

On the other hand there arise unresolved questions from the theoretical point of view. First of all, the Standard Model depends on 19 numerical parameters, which need to be determined experimentally. Presently, no theory could be formulated predicting the parameters. Then, the strong interaction is found to be CP-invariant, contrary to the weak interaction. However, the Lagrangian of QCD naturally contains terms resulting into CP violation. A fine tuning which makes this term vanish is considered as unnatural. A further question concerns the mass of the Higgs boson, which is much lighter than the Planck scale, $m_{Planck} \approx 10^{19}$ GeV, c.f. section 2.3. For energies reaching the Planck scale, higher order loop corrections are proportional to $\sim m_{Planck}^2$. In contrast, the mass of the Higgs boson ought to be independent of the scale. This problem is known as the hierarchy problem.

These and further questions suggest the formulation of other theories beyond that of the Standard Model in order to resolve the issues mentioned and reducing the number of free parameters.

One of the theoretically favoured candidates for physics beyond the Standard Model is the Supersymmetry (SUSY). As described, the motivation of this theory is to protect the mass of the Higgs boson from quadratically diverging corrections. This leads to a theory which postulates invariance under a symmetry transforming bosons into fermions and vice versa. New generators, Q_α and \bar{Q}_α , are introduced which commute with the $SU(3)_C \times SU(2)_L \times U(1)_Y$ symmetry groups of the Standard Model. They transform fermions to bosons and bosons to fermions:

$$Q_\alpha |F\rangle \propto |B\rangle \tag{2.16}$$

$$Q_\alpha |B\rangle \propto |F\rangle \tag{2.17}$$

Consequently, Supersymmetry predicts the existence of corresponding particles to each Standard Model particle with a spin different by half a unit. They are denoted as *sparticles*. Thus, to each Standard Model particle a partner-particle is assigned with the same quantum numbers (except the spin) and the same mass. Presently, no partner-particles of the Standard Model content were detected. This suggests that Supersymmetry is broken, leading to mass differences between Standard Model particles and their *sparticles*. For the warranty of lepton and baryon number conservation, a new multiplicative quantum number is introduced, the so-called R -parity. It is defined as:

$$P_R = (-1)^{3 \cdot (B-L) + 2s}, \quad (2.18)$$

with B and L being the baryon and lepton number and s the spin. For particles it is $P_R = 1$, whereas for SUSY particles it is $P_R = -1$. R -parity conservation leads to the fact that *sparticles* are produced only in pairs and subsequently decay into the lightest SUSY particle which is stable.

2.2.1 The MSSM

The Minimal Supersymmetric Standard Model (MSSM) is the minimal supersymmetric extension of the Standard Model. It introduces a large number of free parameters of ≈ 100 . In particular two complex Higgs doublets are introduced, one with positive and one with negative hypercharge:

$$Y = -\frac{1}{2} \quad \rightarrow \quad \Phi_u = \begin{pmatrix} \phi_u^+ \\ \phi_u^0 \end{pmatrix} \quad (2.19)$$

$$Y = +\frac{1}{2} \quad \rightarrow \quad \Phi_d = \begin{pmatrix} \phi_d^0 \\ \phi_d^- \end{pmatrix} \quad (2.20)$$

Their groundstates are chosen as:

$$\Phi_{u,0} = \frac{1}{\sqrt{2}} \begin{pmatrix} 0 \\ v_u \end{pmatrix}, \quad \Phi_{d,0} = \frac{1}{\sqrt{2}} \begin{pmatrix} v_d \\ 0 \end{pmatrix}. \quad (2.21)$$

The vacuum expectation values of the ground states are combined in the variable $\tan \beta = v_u/v_d$. The two Higgs doublets lead to eight degrees of freedom. Through electroweak symmetry breaking they make the Z^0 and the W^\pm bosons massive and result in five physical Higgs bosons. These are two neutral, CP-even Higgs bosons, h and H , one neutral, CP-odd, A , and a pair of charged Higgs bosons, H^\pm .

Despite the large number of free parameters, at tree level the MSSM is fully specified by two parameters. Generally, these are the mass of the CP-odd Higgs boson, m_A , and the variable $\tan \beta$. However, the tree level relations are modified significantly with radiative corrections. The mass of the lightest Higgs boson, m_h , for instance is constrained to be below the Z^0 boson mass at tree level. Depending on loop corrections, the upper bound on its mass is expected to be $m_h = 135$ GeV. The MSSM is divided into different parts of parameter space for studying the appropriate phenomenology. The scenario used in this work is the m_{max}^h scenario [13]. It is chosen

such that the mass of the lightest Higgs boson h is maximised as a function of $\tan\beta$. For this, m_A is set to its maximal value in this scenario, $m_A = 1$ TeV, the top mass is given by its experimental value and the soft SUSY-breaking mass parameters of the *sfermion* sector, M_{SUSY} , are fixed. The particular set of parameters is the following:

- $M_{SUSY} = 1$ TeV
- $\mu = 200$ GeV
- $X_t = A_t - \mu \tan\beta = 2$ TeV
- $M_2 = 200$ GeV
- $M_3 = 800$ GeV

Here, μ denotes the Higgs mixing parameter, A_t the trilinear Higgs *sfermion* couplings and M_2 and M_3 the $SU(2)$ gaugino and gluino mass parameters.

2.3 Experimental limits on the Higgs boson mass

The mass of the Standard Model Higgs boson is not predicted by theory. However, its mass is associated to properties of known particles such as the W^\pm boson or the t -quark through quantum mechanical effects. Constraints can be set, which say that the Standard Model Higgs boson mass is less than ~ 1 TeV [14].

The experimental limits on the Higgs boson mass are driven by experiments at the electron positron collider LEP [15], the proton-antiproton collider, TEVATRON [16], and the proton-proton collider LHC. Indirect limits on the Standard Model Higgs boson mass were set with precision measurements of electroweak interactions [17]. They imply a mass of $m_H < 159$ GeV at 95% confidence level (CL). Direct searches exclude a Standard Model Higgs boson mass below 600 GeV, apart from the mass region between 122 GeV and 128 GeV, at 95% CL. In detail, the existence is ruled out at 95% CL in the mass range:

- < 114.4 GeV at LEP [18],
- $(147 - 180)$ GeV at the TEVATRON [19],
- $(110 - 121.5)$ GeV and $(128 - 600)$ GeV with CMS [1],
- $(111 - 122)$ GeV and $(131 - 559)$ GeV with ATLAS [2].

Within the remaining mass range of $(122 - 128)$ GeV a new boson was discovered in the search for the Standard Model Higgs boson with the ATLAS and the CMS detector in 2012, [1–4]. Depending on the experiment, approximately 5 fb^{-1} of 7 TeV data and 5.5 fb^{-1} of 8 TeV data were analysed. The search was performed in the Higgs boson decay channels to two photons, $H \rightarrow \gamma\gamma$, to two Z^0 bosons, $H \rightarrow Z^0 Z^0$, to a pair of W^\pm bosons, $H \rightarrow W^+ W^-$, to two τ -leptons, $H \rightarrow \tau^+ \tau^-$, and to a

2.3 Experimental limits on the Higgs boson mass

quark-antiquark pair of b -quarks, $H \rightarrow b\bar{b}$. The measured 95% CL upper limits and the observed probability are given in figure 2.1. With the ATLAS experiment the largest local significance for a Standard Model Higgs boson reaches 5.9σ , the CMS experiment gains 5.8σ . The combined best fit yields the following masses with their statistical and systematic uncertainty:

$$\begin{aligned} \text{ATLAS: } m_H &= (126.0 \pm 0.4 \pm 0.4) \text{ GeV} \\ \text{CMS: } m_H &= (125.3 \pm 0.4 \pm 0.5) \text{ GeV} . \end{aligned}$$

Also the experiments at the TEVATRON reported an excess in the mass region (120 – 153) GeV. The observed local significance for a Higgs boson mass of $m_H = 125$ GeV is 2.8σ [20].

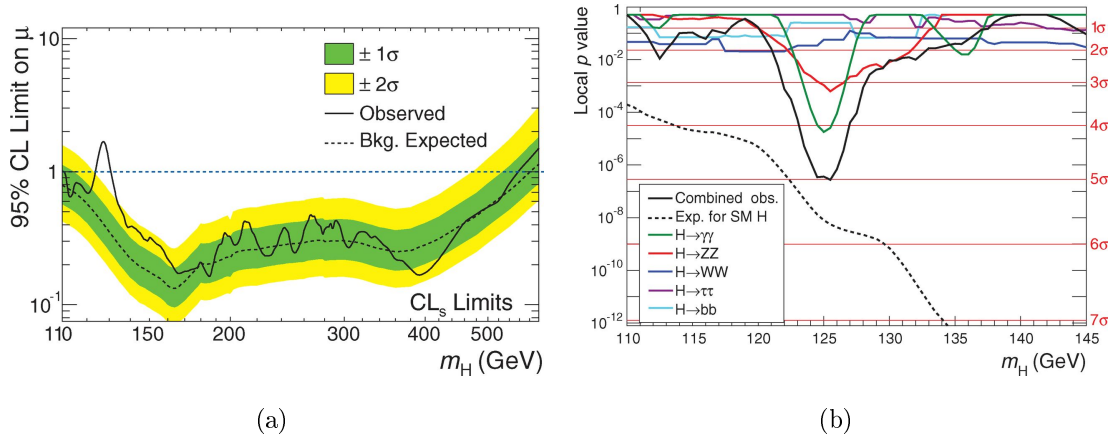


Figure 2.1: Figure (a) shows the measured 95% CL upper limits on the signal strength, μ , as a function of the Higgs boson mass (solid line) measured by the ATLAS detector. The expectation under the background-only hypothesis is given as the dashed line [3]. Additionally displayed are the $\pm 1\sigma$ (green band) and the $\pm 2\sigma$ (yellow band) uncertainties on the background-only expectation. The existence of the Higgs boson cannot be excluded with a signal strength above $\mu = 1$. Figure (b) shows the observed probability, referred to as the local p value, that the background-only hypothesis would yield as many (or more) events as seen in the CMS data. It is given as a function of the Standard Model Higgs boson mass, m_H . The p -value is displayed for the five analysed decay channels individually and for their combination [4].

3 Monte Carlo event generation and detector simulation

3.1 Monte Carlo event generation

Analysis in modern particle physics are usually based upon simulated processes. With the help of ensembles of simulated events the strategy to extract events of rare processes is developed. Especially for hadron colliders the simulation is non-trivial. Due to the asymptotic freedom (section 2.1.1) partons can only be regarded as free particles in scattering processes with a large momentum transfer which is equal to short time scales. At the energy regime of the LHC such a large momentum transfer is possible. Calculations considering this process can be conducted using perturbation theory. However, after a parton-parton interaction the final state particles may be still in colour-connection with the remaining partons of the colliding protons. It can be shown that a full treatment of a proton-proton interaction in a quantum-mechanically correct way is impossible. One tool with which predictions for particle interactions can be made are Monte Carlo event generators.

The difficulties of such simulations stem from the large number of contributing amplitudes, from the evaluation of higher order diagrams and from the limited understanding of the partonic substructure and the hadronisation process. Monte Carlo event generators calculate particle-particle collisions by dividing the process into several subprocesses acting at different energy scales. This is the case for all kind of particle-particle collisions. As this work bases on proton-proton interactions at the LHC, the following sections concentrate on these interactions, exclusively. Nevertheless, the basic principle of Monte Carlo generators is the same for all kind of particle-particle collisions.

The process of a proton-proton collision can be divided as depicted in figure 3.1. The first process is the hard interaction which is the interaction of partons from the incoming protons. Of course, there can be multiple parton-parton interactions. The hard process is defined as the interaction with the highest energy. Subsequently, the resulting particles decay further and hard QCD radiation is produced before the hadronisation of the final state particles takes place. Last, the emerging hadrons decay, whereas photon radiation occurs at all times. Additionally, there exist also beam remnants from the colliding protons. The subprocesses are shortly described in the following sections.

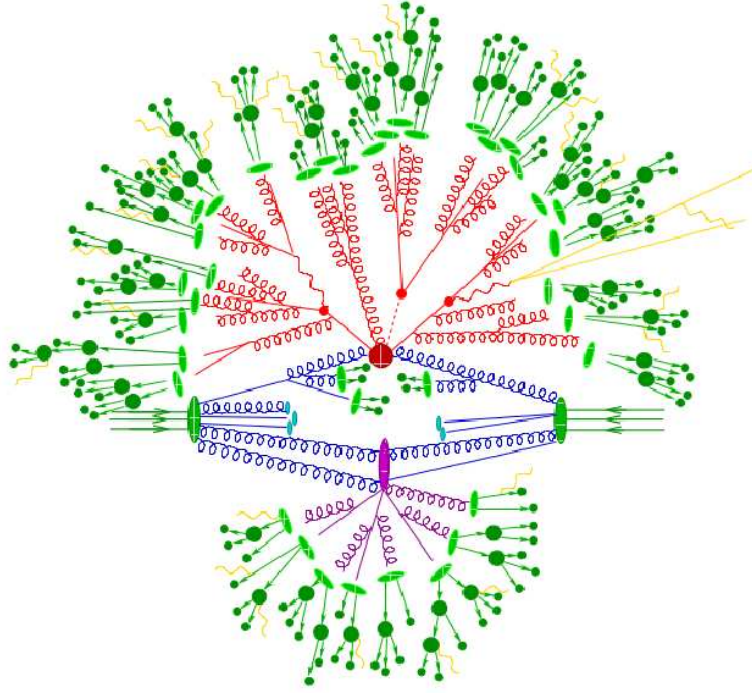


Figure 3.1: Depicted proton-proton interaction (big red blob) resulting in three massive particles. The hard interaction is followed by their decay (small red blobs). Furthermore, hard QCD radiation (red) occurs and a secondary interaction from other partons of the incoming protons (purple blob). Subsequently, the hadronisation of final state particles (light green blobs) takes place and emerging hadrons decay (dark green blobs). Photon radiation (yellow) can happen at all times. Remnants of the colliding protons are indicated as well (light blue blobs) [21].

Hard process

The hard process is given by the collision of two incoming particle, e.g. protons, with two partons interacting and determines the main characteristics of the event. The momentum distribution of the partons is described through parton density functions (PDF). They give the probability of a certain parton with a particular momentum being created inside a proton. The PDFs cannot be derived from first principles but need to be parametrized from experimental data in conjunction with theoretical assumptions dependent on the momentum scale. The hard process can be calculated in fixed order perturbation theory. The computations are based on matrix elements, followed by multi-dimensional phase space integration.

Parton shower

The particles of the hard process decay further, initialising a parton shower as depicted in red in figure 3.1. This QCD evolution connects the scale of the hard process with the scale at which hadronisation takes place. For the parton shower multiple QCD bremsstrahlung is simulated which can be done in approximation to exact perturbation theory. In contrast to the hard process the parton shower contains soft and collinearly radiated particles. Subsequently, the hard process and the parton shower need to be merged, as a complete distinction between them is not possible. This is achieved with several matching schemes [21–23].

Hadronisation and particle decays

As stated earlier, partons can propagate as free particles only on a short time scale. The observables finally being measured with particle detectors are caused by hadrons, leptons and photons. Monte Carlo generators describe the transition from partons to colourless hadrons with the parton-to-hadron fragmentation. The fragmentation process can only be described in a non-perturbative way and needs phenomenological approaches. There are two models which are commonly used. This is the Lund-string scheme [24, 25] with which quark pairs are connected via virtual colour strings. The strings form a potential between the quarks from which new quark-pairs may arise if the potential is high enough. The second commonly used scheme is the cluster-hadronisation model [26, 27]. It bases on the assumption that quantum numbers on hadron level follow the flow of quantum numbers on parton level.

Some of the emerging hadrons decay further into lighter hadrons and/or leptons. They travel away from the interaction point as bundles of hadrons, being called jets in experimental particle physics. Furthermore, some Monte Carlo generators also treat the correlation among particles, such as spin-correlations.

Multiple parton interactions and beam remnants

It may occur that not only two of the incoming partons interact with each other but that multiple parton interactions take place. Together with the remnants of the protons they form the so-called underlying event. The components of the underlying event are still in colour connection with the components of the hard process. Its modeling goes beyond QCD factorisation theorems. Phenomenological theories are employed with free parameters which are adjusted to describe experimental data.

3.2 Detector simulation

Events being simulated by Monte Carlo event generators cannot be directly used for a physics analysis of recorded collision events. Instead, it needs to be transformed into a format which is identical to the detector readout. For the ATLAS detector this is achieved with the software framework ATHENA [28]. As depicted in figure 3.2

the simulation of a certain process can be divided into three steps. The event generation and the simulation of immediate decays is accomplished by Monte Carlo event generators. They provide four-momentum vectors of the generated particles. After this, the physics interactions of the generated particles with the detector material as well as the detector response to them are simulated. For this, the GEANT4 simulation toolkit [29, 30] is used. The whole ATLAS detector geometry is described in databases which contain information about the physical construction and their condition. With the GEANT4 simulation toolkit the passage of particles through matter including hadronic, electromagnetic and optical processes is simulated as well as decays of short-living secondary particles. The models used are chosen depending on the energy range of the incident particles. The toolkit is based on object oriented programming design, using Monte Carlo methods for the particle propagation. During the third step of the simulation chain, energy deposits in sensitive detector regions are digitised into currents and voltages. The format of the output can be chosen to be identical with that of the ATLAS data acquisition. This allows to use identical software for trigger and object reconstruction for either simulated events or real data. Consequently, the output of the reconstruction chain is the same for simulated and recorded data allowing the usage of the same analysis software.

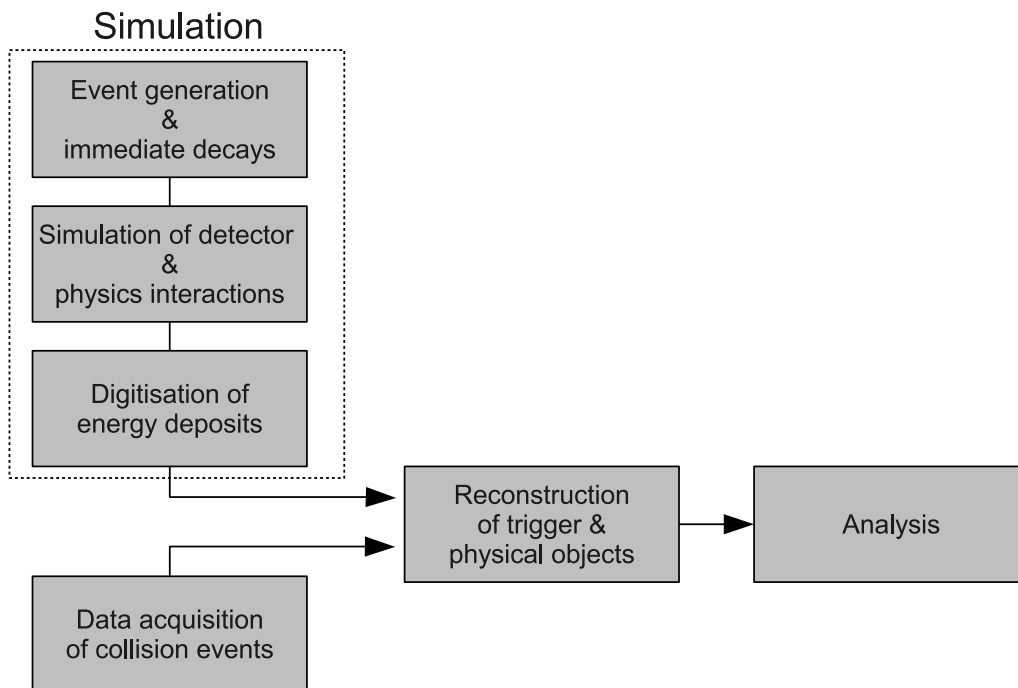


Figure 3.2: Flow of simulated events and recorded data within the ATLAS software framework. The simulation is accomplished by the event generation, the simulation of physics interaction and detector response and the digitisation. The same format of simulated and recorded events enter the reconstruction chain and the analysis software.

4 The ATLAS experiment at the LHC

4.1 The Large Hadron Collider

The Large Hadron Collider (LHC) [31, 32] is situated at the European Organization for Nuclear Research (Conseil Européen pour la Recherche Nucléaire, CERN) at the border of France and Switzerland, near Geneva. With a circumference of 26.7 km it is the world's largest particle collider. The tunnel is placed 50 - 100 m underneath, inside the tunnel of the former LEP experiment. The LHC is a two-ring-superconducting hadron accelerator with counter-rotating beams, which accelerates protons or lead ions using the synchrotron principle.

The operation of the LHC started in 2008, shortly followed by a Helium leak accident [33]. After a period of reparation works [34], the first proton-proton collisions at a centre of mass energy of $\sqrt{s} = 7$ TeV occurred in 2010. This collision energy was chosen to prevent similar accidents as in 2008. Since April 2012 the centre of mass energy was ramped up to $\sqrt{s} = 8$ TeV. This period was completed in December 2012, being followed by a longer pause of 1 to 1.5 years without operation in physics mode. After that, it is aspired to reach the centre of mass energy of $\sqrt{s} = 14$ TeV, for which the LHC originally was designed for.

The limitation to an energy of 7 TeV per beam is given by the magnetic field of the dipoles, bending the beams within the ring. For this, 1232 dipoles are installed. These are superconducting magnets with a magnetic field yielding up to 8.33 T and being cooled down to 1.9 K by superfluid helium. The superconducting dipoles are designed with the “twin-bore” concept, for which the magnets' windings for two beam channels share a common cold mass and cryostat. The focusing and correction of the beam shape is accomplished by approximately 3700 additional multipole magnets. The protons are accelerated and stored at their nominal energy with the use of a 400 MHz superconducting cavity system. Each beam has a lifetime limited to 10 to 20 hours.

The LHC was built to explore particle physics at the high energy regime. Besides resolving the search for the Higgs boson, fundamental questions of particle physics ought to be answered. For this purpose there are four dedicated interacting regions, where through beam crossing proton-proton interactions take place. At these interaction points four experiments are installed. These are two multipur-

pose detectors of different detector techniques, the ATLAS detector [35] and the CMS detector [36]. Both are built for the search of the Higgs boson and for physics beyond the Standard Model. Furthermore, two specialised detectors are installed. This is the ALICE experiment [37], dedicated to heavy-ion physics, and the LHCb experiment [38], which is built for precision measurements of CP violation as well as rare b -quark decays.

4.1.1 Injection Chain

The protons circulating inside the LHC stem from an hydrogen source and are pre-accelerated passing through an injection chain. The injection chain uses the infrastructure of the CERN accelerator complex which can deal with different types of particles and delivers pre-accelerated beams for different experiments. For the LHC experiment the protons first enter the linear accelerator Linac2, where they are accelerated up to 50 MeV. The protons are then injected into the Proton Synchrotron Booster, PSB. After reaching an energy of 1.4 GeV, the protons are injected to the Proton Synchrotron, PS, where they are boosted to 26 GeV. The last pre-accelerator before entering the rings of the LHC is the Super Proton Synchrotron, which brings the protons to their injection energy of 450 GeV. Finally, the protons are transferred through two tunnels linking the CERN accelerator complex and the LHC. A detailed view of the CERN accelerator complex is given in figure 4.1.

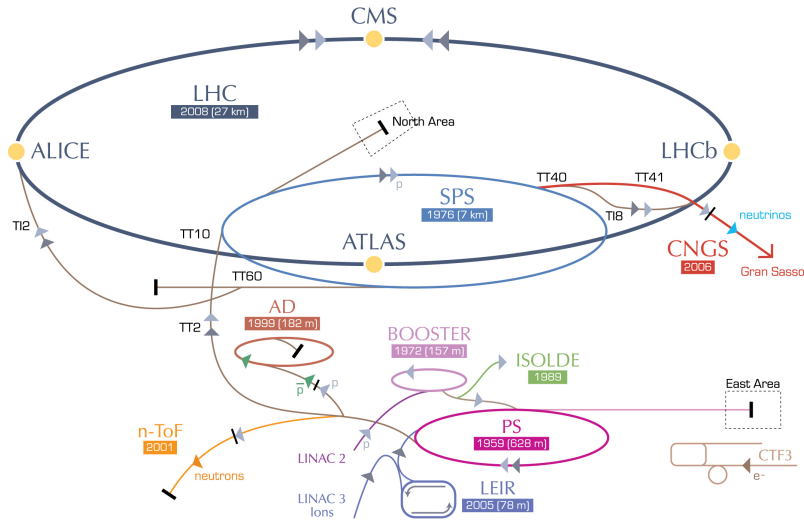


Figure 4.1: Infrastructure of the CERN accelerator complex. Furthermore, the four interaction points of the two proton beams with their dedicated experiments, CMS, ALICE, ATLAS and LHCb, are depicted [39]

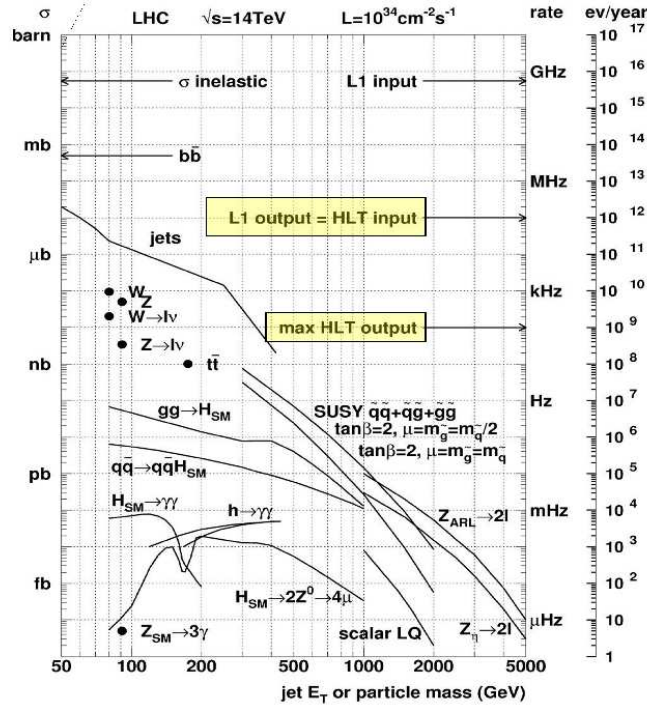


Figure 4.2: Expected rates of Standard Model and SUSY processes for a centre of mass energy of $\sqrt{s} = 14$ TeV and with the design luminosity of $\mathcal{L} = 10^{34} \text{ cm}^{-2} \text{ s}^{-1}$ [40].

4.1.2 Beam conditions

Because of the usage of superconducting high frequency cavities for accelerating and storing the beam, it is not possible to provide a continuous proton beam. Instead, the protons are bundled with up to $1.15 \cdot 10^{11}$ protons per bunch. At design operation the bunches have a temporal separation of 25 ns. With this, up to 2808 bunches can be present in the proton beam at the LHC. The rate of events, \dot{N}_{ev} , arising at the interaction point is given by the luminosity of the beam, \mathcal{L} and the cross section of the process, σ :

$$\dot{N}_{ev} = dN_{ev}/dt = \mathcal{L} \cdot \sigma. \quad (4.1)$$

While the cross section is a fixed value at a certain centre of mass energy, the instantaneous luminosity is assembled by beam parameters. With the assumption of gaussian beam shapes and equal beam parameters for both beams, \mathcal{L} can be described by:

$$\mathcal{L} = \frac{N_P^2 n_b f_{rev} \gamma}{4\pi \epsilon_n \beta} \cdot F. \quad (4.2)$$

The corresponding parameters are the number of particles per bunch, N_P , the number of bunches per beam, n_b , the revolution frequency, f_{rev} , the relativistic gamma parameter, γ , the normalized transverse beam emittance, ϵ_n and the beta function

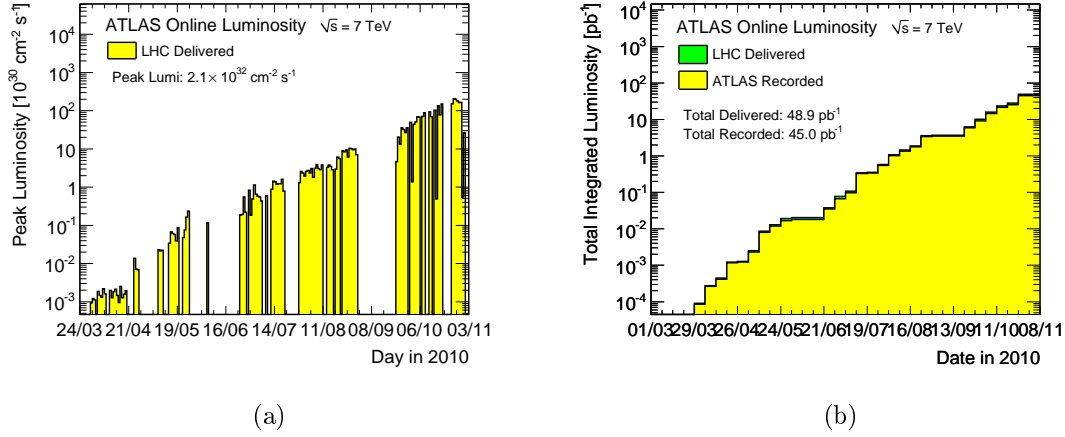


Figure 4.3: Evolution of the instantaneous peak luminosity (a) and the integrated luminosity recorded by the ATLAS detector for operation in 2010 [41].

at the collision point, β . The luminosity is further dependent on the crossing angle of the two beams at the interaction points, which is described through the geometric luminosity reduction factor, F . For the detection of rare events the beam conditions need to be prepared in a such a way that high luminosities are gained. The luminosity can be increased by increasing the beam intensity, i.e. a higher number of particles per bunch, N_P , and by increasing the particle energy. The latter is possible since the relativistic gamma parameter depends on the energy: $\gamma = E/E_0$, with E_0 being the rest energy.

For the operation with proton beams the aspired instantaneous luminosity at the LHC is $\mathcal{L} = 10^{34} \text{ cm}^{-2} \text{ s}^{-1}$. The cross sections expected with a centre of mass energy of $\sqrt{s} = 14$ TeV and the resulting rates of processes at the design luminosity are given in figure 4.2.

For the operation in 2010, beam conditions varied, in particular the number of protons per bunch and the number of bunches. With this, the instantaneous luminosity increased constantly as is depicted in figure 4.3(a). For the data analysed in this work individual bunches of protons, with $N_P = 10^{11}$ protons per bunch, are temporally separated by 150 ns. Eight individual bunches form so-called bunch trains. Per fill the number of bunches is $n_b = 368$. With these beam conditions peak luminosities of $\mathcal{L} = 10^{32} \text{ cm}^{-2} \text{ s}^{-1}$ were achieved. The total integrated luminosity recorded by the ATLAS detector in 2010 was 45 pb^{-1} .

For the operation in 2011 at $\sqrt{s} = 7$ TeV the peak luminosity even increased to $2 \cdot 10^{32} \text{ cm}^{-2} \text{ s}^{-1}$ with a recorded integrated luminosity of 5.25 fb^{-1} . In 2012 the centre of mass energy was set to $\sqrt{s} = 8$ TeV. Peak luminosities of $7 \cdot 10^{33} \text{ cm}^{-2} \text{ s}^{-1}$ were achieved and the ATLAS detector recorded a total of 21.7 pb^{-1} .

4.2 The ATLAS detector

The ATLAS detector is an all-purpose detector built to resolve the search for the Higgs boson and to answer fundamental questions of particle physics. It is situated at Point 1 of the CERN complex, one of the interaction points of the LHC. The ATLAS detector has a cylindrical design with a layer structure of dedicated subdetectors for the detection of particles. Hadrons, leptons or photons traversing the detector leave a certain signature, which are analysed by specific algorithms to reconstruct particle objects. Its layout is depicted in figure 4.4. The ATLAS detector is divided into three major subdetectors which are being explained in more detail in the following section. The outermost component is a muon spectrometer, which surrounds a high-granularity calorimetry system. The innermost component is a tracker system of different technologies situated in a 2 T magnetic field which is provided by a solenoid.

The ATLAS detector has an overall length of 44 m with a diameter of 25 m and a weight of 7000 t. Its name is an acronym for “A Toroidal LHC ApparatuS”. A detailed description of the detector can be found in [35].

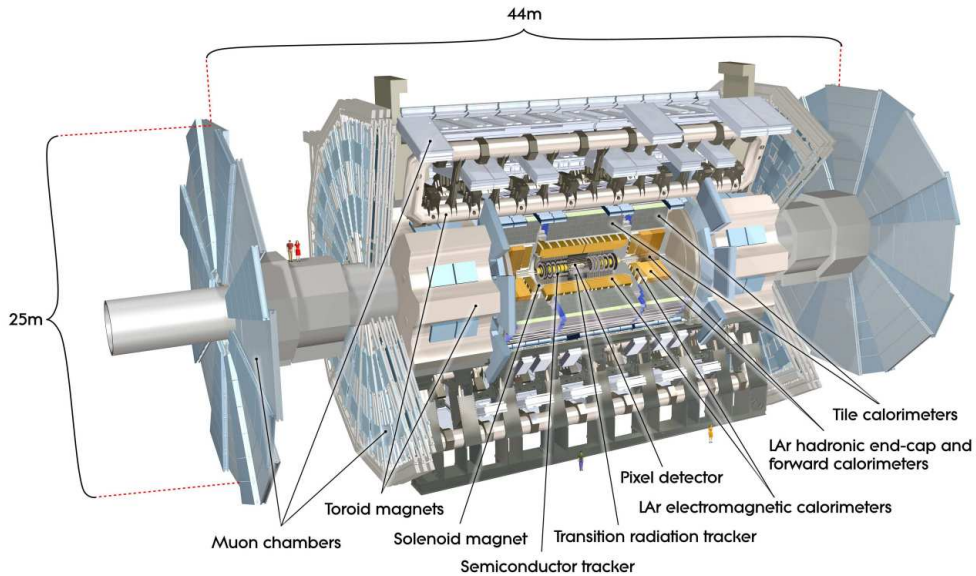
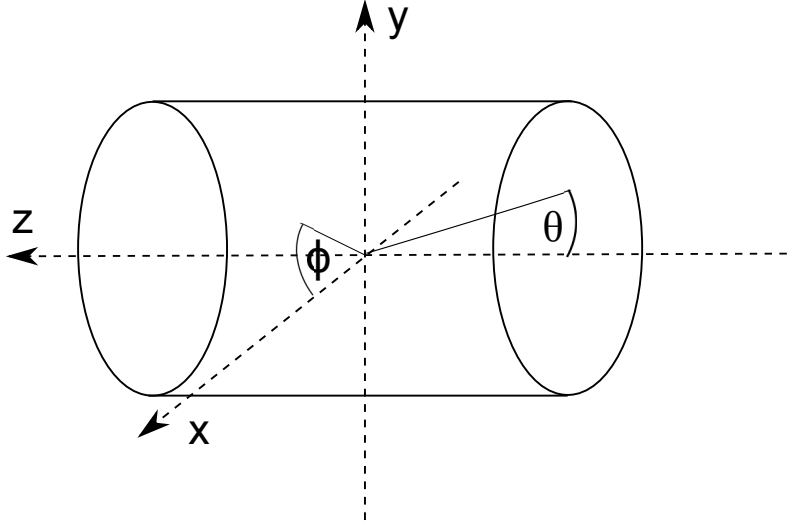


Figure 4.4: Layout of the ATLAS detector with its subdetectors [35].

The origin of the cartesian coordinate system used at the ATLAS experiment is at the expected interaction point of the beams. The coordinate system is chosen such that the beam direction of the LHC is the z -axis. The x -axis points towards the centre of the LHC ring, while the y -axis points upwards towards the surface as depicted in figure 4.5. The so-called transverse plane is the x - y plane, which is the plane perpendicular to the beam axis. Components of this plane are labelled

**Figure 4.5:** Coordinate system of the ATLAS detector.

with “T” and are calculated as $p_T = \sqrt{p_x^2 + p_y^2}$. The kinematics of a particle of a given mass are fully described with the direction variables ϕ , η and the transverse momentum p_T . The first two are based on cylindrical coordinates, with ϕ being the azimuthal angle measured in the x - y plane. The pseudorapidity, η , is calculated from the polar angle θ , which is defined with respect to the beam axis as follows:

$$\eta = -\ln \left[\tan \left(\frac{\theta}{2} \right) \right]. \quad (4.3)$$

With this definition, $\eta = 0$ points along the y -axis, whereas large values of η point along the beam axis. In hadron collider physics the rapidity is the preferred variable over the polar angle θ , since the particle flux in the detector is about constant with respect to θ . The rapidity, y_r , of a particle with an energy E and the momentum p_z in the z -direction is described as:

$$y_r = -\frac{1}{2} \ln \frac{E + p_z}{E - p_z}. \quad (4.4)$$

For high energies with respect to the particles’ mass the rapidity converges into the pseudorapidity. Because of this and since η is independent of the energy or momentum of the particle, η is commonly used within the ATLAS collaboration. The geometrical distance between two objects, p_1 and p_2 , is calculated from the pseudorapidity and the azimuthal angle as follows:

$$\Delta R = \sqrt{\Delta\phi^2 + \Delta\eta^2}, \quad (4.5)$$

with $\Delta\phi = \phi_{p1} - \phi_{p2}$ and $\Delta\eta = \eta_{p1} - \eta_{p2}$. The radius from the z -axis is given as $r = \sqrt{x^2 + y^2}$.

4.2.1 The magnet system

The ATLAS detector comprises two individual magnet systems which are depicted in figure 4.6. They consist of a central solenoid housing the inner tracking system and three air-core toroids being used for the track measurement in the muon system. The central solenoid provides a 2 T axial magnetic field for the inner tracking system. Trajectories of charged particles traversing the inner tracking system are bent and their momentum can be identified. To minimise the material in front of the calorimetry system the solenoid shares a common vacuum vessel with the barrel ELECTROMAGNETIC CALORIMETER.

The three air-core toroids consist of eight independent coils each, arranged radially and symmetrically around the beam axis. The barrel toroid produces a magnetic field of approximately 0.5 T, while the magnetic field of the two end-cap toroids is of 1 T. With this setup, trajectories of particles traversing both, the inner tracking system and the muon spectrometer, are bent in the x - y plane within the solenoid and in the r - z plane within the toroidal field.

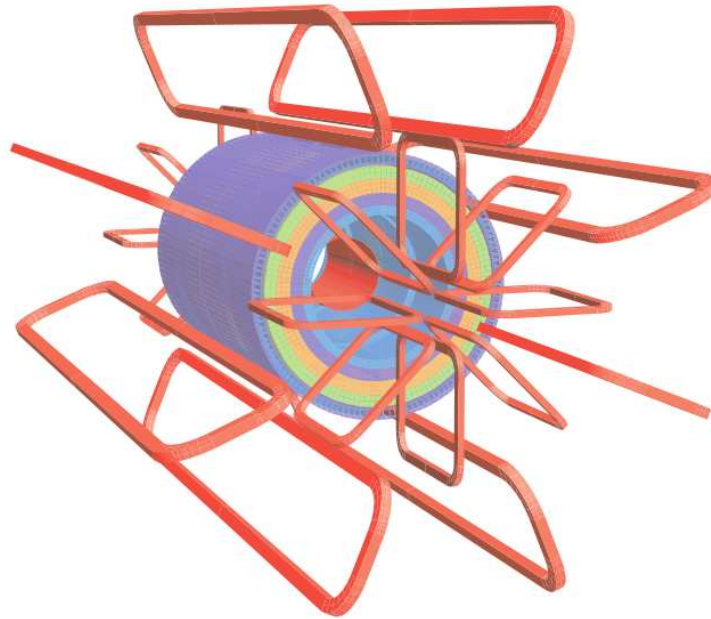


Figure 4.6: Layout of the magnet system of the ATLAS detector. Depicted are the central solenoid and the eight barrel toroid coils, with the end-cap coils interleaved [35].

4.2.2 The inner tracking system

The inner tracking system is referred to as the INNER DETECTOR and constitutes the innermost layer of the ATLAS detector. Its layout is depicted in figure 4.7. The

inner tracking system is designed to measure the position and momentum of charged particles with high precision and efficiency in both, the r - ϕ and z coordinates. It is divided into three complementary subdetectors. They provide an acceptance in pseudorapidity of $|\eta| < 2.5$ for particles coming from the interaction point. In ϕ a full coverage is provided. The inner tracking system is designed to provide a transverse momentum resolution of $\sigma(p_T)/p_T = 0.05\% \cdot p_T / \text{GeV} \oplus 1\%$ [35]. After detector alignment, the resolution of the transverse impact parameter for high momentum particles was found to be $22.1 \pm 0.9 \mu\text{m}$, for the longitudinal direction it was found to be $112 \pm 4 \mu\text{m}$ [42]. The inner tracking system is immersed in a 2 T magnetic field generated by the central solenoid (section 4.2.1).

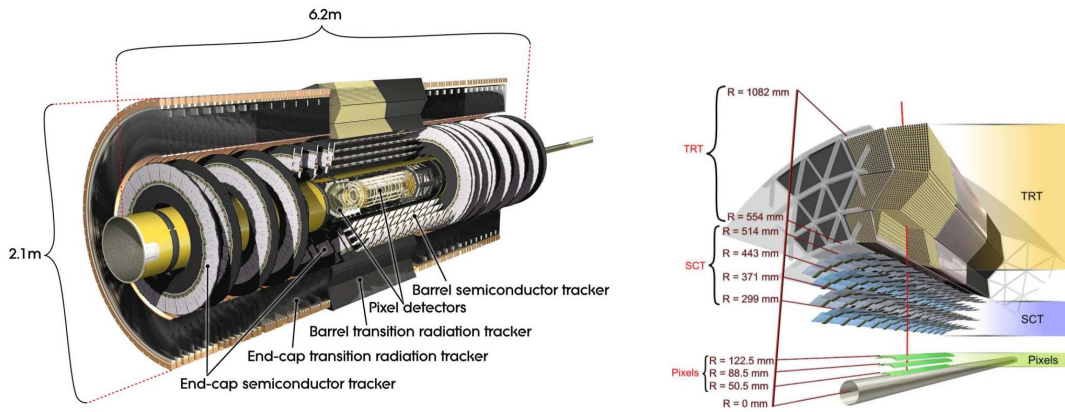


Figure 4.7: Layout of the Inner Detector with its components (a) and a detailed view of the barrel system at $\eta = 0.3$ (b) [35]. For illustrative reasons the cooling and electronic systems are not shown.

The silicon pixel detector

The silicon pixel detector is arranged in three concentric barrel layers covering a radial distance of 5 cm to 15 cm from the beam axis. It spans a range in pseudorapidity of $|\eta| < 1.7$. The innermost layer is the so-called b -layer, because of its importance for b -quark tagging performance. In the end-cap region, covering the range $1.7 < |\eta| < 2.5$, the silicon pixel detector consists of three discs orthogonal to the beam axis. The layers and discs are arranged such that a charged particle traversing the detector always hits three detector layers. In total the silicon pixel detector has approximately $80 \cdot 10^6$ pixel sensors. With this, a tracking accuracy of $10 \mu\text{m}$ in the r - ϕ plane and $115 \mu\text{m}$ in the z -direction of the barrel is reached. The working principle of the pixel sensors is based on silicon pn-diodes in reversed bias. The diodes are connected to readout chips via conductive bumps. A high voltage is applied to the pixel sensor. If a charged particle traverses the diode additional free charge carriers are generated through excitation across the bandgap. Because of the electric field the charge carriers begin to move and induce a signal on the

pixel electrodes. The operating temperature ranges from -5°C to -10°C to reduce leakage current and to keep the effective doping concentration stable.

The Semiconductor Tracker

The SemiConductor Tracker (SCT) is arranged in four concentric barrel double-layers with a constant pitch of $80\mu\text{m}$. They span a radial distance of 30 cm to 56 cm from the beam pipe and in pseudorapidity $|\eta| < 1.4$. The end-caps, spanning $1.4 < |\eta| < 2.5$, each contain nine disks with variable pitch. For particles originating from the interaction point four space-points are measured, typically. The SCT consists of 4088 modules of silicon micro-strip sensors. They have the same working principle like the pixel sensors described above. A channel is read out if the induced pulse height exceeds a preset threshold. This procedure keeps the read-out occupancies as low as possible.

As the double-layers are tilted to each other by an angle of 40 mrad a high resolution is achieved in the r - ϕ plane. In the barrel component the spatial accuracy is $17\mu\text{m}$ in r - ϕ and $580\mu\text{m}$ in the z -direction. With this, two tracks can be distinguished if they are separated by more than $200\mu\text{m}$. Together with the silicon pixel detector, the SCT is cooled at a temperature of -5°C to -10°C .

The Transition Radiation Tracker

The Transition Radiation Tracker (TRT) consists of 298304 proportional drift tubes, each of them with a diameter of 4 mm. It is built to increase the electron identification above that of the ELECTROMAGNETIC CALORIMETER. When a charged particle traverses the polypropylene fibers (barrel TRT) or polypropylene foils (end-cap TRT) between the tubes, through transition radiation photons are caused. The drift tubes are filled with a xenon-based gas mixture. At its centre an anode wire is placed with an electric field between the wire and the cylindrical walls of the tube. If charged particles or energetic photons pass through the gas volume they can release free charge carriers through interactions with the gas. The released electrons drift towards the anode wire and induce a signal.

The TRT covers the radial distance from 56 cm up to 107 cm. In the barrel region, covering $|\eta| < 0.7$, the drift tubes are arranged in three cylindrical layers, segmented into 32 ϕ sectors. They are read-out at both sides, dividing the tubes into two halves at $\eta = 0$. In the end-caps they are oriented radially and split into 80 disc modules. Charged particles with a transverse momentum larger than $p_{\text{T}} = 0.5\text{ GeV}$ and $|\eta| < 2.0$ typically cross more than 30 drift tubes.

4.2.3 The calorimetry system

The calorimetry system of the ATLAS detector is divided into the ELECTROMAGNETIC CALORIMETER and the HADRONIC CALORIMETER. Its layout is depicted in figure 4.8. The whole system covers a range in pseudorapidity of $|\eta| < 4.9$. Within

the η region which is covered by the inner tracking system, $|\eta| < 2.5$, the ELECTROMAGNETIC CALORIMETER provides a fine granularity. With this, high-precision measurements of electrons and photons are possible. The rest of the calorimetry system shows a coarser granularity, which is sufficient for the jet reconstruction and measurements of the missing transverse energy (section 4.5.5). Furthermore, the thickness of the calorimetry system is built to provide a good containment for electromagnetic and hadronic showers on the one hand. On the other hand, also the escape of hadrons or electrons into the muon system is limited.

The calorimetry system provides a full ϕ -symmetry and coverage around the beam axis. It is designed to measure the energy of electrons, photons and hadronic particles, which are seen in the detector as particle jets¹. The calorimeter components closest to the beam-line use liquid argon as the active detector material. These are the barrel ELECTROMAGNETIC CALORIMETER, situated in one cryostat, and the electromagnetic end-cap, the hadronic end-cap and the forward calorimeter which are all housed in one cryostat at each end-cap. The outer hadronic calorimeter is separated into one central barrel and two extended barrels whose active medium are scintillator tiles and the absorber medium is steel.

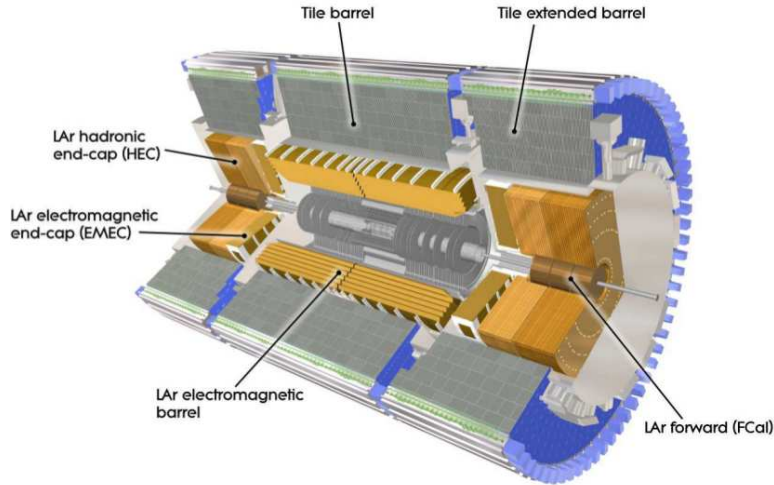


Figure 4.8: Layout of the calorimetry system of the ATLAS detector with the components using liquid argon as the active detector material and the outer hadronic calorimeter [35].

The Electromagnetic Calorimeter

The ELECTROMAGNETIC CALORIMETER consists of two identical barrel parts, separated by a small gap of 4mm at $z = 0$. They cover the range $|\eta| < 1.475$. Furthermore, it is built of two end-cap components, each of them mechanically di-

¹A full explanation of particle jets can be found in section 4.5.4.

vided into two wheels. The inner wheel provides an acceptance in pseudorapidity of $2.5 < |\eta| < 3.2$ while the outer wheel covers $1.375 < |\eta| < 2.5$.

The ELECTROMAGNETIC CALORIMETER is a lead-liquid argon detector with alternating regions of passive detector material (lead) and active detector material (liquid argon). In the passive detector material an electromagnetic shower of electrons, positrons and photons is induced. The electrons and positrons then cause a signal on the electrodes when traversing the liquid argon. To provide a complete ϕ symmetry a geometry with accordion-shaped kapton electrodes and lead absorber plates, which are arranged axially, was chosen. The barrel component has a total thickness of 22 to 33 radiation lengths² X_0 . It is subdivided into three longitudinal sections (or *samplings*) differing in granularity, as depicted in figure 4.9. The innermost layer has the highest granularity. It is finely segmented into strips along η with a length of about 4 mm each. The other two samplings are coarser in η with a finer granularity in ϕ , covering an area of about $(4 \times 4) \text{ cm}^2$ at $\eta = 0$ in the second layer. Each compartment constitutes a so-called cell. In the end-caps the material covers 24 to 36 radiation lengths. The accordion waves are arranged parallel to the radial direction. In the pseudorapidity range of $|\eta| < 1.8$ a presampler detector is installed which corrects for the energy loss of electrons and photons upstream of the calorimeter.

The ELECTROMAGNETIC CALORIMETER provides an energy resolution [35] of

$$\frac{\sigma_E}{E} = \frac{a}{\sqrt{E/\text{GeV}}} \oplus \frac{b}{E} \oplus c.$$

All three parameters are η dependent. However, the target values of the parameter are respectively for the stochastic term $a \simeq 10\%$, for the noise term $b \simeq 0.17 \text{ GeV}$ and for the constant term $c = 0.7\%$.

The Hadronic Calorimeter

The HADRONIC CALORIMETER can be divided into two components with respect to their working principle. The so-called tile calorimeter follows the barrel part of the ELECTROMAGNETIC CALORIMETER. It is subdivided into one central barrel, covering the region $|\eta| < 1.0$, and two extended barrels, which give an acceptance in pseudorapidity of $0.8 < |\eta| < 1.7$. All three are longitudinally separated into three layers with the innermost radius of 2.28 m from the beam axis and an outer radius of 4.25 m. In units of the interaction length³ λ the layers have a thickness of approximately 1.5, 4.1 and 1.8 λ for the barrel part and 1.5, 2.6, and 3.3 λ for the extended barrel. Azimuthally, they are divided into 64 modules. The tile calorimeter is a sampling calorimeter with steel as the absorber medium and scintillating plastic tiles as the active detector material. The readout of the scintillating tiles is accomplished through wavelength shifting fibres connected to photomultipliers. A hadron

²The radiation length is defined as the distance in which an electron or positron loses all but $1/e$ of its energy due to radiation loss.

³The interaction length is the mean free path of a hadronic particle before undergoing an inelastic interaction.

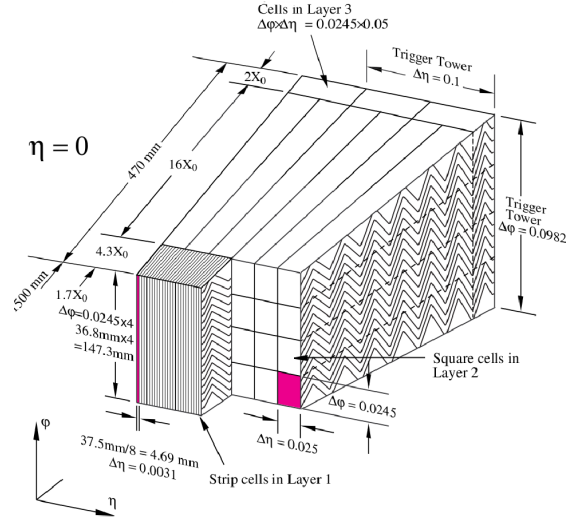


Figure 4.9: Layout of the barrel liquid argon calorimeter with its longitudinal division and the accordion structure [35].

traveling through the passive absorber medium causes a series of inelastic hadronic nuclear interactions. The secondary particles of the interaction deposit energy in the scintillating tiles producing ultraviolet scintillating light. Through wavelength shifters the ultraviolet light is then converted into visible light and eventually to an electrical charge by the photomultipliers.

The second component of the HADRONIC CALORIMETER uses liquid argon as the active detector material. The two hadronic end-caps at each side of the detector cover a region $1.5 < |\eta| < 3.2$, overlapping slightly with the tile calorimeter and the forward calorimeter to reduce the drop in material density at the transition regions. They are located behind the electromagnetic end-caps and consist of two independent wheels, respectively, assembled one in a row. With both wheels being segmented into two layers, the hadronic end-caps provide four layers each. The passive detector material of the end-caps is made of copper plates with 8.5 mm gaps filled with the liquid argon.

The forward calorimeter which is housed in a common cryostat together with the electromagnetic and hadronic end-caps covers the pseudorapidity range of $3.1 < |\eta| < 4.9$. It is divided into three modules differing in the passive detector material. The first module is made of copper, while the other two use tungsten. Each of the modules is built of a metal matrix holding longitudinal channels, working as electrodes. The channels consist of concentric tubes and rods and are filled with liquid argon.

The HADRONIC CALORIMETER provides an energy resolution for the tile component and the hadronic end-caps [35] of

$$\frac{\sigma_E}{E} = \frac{50\%}{\sqrt{E/\text{GeV}}} \oplus 3\%.$$

The forward calorimeter yields an energy resolution [35] of

$$\frac{\sigma_E}{E} = \frac{100\%}{\sqrt{E/\text{GeV}}} \oplus 10\% .$$

4.2.4 The Muon Spectrometer

The outermost subdetector of the ATLAS detector is the MUON SPECTROMETER. Compared to the electron mass of 0.511 MeV [5], the muon mass of 105.6 MeV [5] is comparably large. Since the energy loss is proportional to the inverse squared mass they do not initiate a particle shower in the ELECTROMAGNETIC CALORIMETER. Instead, they traverse the detector up to the MUON SPECTROMETER with an energy loss of approximately 3 GeV. With the calorimetry system being built to provide a good containment for electromagnetic and hadronic showers, muons are the only particles which are capable to reach the MUON SPECTROMETER (except for neutrinos, which leave the detector without interactions). The muon system provides an autonomous track measurement with high precision position information.

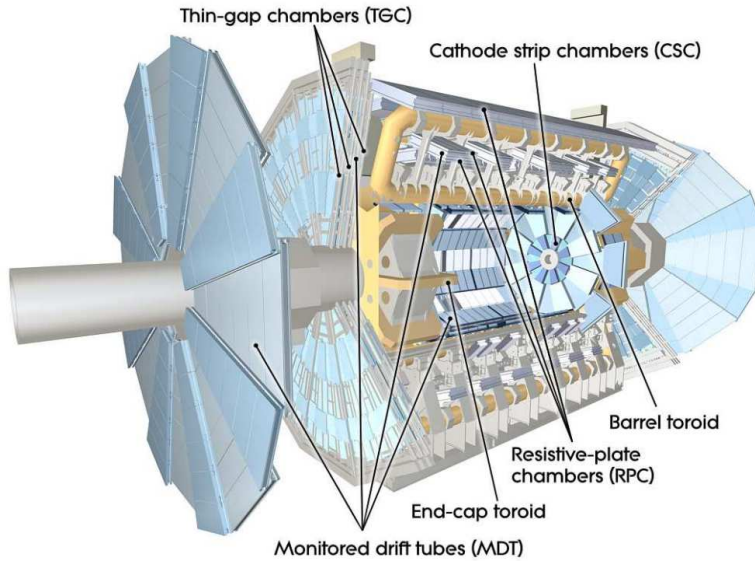


Figure 4.10: Layout of the MUON SPECTROMETER together with the toroidal magnet system [35].

The MUON SPECTROMETER is embedded in the magnetic field of the toroidal magnet system as described in section 4.2.1. The magnetic field is provided by the large barrel toroid for pseudorapidities $|\eta| < 1.4$, while for $1.6 < |\eta| < 2.7$ the two end-cap magnets are responsible. In the transition region, $1.4 < |\eta| < 1.6$ the magnetic field is a superposition of both. The muon system is built of different

trigger and high-precision tracking chambers. Its layout is depicted in figure 4.10. The muon tracks are measured in the x - y plane by Monitored Drift Tubes (MDT's) in the barrel part, which are arranged in three cylindrical layers parallel to the beam axis. The MDT's are built of aluminum tubes, 3 cm in diameter, and a drift-gas mixture of argon and carbon dioxide at a pressure of 3 bar. They provide a position resolution of $80\ \mu\text{m}$. For large pseudorapidities $2 < |\eta| < 2.7$ Cathode Strip Chambers (CSC's) are installed in three layers perpendicular to the beam axis. The CSC's have a higher granularity and are better suited for higher rates and radiation. They are built of multiwire proportional chambers filled with a gas mixture of argon, carbon dioxide and tetrafluoromethane, achieving an average position resolution of $60\ \mu\text{m}$.

Resistive Plate Chambers, covering the barrel part, and Thin Gap Chambers for the end-cap regions constitute the trigger system. They cover the pseudorapidity range $|\eta| < 2.4$.

4.3 Trigger system

With the LHC working at the design parameters, the bunch crossing rate in the ATLAS detector is 40 MHz. The full read-out of the ATLAS detector is possible with a rate of 75 kHz. The full detector information can be stored with a rate of 200 Hz. Because of the large range between the collision event rate and the rate at which events can be stored a trigger system is installed to reduce the input rate for recording and offline processing. Furthermore, the trigger system is dedicated to select specific events from the large ensemble of proton-proton collisions. As depicted in figure 4.2 the rates of events of interest is of the order 10^6 to 10^{12} smaller than the total rate of inelastic p - p collisions at a design luminosity of $\mathcal{L} = 10^{34}\ \text{cm}^{-2}\text{s}^{-1}$ and a centre of mass energy of $\sqrt{s} = 14\ \text{TeV}$.

The trigger system is divided into three distinct levels: the Level 1, the Level 2 trigger and the event filter. The two latter form the so-called High-Level Trigger. They are software-based systems using information from all subdetectors. In contrast, the Level 1 trigger is a hardware-based system with reduced-granularity information from only a subset of detectors. For each trigger level the decisions made at previous levels are refined and additional selection criteria are added if necessary. The trigger system is constructed to identify single or multiple candidates of physics objects. Furthermore, there exist triggers based on global event properties such as the summed transverse energy of physics objects or the missing transverse energy (section 4.5.5). In addition, there is also a set of monitoring and calibration triggers. The Level 1 trigger is constructed to make a decision in less than $2.5\ \mu\text{s}$ after the bunch-crossing with which it is associated. For this, it makes use of limited detector information, namely reduced-granularity information of the Resistive Plate Chambers and the Thin Gap Chambers of the muon system and of all calorimeter systems. Regions of the detector in which possible trigger objects were identified are saved as so-called Regions-of-Interest. The Level 1 trigger reduces the rate to 75 kHz.

The High-Level Trigger system consisting of the Level 2 trigger and the event filter are software-based systems. They have access to full granularity and precision of calorimeter and muon chamber data, as well as the data from the inner tracking system. With better information on energy depositions and an enhanced particle identification through track reconstruction in the inner tracking system, the trigger selection is refined. The Level 2 trigger is seeded by Regions-of-Interest from the Level 1 trigger and uses its information about coordinates, energy, and type of signatures. This trigger level reduces the rate to 3.5 kHz. The last level of the trigger system is the event filter which reduces the event rate further to the recording rate of 200 Hz for subsequent offline analysis. The trigger itself uses offline analysis procedures with an event processing time of 4 s.

If a specific bunch collision is accepted by the whole trigger chain, the detector information of this collision are written to mass storage for further analysis. One collision, of course, can pass several trigger chains. It is important that one collision does not necessarily contain only one proton-proton interaction. Instead, per bunch crossing up to 25 interactions are expected, depending on the instantaneous luminosity. This is referred to as pile-up. For calibrating and monitoring often events are used which occur at a rather large rate compared to events of rare processes. In order to keep the recording rate of these events low the dedicated triggers have a pre-scale factor, N , applied. With this pre-scale factor only every N th event is recorded, finally.

For this work, the event filter `EF_e15_medium` is used, which quests for identified electrons of the class `Medium` (section 4.5.1) with a transverse momentum larger than $p_T = 15$ GeV. At luminosities of $\mathcal{L} = 10^{32} \text{ cm}^{-2} \text{ s}^{-1}$ this event filter has a rate of 20 Hz and is provided without a pre-scale factor [43].

4.4 Luminosity determination

The ATLAS experiment has three distinct detectors for luminosity determination. They are situated at ± 17 m (LUCID), ± 140 m (ZDC) and ± 240 m (ALFA) from the interaction point of the ATLAS experiment along the beam axis. The three detectors obtain the luminosity with different techniques and multiple algorithms. After calibration, the luminosities obtained differ approximately by $\pm 2\%$, whereas absolute luminosity calibrations have a common systematic uncertainty of $\pm 11\%$ [44].

The system closest to the interaction point, LUCID, is the main relative luminosity monitor of the ATLAS experiment. It is a Cerenkov detector (LUMinosity measurement using Cerenkov Integrating Detector) detecting inelastic p - p scattering in the forward direction. The main purpose of this detector is to provide online monitoring of the instantaneous luminosity and beam conditions on the one hand and the measurement of the integrated luminosity on the other. The LUCID detector is built of an array of sixteen optically reflecting gas-filled aluminum tubes, surrounding the beampipe. The working principle of LUCID is based on Cerenkov photons created by charged particle in the gas. The photons are reflected inside

the tubes until they reach photomultipliers at the end of the tubes. Luminosity determination is then accomplished through counting the numbers of tubes which deliver a signal above a preset threshold.

The ZDC detector (Zero-Degree Calorimeters) ought to determine the centrality of heavy-ions collisions by detecting forward neutrons with $|\eta| > 8.3$. Its modules consist of layers of alternating tungsten plates and quartz rods.

The luminosity detector with the largest distance to the interaction point of the ATLAS experiment is the ALFA detector (Absolute Luminosity For ATLAS). The detector consists of scintillating fibre trackers. They are located inside Roman pots which can be moved towards the beam as close as 1 mm. ALFA provides an absolute luminosity measurement via elastic scattering at small angles.

4.5 Particle reconstruction

The ATLAS detector response to a proton-proton collision is stored if it passes the full trigger chain. To derive physical objects like electrons from the output of the ATLAS data acquisition system, dedicated algorithms were developed. This software framework analyses and combines the signals of all detector components and thereby reconstructs and identifies physical objects. Algorithms important for this work are explained in the following.

4.5.1 Electron candidates

Electron candidates are detected by the ATLAS detector through a combination of signatures in the INNER DETECTOR and the ELECTROMAGNETIC CALORIMETER for central pseudorapidities of $|\eta| < 2.5$ [45]. With the standard algorithm they are reconstructed using a sliding window of 3×5 cells in the $\eta - \phi$ plane of the middle layer in the ELECTROMAGNETIC CALORIMETER. The sliding window searches for energy deposits above 2.5 GeV in the cluster of cells. With this, a preliminary set of seed clusters is created. Subsequently, the seed clusters are matched with tracks from the INNER DETECTOR of $p_T \geq 0.5$ GeV by extrapolation from the last measurement point of the inner tracking system to the second layer of the calorimeter. The quality of the match is given by the difference in the η - ϕ coordinates of the track measurement and the seed cluster. If more than one track matches the same seed cluster, the track of the highest match quality is considered. After the matching the electromagnetic cluster is recalculated with a sliding window of 3×5 (5×5) cells in the $\eta - \phi$ plane of the middle layer in the barrel (the end-caps). At this step also the cluster energy is recalculated with calibration factors such that reconstructed electrons are calibrated to the electromagnetic energy scale. The energy of an electron candidate is computed as a weighted average of the energy deposit in the cluster and the track momentum. For the direction in η and ϕ the corresponding track parameters are used.

Electrons of a low transverse momentum of a few GeV are reconstructed with the so-called soft algorithm. This technique makes use of tracks as a starting point which are then extrapolated to the calorimeter. The track impact point in the calorimeter is then used as a seed for cluster building. More details on this algorithm can be found in [40].

After the reconstruction of an electron candidate an identification procedure is applied. This step is necessary to suppress hadrons like pions traveling through the INNER DETECTOR and the ELECTROMAGNETIC CALORIMETER and therefore may be reconstructed as an electron candidate. To be identified as an electron object, the reconstructed electron candidate has to fulfil further requirements. This identification is done by a set of rectangular cuts, separated into three classes: **Loose**, **Medium** and **Tight** [45]. The algorithm used is driven to receive a high and uniform identification efficiency and to deliver a good separation between isolated electrons and fake signatures from QCD multijets or background electrons from photon conversions. For this, according cut values are optimised in bins of the transverse energy, $E_T = E/\cosh\eta$, and pseudorapidity. The identification procedure of **Loose** electrons makes use of shower shape variables and the hadronic leakage, which describes energy deposits beyond the ELECTROMAGNETIC CALORIMETER into the HADRONIC CALORIMETER. The algorithm for **Medium** electrons is based on the loose criterions and imposes additional requirements on the energy deposit in the strip layer of the ELECTROMAGNETIC CALORIMETER. Further, it sets conditions on the track quality and a track-cluster match. The **Tight** requirement utilises the full resources of the ATLAS detector and puts further demands on tracking characteristics and tightens the track-cluster matching. The variables to separate between the classes **Loose**, **Medium** and **Tight** are given in table 4.1.

Table 4.1: Variables used for the identification of electron candidates, separated into the identification classes **Loose**, **Medium** and **Tight**.

Loose class	
Acceptance of the detector	• $ \eta < 2.47$
Hadronic leakage	• Ratio of E_T in the first layer of the hadronic calorimeter to E_T of the electromagnetic cluster (used over the range $ \eta < 0.8$ and $ \eta > 1.37$)
	• Ratio of E_T in the hadronic calorimeter to E_T of the electromagnetic cluster (used over the range $ \eta > 0.8$ and $ \eta < 1.37$)
Second layer of electromagnetic calorimeter	• Lateral width of the shower
	• Ratio in η of cell energies in 3×7 versus 7×7 cells
Medium class (includes Loose)	
First layer of electromagnetic calorimeter	• Total shower width
	• Ratio of the energy difference associated with the largest and second largest energy deposit over the sum of these energies
Track quality	• Number of hits in the pixel detector (≥ 1)
	• Number of hits in the pixels and SCT (≥ 7)
	• Transverse impact parameter (< 5 mm)
Track matching	• $\Delta\eta$ between the cluster and the track (< 0.01)
Tight class (includes Medium)	
b-layer	• Number of hits in the b-layer (≥ 1)
Track matching	• $\Delta\phi$ between the cluster and the track (< 0.02)
	• Ratio of the cluster energy to the track momentum
	• Tighter $\Delta\eta$ cut (< 0.005)
Track quality	• Tighter transverse impact parameter cut (< 1 mm)
TRT	• Total number of hits in the TRT
	• Ratio of the number of high-threshold hits to the total number of hits in the TRT
Conversions	• Electron candidates matching to reconstructed photon conversions are rejected

4.5.2 Muon candidates

The muon reconstruction of this analysis is achieved by combining INNER DETECTOR tracks with MUON SPECTROMETER tracks under consideration of energy loss in the calorimeters. There are other algorithms which base on track reconstruction in either the INNER DETECTOR or the MUON SPECTROMETER and then extrapolate the tracks to the appropriate other detector component [40].

In the case that multiple candidates share the same track from either the INNER DETECTOR or the MUON SPECTROMETER, the muon reconstruction algorithm uses the minimal match chi-square value (χ^2) to decide which pair of tracks is chosen. The match chi-square value is defined as the difference between inner and outer track vectors weighted by their combined covariance matrix. To obtain a combined track vector a statistical combination of the inner and the outer track vector is used. Because of the acceptance of the inner tracking system this muon reconstruction algorithm is only valid in the range $|\eta| < 2.5$.

By combining measurements of the inner tracker system and the MUON SPECTROMETER for muon reconstruction a good momentum resolution over a wide range is accomplished. The inner tracking system provides the best momentum measurement at low to intermediate momenta up to 30 GeV. For higher momenta the MUON SPECTROMETER delivers best resolution. Furthermore, this algorithm suppresses backgrounds from pion escape of the calorimetry system and from pion or kaon decays in flight to a certain extent [35].

4.5.3 Heavy lepton candidates

Because of the rather high mass of τ -leptons of $m_\tau = 1.777$ GeV [5] and the short life time, the τ -lepton decays before interacting with the sensitive detector material. Possible decay modes and their branching ratios are given in table 5.1. The reconstruction of τ -leptons is therefore conducted through its decay products, which is either through light lepton detection or with a dedicated algorithm reconstructing hadronically decaying τ -leptons. The latter algorithm is described in detail in reference [46].

4.5.4 Jet reconstruction

As explained in section 2.1.1 partons being produced in proton-proton collision cannot propagate as free particles on large distances. Instead, they form so-called jets, bundles of hadrons which can also comprise light leptons from hadron decays. A more detailed explanation is given in section 3.1. The reconstruction of jets is mainly built on calorimeter entries of the HADRONIC CALORIMETER. There exist various algorithms for jet reconstruction [35]. For this study, jets reconstructed by the anti- k_t algorithm [47] are analysed.

The algorithm is based on noise-suppressed three-dimensional topological calorimeter energy clusters [48]. Topological clusters are built by collecting calorimeter cells around seed cells with an energy deposit, E_{cell} , significantly larger than the total

noise σ_{cell} , in particular $|E_{cell}| > 4\sigma_{cell}$. If the collected cells contain an energy deposit larger than $|E_{cell}| = 2\sigma_{cell}$, their direct neighbours are adjoint, as well. Finally all surrounding cells are collected to form the final cluster. If there exists more than one energy maximum on one cluster, the cluster is split into smaller clusters.

These topological clusters are the basis of the anti- k_t algorithm. The algorithm groups clusters in the inverse momentum space. The only variable of the algorithm is given by the distance R_r of two clusters in the rapidity- ϕ space. For this study, the distance parameter is chosen to be $R < -r = 0.4$. With the anti- k_t algorithm it is given that all clusters are assigned to exactly one jet. Furthermore, this algorithm is collinear- and infrared-safe⁴.

Topological clusters are calibrated to the electromagnetic energy scale which was obtained from test-beam measurements for electrons and muons in the ELECTROMAGNETIC CALORIMETER and HADRONIC CALORIMETER [49, 50]. Although its estimated energy deposit suits for electrons and photons, the energy scale for jets needs to be further calibrated. This calibration takes into account detector effects like energy loss in inactive regions or calorimeter non-compensation but also inefficiencies in energy clustering and jet reconstruction. For 2010 data this is accomplished using η and p_T dependent jet energy scale factors based on Monte Carlo simulation. The validation of the simulation was achieved with test-beam and collision data [51].

4.5.5 Transverse missing energy

Particles traversing the detector without interaction with the sensitive material cannot be detected and measured. Candidates for this are neutrinos, interacting only through the weak force, but also stable, weakly-interacting supersymmetric particles. Still, it is possible to give a lower threshold on their energies with the help of momentum conservation. For collider events the sum of the transverse momenta of the particles colliding is approximately zero. With the measurement of the momentum imbalance in the transverse plane the sum of the transverse momenta of the undetected particles can be estimated. The observable is called missing transverse energy and denoted with E_T^{miss} .

An estimator is given by the negative vector sum of all particles detected by the ATLAS detector. In more detail, it is reconstructed from energy deposits in the calorimeter, $\vec{E}_T^{\text{miss}}(\text{calo})$, and from reconstructed muon tracks, $\vec{E}_T^{\text{miss}}(\mu)$, [52]:

$$\vec{E}_T^{\text{miss}} = \vec{E}_T^{\text{miss}}(\text{calo}) + \vec{E}_T^{\text{miss}}(\mu) .$$

The calorimeter term consists of clusters associated to electrons, photons, jets (including hadronically decaying τ -leptons) calibrated to the appropriate scale. Clusters associated to hadronically decaying τ -leptons are calibrated to the hadronic energy scale, if their momentum exceeds $p_T > 20$ GeV. Furthermore, the energy lost by muons in the calorimeters and the energy of cells in topological clusters [48]

⁴Collinear- and infrared-safety is given if the output of the jet algorithm is robust against collinear particles and the addition of particles of low energy of the order ~ 1 MeV.

which cannot be associated to any reconstructed object is added. The second term of the $E_{\text{T}}^{\text{miss}}$ definition is the sum of the momenta of muon tracks reconstructed within the pseudorapidity range $|\eta| < 2.7$. If a muon is geometrically isolated (the distance to a jet is at least $\Delta R = 0.3$) the energy loss in the calorimeter is subtracted to avoid double counting.

5 Observation and Cross section measurement of $Z^0/\gamma^* \rightarrow \tau^+\tau^- \rightarrow e\mu + 4\nu$

5.1 Motivation

This chapter describes the measurement of the cross section times branching ratio¹ of the process $pp \rightarrow Z^0/\gamma^* \rightarrow \tau^+\tau^- \rightarrow \ell^+\ell^- + 4\nu$ in the mixed leptonic final state, where $\ell = e, \mu$. With this measurement several aims can be addressed.

One of the goals is to test Standard Model predictions by comparison of theoretical calculations of production cross sections with experimental measurements. The inclusive production of W and Z^0 bosons is a process offering this possibility. The total production cross section may be described as a convolution of the parton-parton cross section and momentum distribution functions (PDFs) of the partons inside the protons. Theoretical calculations give results in next-to-leading order (NLO) and next-to-next-to-leading order (NNLO) perturbation theory ([53] and [54] among others). Crucial ingredients to the phenomenological calculations are the PDFs, higher-order Quantum Chromodynamics (QCD) and electroweak radiative corrections, which can be tested through comparison with experimental measurements. The measurement at hand focuses on the inclusive process of the coherent sum of the photon γ^* and the Z^0 boson in the $\tau^+\tau^- \rightarrow e\mu + 4\nu$ decay channel.

An additional motivation provides the fact that the decay $Z^0/\gamma^* \rightarrow \tau^+\tau^-$ is the dominant background in Higgs boson searches in the $\tau\tau$ decay channel in the Standard Model and the Minimal Supersymmetric Standard Model (MSSM). The process $H \rightarrow \tau^+\tau^-$ is sensitive in the low Higgs boson mass region, yielding relatively high branching ratios for the decay to τ leptons as shown in figure 5.1. Most background contributions can either be obtained from data directly, like $t\bar{t}$, W + Jets and QCD multijet, or they yield very small contribution, like $WW/ZZ/WZ$. In case of the Higgs boson searches, the $Z^0/\gamma^* \rightarrow \tau^+\tau^-$ decay is irreducible because of the same final state and very similar decay kinematics. Therefore, its differential mass spectrum and normalisation have to be known precisely and must be well understood for searches of new physics. Figure 5.2 shows the $Z^0/\gamma^* \rightarrow \tau^+\tau^-$ decay as an irreducible background to $H \rightarrow \tau^+\tau^-$ in the MSSM model. As a consequence,

¹The branching ratio, BR , is the decay width of a specific decay channel with respect to the total decay width of a particle.

also the $Z^0/\gamma^* \rightarrow \tau^+\tau^-$ decay cannot be measured Higgs-signal free, in contrast to all other backgrounds. However, the expected number of Higgs events in the amount of $L = 35.51 \text{ pb}^{-1}$ being analysed are negligible for the unexcluded SM and MSSM parameter range.

One of the lower priorities of the cross section measurement of $Z^0/\gamma^* \rightarrow \tau^+\tau^- \rightarrow e\mu + 4\nu$ is to establish a proper functioning of the ATLAS detector.

The study was developed in cooperation with the official ATLAS study [55]. A similar analysis was performed in the diploma thesis [56]. The main difference of the three studies is the ansatz of the estimation of QCD multijet events from data.

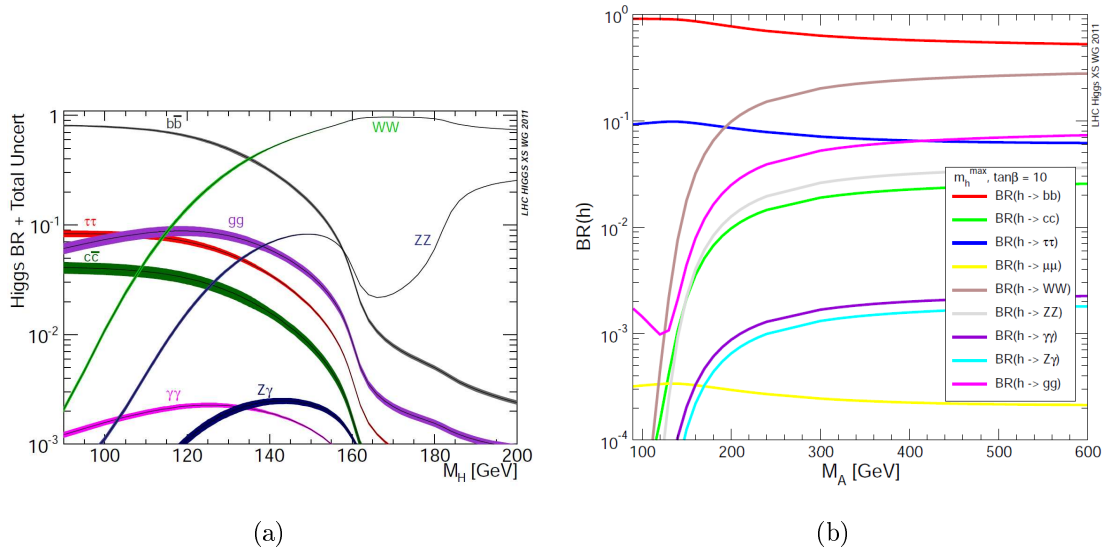


Figure 5.1: Branching ratios and their uncertainties for the SM Higgs boson (a) and branching ratios for the light MSSM Higgs boson (b). For the MSSM model the parameters are chosen according to the m_h^{max} scenario with $\tan\beta = 10$. The coloured bands give the uncertainty based on theoretical and parametric uncertainties [57].

5.2 Signal and background processes

5.2.1 Signal process

The present analysis describes the cross section times branching ratio measurement of the Z^0 boson decay to τ -leptons, which further decay into an electron-muon pair and four neutrinos. To be more precise, the measured process is $pp \rightarrow Z^0/\gamma^* \rightarrow \tau\tau \rightarrow e\mu + 4\nu$. On the basis of their observables the gauge bosons γ^* and Z^0 differ in their rest mass and their coupling structure to fermions,

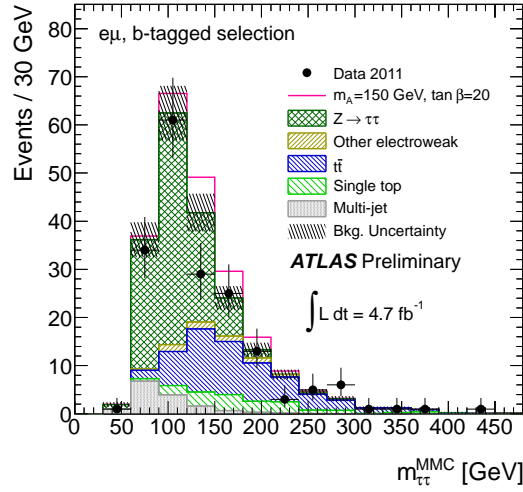


Figure 5.2: Reconstructed $m_{\tau\tau}$ mass of the $H \rightarrow \tau^+\tau^- \rightarrow e\mu + 4\nu$ final state in the MSSM. Parameters are chosen according to the m_h^{max} scenario with $\tan\beta = 20$ and $m_A = 150$ GeV [58].

only. In their appearance as intermediate particles of the process they are not on-shell (2.1.1), necessarily. Consequently, the analysis, not being sensitive on the fermion coupling structure of the intermediate particle, is not capable of distinguishing between them. It rather measures the coherent sum of the virtual photon, γ^* , and Z^0 boson.

The coherent sum Z^0/γ^* is produced from proton-proton collisions at the LHC through several production graphs. Figure 5.3 shows Feynman diagrams on tree level and a variety of graphs in next-to-leading order. The intermediate gauge bosons Z^0 and γ^* further decay into particle anti-particle pairs of quarks or leptons. Table 5.1 shows the branching ratios of the Z^0 boson. The decay mode with the highest branching ratio is the decay to a quark anti-quark pair with a share of 70%. It is followed by the invisible mode, the decay to a neutrino anti-neutrino pair, with 20%. From the electroweak theory it follows that the branching ratio for the three families of charged leptons is the same if mass effects are neglected. This is called lepton universality. The decay channel to charged leptons yields about 10% of the Z^0 decay.

Due to the short life time of the τ lepton it decays before interacting with the sensitive detector material. It is therefore detected via its decay products. Table 5.1 gives the possible decay modes and their branching ratios. The detection of τ -leptons in the ATLAS detector is therefore done either by light lepton detection or the measurement of hadrons (reference [46]), which come along as collimated jets. Further, the presence of missing transverse energy, E_T^{miss} , is required, because of the neutrinos being invisible to the detector.

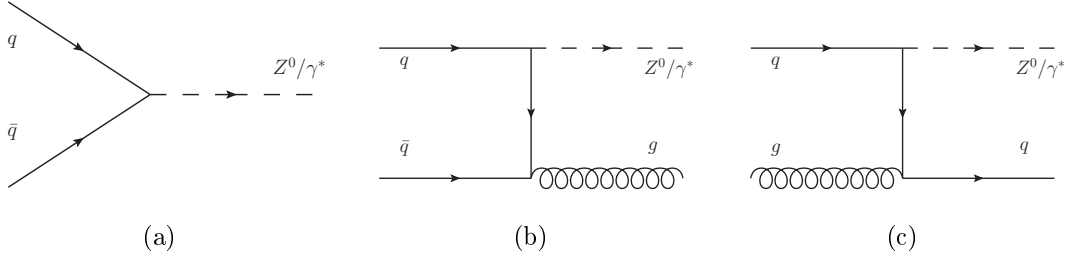


Figure 5.3: Possible Feynman graphs for the production of inclusive Z^0/γ^* in proton-proton collisions at the LHC on tree level (a) and in next-to-leading order (b) and (c).

Table 5.1: The decay modes and their branching ratios of the Z^0 boson (left side) and the τ lepton (right side) given by the PDG group [5].

Z^0 decay mode	branching ratio (%)	τ decay mode	branching ratio (%)
$Z^0 \rightarrow e^+e^-$	3.36	$\tau \rightarrow e\bar{\nu}_e\nu_\tau$	17.85
$Z^0 \rightarrow \mu^+\mu^-$	3.37	$\tau \rightarrow \mu\bar{\nu}_\mu\nu_\tau$	17.36
$Z^0 \rightarrow \tau^+\tau^-$	3.37	$\tau \rightarrow qq'\nu_\tau$	64.79
$Z^0 \rightarrow \nu\bar{\nu}$	20.00		
$Z^0 \rightarrow q\bar{q}$	69.90		

The fully leptonic decay chain leaves the final states:

$$\begin{aligned}
 Z^0/\gamma^* &\rightarrow \tau^+\tau^- \rightarrow e^+e^-\nu_e\bar{\nu}_e\nu_\tau\bar{\nu}_\tau \\
 Z^0/\gamma^* &\rightarrow \tau^+\tau^- \rightarrow e^\pm\mu^\mp\nu_{e,\mu}\bar{\nu}_{\mu,e}\nu_\tau\bar{\nu}_\tau \\
 Z^0/\gamma^* &\rightarrow \tau^+\tau^- \rightarrow \mu^+\mu^-\nu_\mu\bar{\nu}_\mu\nu_\tau\bar{\nu}_\tau
 \end{aligned}$$

This study concentrates on the measurement of the cross section times branching fraction of $Z^0/\gamma^* \rightarrow \tau^+\tau^-$ in the mixed leptonic final state $\tau^+\tau^- \rightarrow e\mu + 4\nu$. Due to a large background contribution from $Z^0/\gamma^* \rightarrow e^-e^+$ and $Z^0/\gamma^* \rightarrow \mu^-\mu^+$ at low masses, the same flavour decay channels are left out.

Theoretical calculations including NNLO QCD result in a cross section of

$$\sigma_{SM}(pp \rightarrow Z^0/\gamma^* \rightarrow \tau^+\tau^-) = 964 \pm 48 \text{ pb}$$

in the invariant $\tau\tau$ mass range of $66 \text{ GeV} \leq m_{\tau^+\tau^-} \leq 116 \text{ GeV}$ at the centre of mass energy of $\sqrt{s} = 7 \text{ TeV}$ for the Standard Model [59–61].

Events of the signal process are selected from the ensemble of measured data with rectangular cuts. The cuts are based on the kinematics and the event topology of the signal process. At leading order (figure 5.3(a)), the transverse momentum of the Z^0 boson is approximately zero since the transverse momenta of the incoming quarks are negligible. This means, that the τ -leptons are emitted back-to-back in

the rest-frame. Further, they gain a transverse momentum of $p_T \approx m_{Z^0/\gamma^*}/2$, which is much larger than their rest-mass of $m_\tau = 1.777$ GeV [5]. This circumstance leads to the fact, that the τ -lepton decay products gain a strong Lorentz-boost and are transmitted collinearly. The direction of flight of the electron or muon and their associated neutrinos point in the same direction. Additionally, the back-to-back topology is transferred to the electron-muon pair and their neutrinos. The vectorial sum of the transverse momenta of the lepton pair will be approximately zero. Though the momenta of the τ -leptons are large, the momenta of the electron and the muon are of a moderate range due to the present neutrinos of the final state. The leptons appear geometrically isolated in the detector, meaning that a specific region around the leptons is free of additional energy entries or tracks.

Interacting only through the weak force, the neutrinos leave the detector undetected. The variable of the missing transverse energy, E_T^{miss} , is utilised to address the missing energy of the neutrinos. Nevertheless, its value is rather small for $Z^0/\gamma^* \rightarrow \tau^+\tau^- \rightarrow e\mu + 4\nu$ events, keeping in mind that the variable is built of the vectorial sum of energy deposits in the calorimeter and reconstructed muon tracks. At higher orders of the Z^0/γ^* production, however, e.g. figure 5.3(b) and 5.3(c), additional quarks or gluons in the final state make the p_T of the Z^0 boson non-zero. This leads to an event topology with the electron-muon pair being not transmitted exactly back-to-back. Consequently, the vectorial sum of their momenta is larger than zero and with that also the value of the measured missing transverse energy. Still, the energy stemming from neutrinos is considerably higher. In summary, the measured values of the missing transverse energy underestimate the real transverse energy of the neutrinos. This circumstance makes it impossible to reconstruct the invariant mass of $Z^0/\gamma^* \rightarrow \tau^+\tau^-$ events. Hence, one of the challenges is to construct mass reconstruction methods, yielding a mass close to the invariant mass. Several approaches are discussed in chapter 6.

The electron and the muon of the final state are geometrically well isolated objects in the detector with a steeply decreasing transverse momentum distribution with $p_{T,e,\mu} \leq 50$ GeV.

5.2.2 Physics background

There exist several Standard Model processes in proton-proton collisions which can mimic the signal $Z^0/\gamma^* \rightarrow \tau^+\tau^- \rightarrow e\mu + 4\nu$ due to a similar event structure. They are called background processes. For the present work, they have two oppositely charged lepton candidates and missing transverse energy, E_T^{miss} , in the final state. Both signatures can be either real or fake. Fake lepton candidates arise from collimated QCD jets being misinterpreted as an electron or a muon. Fake E_T^{miss} originates from mismeasurements in the calorimeter or additional deposits in the calorimeter from additional proton-proton collisions. Potential background processes are the following:

- **QCD Multijet:** The QCD multijet background stems from processes producing quarks or gluons, which induce jets in the final state. It may yield either

real leptons from heavy flavour quark decays or fake leptons from charged hadrons being misinterpreted as lepton candidates. A pair of real or fake leptons may mimic the signal with two oppositely charged leptons. Although the rate of producing a fake lepton candidate from charged hadrons is rather low, the high cross section of QCD multijets at the LHC makes this process an important source of background events for all leptonic decay channels of $Z^0/\gamma^* \rightarrow \tau^+\tau^-$.

- **$Z^0/\gamma^* \rightarrow ee, \mu\mu + \text{jets}$:** In particular the low mass range of the coherent sum Z^0/γ^* with an off-shell Z^0 or a virtual photon mimics the signal. In this mass regime the energy of the leptons is in the range expected from the signal. Given that Z^0/γ^* decays into two real oppositely charged leptons of the same flavour, this background becomes important, if additional jets are present. Similar to the QCD Multijet background, the jets may potentially fake leptons or contain leptonically decaying hadrons.
- **$W^\pm \rightarrow e^\pm\nu_e, \mu^\pm\nu_\mu + \text{jets}$:** When decaying leptonically, W bosons with additional jets represent a background. Again, the additional jets may be misidentified as lepton candidates. Their lepton flavour is uncorrelated to the lepton flavour of the W decay. However, the fake rate of jets for electrons being higher than for muons, the background $W^\pm \rightarrow \mu^\pm\nu_\mu + \text{jets}$ plays a more important role.
- **$W^\pm \rightarrow \tau^\pm\nu_\tau + \text{jets}$:** In contrast to the previous sources of backgrounds, the decay product of this channel, a τ lepton, decays further. In most of the cases it decays hadronically, mainly producing charged pions or kaons. Those can then provide fake lepton candidates. In addition, the τ lepton can also decay leptonically producing real electrons or muons. For both cases, additional jets have to be present to mimic the signal, producing the second lepton from real or fake source.
- **$t\bar{t}$:** The fully leptonic decay of top and anti-top quarks form a direct background source to the signal. Furthermore, the semi-leptonic and the fully hadronic $t\bar{t}$ decay mode may imitate the signal when having at least one or two additional jets in the fiducial region. Again, the jets can provide real or fake lepton candidates.
- **Weak diboson production:** The production of pairs of W bosons, WW , form a direct background if both bosons decay leptonically. In the leptonic decay mode of the boson pairs, WZ and ZZ , some of the leptons must stay undetected in order that the diboson decay yields a background source. However, with their cross section being very small, their contribution as a background is negligible for this study.

5.2.3 Monte Carlo simulation

The background processes discussed above are simulated at a centre of mass energy of $\sqrt{s} = 7$ TeV using Monte Carlo techniques. The response of the ATLAS detector to particles is simulated with GEANT4 [29, 62]; the decay of the τ lepton is simulated using TAUOLA [63]. All backgrounds used, except for $t\bar{t}$, are generated using PYTHIA v6.423 [22]. This generator conducts the event generation, initial and final state radiation as well as the hadronisation. The $t\bar{t}$ sample was generated using MC@NLO v3.3 [64]. For the generation of the parton shower and the hadronisation, the sample is interfaced to HERWIG [65]. Both generators are interfaced with PHOTOS [66], a programme which simulates the effect of final state QED radiation. The samples generated with PYTHIA resort to the PDF set MRST2007LO* [67], while the MC@NLO samples makes use of the CTEQ6.6 [68] set of PDFs.

For all samples the ATLAS MC10 tune [69] was used. It makes use of the knowledge gathered from the ATLAS data collected in 2010. Further, they were simulated with pile-up events² being overlaid on top of the hard scattering event. The average number of simulated additional proton-proton interactions per bunch crossing is chosen to be Poisson distributed with an expectation value of 2.2.

The cross sections used for the W and the high mass Z^0 background samples are calculated at NNLO [59–61], not including electroweak corrections. They were calculated using FEWZ [54, 70]. The $t\bar{t}$ sample is normalised to reproduce the cross section calculated at approximate NNLO precision [71, 72], which was retrieved under the usage of the heavy quarks cross section calculator HATHOR [73]. A summary of the samples used, providing the generator they were made with, their corresponding cross section times branching ratio and the filter efficiency, f , on generator level³ is given in table 5.2. The background from QCD multijet events is not evaluated using Monte Carlo simulated samples but rather estimated from data. This method is discussed in section 5.8.1. This step is mandatory due to the large cross section of QCD multijet events, which make the generation of the corresponding Monte Carlo samples and especially the simulation of the ATLAS detector response and the reconstruction of all particle objects too time consuming.

5.3 Analysis strategy

The common approach to make an observation of a process or measure a characteristic in particle physics of the high energy regime is the usage of simulated Monte Carlo pseudo data. Besides the signal process, processes which mimic the event topology of the signal need to be considered. They are usually estimated using Monte Carlo simulations, but can also be derived directly from data. These processes are called background processes and are on the one hand processes which have a very similar event structure like the signal. On the other hand, these can also be

²With pile-up multiple proton-proton interactions per bunch crossing are denoted (section 4.3).

³Some processes are generated in a certain phase space of interest. The efficiency of such a filter is given by the number f .

Table 5.2: Summary of the Monte Carlo simulated samples, their corresponding cross section, σ , times branching ratio, BR, and the filter efficiency, f , on generator level. The cross sections are given for each of the given flavours, separately.

Dataset	Generator	$\sigma \times \text{BR}$ [pb]	f (%)
$W^\pm \rightarrow \ell^\pm \nu_\ell$ ($\ell = e, \mu, \tau$)	Pythia	10460	100
$Z^0/\gamma^* \rightarrow \ell^+ \ell^-$ ($m_{\ell\ell} \geq 60$ GeV, $\ell = e, \mu, \tau$)	Pythia	990	100
$Z^0/\gamma^* \rightarrow \ell^+ \ell^-$ ($m_{\ell\ell} \in [15 - 60]$ GeV, $\ell = e, \mu$)	Pythia	1462	100
$Z^0/\gamma^* \rightarrow \ell^+ \ell^-$ ($m_{\ell\ell} \in [10 - 60]$ GeV, $\ell = \tau$)	Pythia	3967	100
$t\bar{t}$	MC@NLO	165	55.6

processes being misidentified as the signal process by misreconstruction of objects in the detector. Taking into account the design concept of the detector, mismeasurements and misreconstructions should be rare. Nevertheless, they become relevant if the cross section of the background process is considerably larger than the signal process cross section.

Cuts are applied on distributions of event and object variables to enrich events of the signal process and suppress the ensemble of background events. In the present work, rectangular cuts are used. Alternative approaches are for example machine learning methods, but are not required for the given signal process. The cuts need to be optimised with the help of simulated Monte Carlo data of signal and background processes. The optimisation is implemented in terms of a figure of merit, quantifying the performance of the signal enrichment over the background suppression.

The figure of merit is built from the ansatz that a hypothetical ensemble of n_{ens} events is Poisson distributed. The likelihood to select a random number of n events from the ensemble is given by the following probability density function (PDF):

$$\mathcal{L}(n, n_{ens}) = \frac{e^{-n_{ens}} \cdot n_{ens}^n}{n!} \quad (5.1)$$

One can establish two hypotheses. Either, that the ensemble of n_{ens} events comprises events from background processes only, or that n_{ens} consists of events from the signal and background processes:

- signal hypothesis $n_{ens} = s + b$
- background only hypothesis $n_{ens} = b$

Using Wilks theorem [74] an observable can be built out of the two hypotheses $\mathcal{L}(n, s+b)$ and $\mathcal{L}(n, b)$ through a Likelihood ratio:

$$\begin{aligned}
 \lambda(n) &= -2 \ln \frac{\mathcal{L}(n, s+b)}{\mathcal{L}(n, b)} \\
 &= -2 \ln \frac{e^{-(s+b)}(s+b)^n/n!}{e^{-b}(b)^n/n!} \\
 &= -2 \ln \left(e^{-s} \left(\frac{s+b}{b} \right)^n \right) \\
 &= 2s - 2n \ln \left(\frac{s+b}{b} \right)
 \end{aligned} \tag{5.2}$$

The mean, $\langle \lambda \rangle$, and the variance, $V(\lambda)$, of equation (5.2) are:

$$\langle \lambda \rangle = -2 \langle n \rangle \ln \left(\frac{s+b}{b} \right) \tag{5.3}$$

$$V(\lambda) = \sigma^2(\lambda) = 4\sigma^2(n) \left(\ln \frac{s+b}{b} \right)^2 \tag{5.4}$$

The figure of merit is then constructed by the following ansatz. For a precise measurement of signal events, s , the expected statistical uncertainty which is given as $\sqrt{s+b}/s$ is ought to be minimal. Accordingly, the reciprocal should be maximal. With equations (5.2), (5.3) and (5.4) and the assumption that the selected random number of $n = s+b$ events is Poisson distributed, the reciprocal can be translated into:

$$\begin{aligned}
 \Sigma &= \frac{\langle \lambda_b \rangle - \langle \lambda_{s+b} \rangle}{\sigma_{s+b}(\lambda)} \\
 &= \frac{-2 \langle b \rangle \ln \frac{s+b}{b} + 2 \langle s+b \rangle \ln \frac{s+b}{b}}{\sqrt{4 \left(\ln \frac{s+b}{b} \right)^2 \sigma^2(s+b)}} \\
 &= \frac{s}{\sqrt{s+b}}
 \end{aligned} \tag{5.5}$$

The established analysis is optimised by means of the figure of merit $\Sigma = \frac{s}{\sqrt{s+b}}$ with the help of simulated Monte Carlo data and then applied on recorded experimental data. The computer code was developed on the basis of SFrame [75, 76].

5.4 Experimental data and quality criteria

The data used for this analysis was recorded by the ATLAS detector from July to October 2010 at a centre of mass energy of 7 TeV. They were processed during the ‘‘Autumn 2010 Reprocessing’’ campaign, making use of ATHENA⁴ release 16.0.2.3.

⁴ATHENA is the software framework of the ATLAS detector (see section 3.2).

The data recorded is separated in units of so called luminosity blocks which have a duration of approximately two minutes [77]. To ensure the use of good quality data only, several requirements are made on the luminosity blocks. They are combined in the GoodRunsList (GRL) created by the WZ physics group [78]. This guarantees that all parts of the detector necessary for this analysis were fully operational, that stable beam condition has been declared by the LHC operators and ATLAS data taking was underway. In detail, the flags of the GoodRunsList include global ATLAS stability flags and ensure that the magnetic fields of the solenoid and torroid magnets were fully established, reliable luminosity values were available, that a selected set of triggers from Level 1 and High-Level Triggers (section 4.3) are functioning. They further demand that the quality of data from detector components, necessary for muon and electron reconstruction, was guaranteed and the detector response values necessary for the E_T^{miss} calculation behave as expected. The chosen data includes the data taking periods E4 to I, each of them of approximately one month length. Their luminosity is calculated with the official ATLAS web-based tool [77, 79] (`Of1Lumi-7TeV-002`) considering the GRL used and the trigger described in section 5.6.2. The luminosity retrieved had to be corrected by a factor of 0.964 due to an updated luminosity determination [80]. This results in an integrated luminosity of $L = 35.51 \text{ pb}^{-1}$. Data taking periods before E4 were not taken into account because of rapidly varying trigger conditions and to avoid the usage of prescaled triggers⁵. This leads to a loss of only 0.2% of the total luminosity.

5.5 Object selection

Electrons

For this analysis, electrons of the class `Medium` are utilised. They are geometrically well isolated of other objects with a transverse momentum of approximately $p_T \leq 50 \text{ GeV}$. The reconstruction and identification algorithms are explained in section 4.5.1. Alignment differences seen in the 2010 ATLAS data [81] are taken into account. The reconstruction and identification efficiency for electrons chosen with these requirements is approximately 89%. To make use of information from the inner tracking system, the pseudorapidity range is set to $|\eta| < 2.47$, excluding the transition region between the barrel and the end-cap calorimeters, $1.37 < |\eta| < 1.52$. Furthermore, the electron cluster must exceed a transverse energy of $E_T > 16 \text{ GeV}$ to ensure that reconstruction and trigger efficiencies are well understood. The electron candidate must be reconstructed by the standard or the soft electron algorithm (section 4.5.1). Finally, information about readout problems or non-nominal high voltage conditions in the calorimeter, stored as $\eta \times \phi$ maps, are used to avoid electrons built from a cluster affected by detector problems. The $\eta \times \phi$ map corresponding to the data taking period with the highest integrated luminosity is chosen to represent

⁵A pre-scale factor N ensures that only every N th event passes the trigger chain (section 4.3). This is used to reduce the recording rate of events from processes of a high event rate.

all data periods.

The electron's four vector is built from calorimeter and track information; specifically, the energy component is given by the electron calorimeter cluster while the direction is given by the electron track. In the case of the selection of the pseudorapidity range and the restriction to electrons from calorimeter regions without detector problems, the four vector is built from electron calorimeter cluster information, only, as they demand the electron position in the calorimeter.

Muons

Similarly to the electrons, muons considered in this analysis are geometrically well isolated of other objects with a transverse momentum of approximately $p_T \leq 50$ GeV. Muon candidates are built by combining INNER DETECTOR tracks with MUON SPECTROMETER tracks under consideration of energy loss in the calorimeters. The algorithm is explained in section 4.5.2 in more detail.

The MUON SPECTROMETER forms the outermost part of the detector. All other parts are built in a way that they not only can identify a specific class of particles but also make them stop in the detector part they are identified in. As a result, only muons should be able to travel through the whole detector, reaching the MUON SPECTROMETER. Nevertheless, the possibility exists that highly-energetic particles travel through the INNER DETECTOR and the calorimeter systems without being stopped. For this reason and to suppress muons from cosmic rays or decaying hadrons, there exist various supplementary cuts on the muon candidates. First, the difference, z_0 , between the z position of the muon track extrapolated to the beam line and the z position of the primary vertex must be less than 10 mm. This cut mainly reduces contamination from cosmic muons. Furthermore, there are quality criteria on INNER DETECTOR tracks which ensure the muon candidate to be well reconstructed and which suppress fake tracks and discriminate muons coming from hadrons decaying in flight. These cuts are constructed such, that detector conditions are taken into account, especially dead or uninstrumented regions. In particular, at least one hit in the pixel b-layer is required except when the extrapolated muon track passed an uninstrumented or dead area of the b-layer. The sum of the number of hits in the pixel detector plus the number of crossed dead pixel sensors have to be at least one. The sum of the number of hits in the SCT detector (section 4.2.2) plus the number of dead SCT modules crossed should exceed six. The sum of crossed dead pixel sensors plus crossed dead SCT modules should be less than two. Furthermore, a successful extension to the TRT detector (section 4.2.2) where expected is required. This means that within the angular region $|\eta| < 1.9$ the sum of the hits in the TRT and outliers on the track must be larger than five and the ratio of TRT outlier hits to the total number of TRT hits must be less than 0.9. Track outliers represent detector measurements which could not be associated to a reconstructed track or give an unfavourable match χ^2 . If the muon track is outside that angular region, the ratio of TRT outlier hits to the total number of TRT hits must be less than 0.9, but only if the sum of the TRT hits and outliers on the track is larger than five. Finally, the pseudorapidity range of muons is set to $|\eta| < 2.4$ and their

transverse momentum must exceed $p_T > 10$ GeV.

Jets

Jet candidates are reconstructed using the anti- k_t algorithm with a distance parameter of $R_r = 0.4$. A detailed explanation of the reconstruction algorithm and the calibration of jets is given in section 4.5.4. Identified jet candidates are required to have a transverse momentum of $p_T > 20$ GeV and a pseudorapidity of $|\eta| < 4.5$.

Resolving overlap ambiguities

The algorithms used to reconstruct and identify objects passing the ATLAS detector are constructed in view of efficiency and low fake rates. One object may however be identified by two different algorithms. To resolve these ambiguities and give each object a unique hypothesis, a procedure of ordering with priorities of overlapping objects is introduced. The procedure uses the distance between objects built from the azimuthal angle ϕ and the pseudorapidity η as $\Delta R = \sqrt{\Delta\phi^2 + \Delta\eta^2}$. If objects of the same class overlap, then the one with the higher transverse momentum is selected. If objects of different classes overlap, they are selected in the following order: muons, electrons, jets, considering that leptons are selected with a higher purity. To summarise:

- a muon is selected if it overlaps with a muon or an electron within $\Delta R < 0.2$ or a jet within $\Delta R < 0.4$,
- an electron is selected if it overlaps with an electron within $\Delta R < 0.2$ or a jet within $\Delta R < 0.4$,
- a jet is selected if it overlaps with another jet within $\Delta R < 0.4$.

Missing Transverse Energy

The reconstruction of missing transverse energy is based upon energy deposits in the calorimeter and on reconstructed muon tracks. A detailed explanation of the method is given in section 4.5.5.

Vertices

Event vertices are required to have at least three associated tracks. With this specification, the perspective to select vertices from proton-proton collisions rather than from cosmic muons or other sources is enhanced. The algorithm to find vertices extrapolates tracks to the beam pipe and looks for regions with high track densities. Cosmic muons traversing the detector will leave one track through the whole detector. This track will be misinterpreted as two tracks coming from one vertex at the beam axis. Therefore, the requirement of the vertex to have at least three associated tracks suppresses the background from cosmic muon events.

5.6 Event selection

5.6.1 Vertex multiplicity

To ensure a selection of only proton-proton collisions, each event is required to contain at least one reconstructed vertex fulfilling the selection requirements described in section 5.5.

5.6.2 Trigger

For this analysis, the specific trigger to select events out of the recorded experimental data ensemble should remain unrescaled over the whole data taking period considered. Furthermore, it should give a high efficiency, meaning that the turn-on curve for triggered objects is steep, and indicate a fully understood behaviour verified with earlier measurements. As stated in section 5.2.1, the analysis concentrates on the mixed leptonic final state $Z^0/\gamma^* \rightarrow \tau^+\tau^- \rightarrow e\mu + 4\nu$. Due to the limited geometrical coverage of the muon trigger system, the efficiency of muon triggers is marginally lower than that for electrons. Consequently, a single electron trigger `EF_e15_medium` is preferred. The event filter will search for identified electrons of the class `Medium` (section 5.5) with a transverse momentum larger than $p_T = 15$ GeV. At peak luminosities of $\mathcal{L} = 10^{32} \text{ cm}^{-2}\text{s}^{-1}$ the corresponding rate of this trigger is 21.2 s^{-1} [82], making it possible to run unrescaled throughout the data taking periods E4 to I. For electrons with a transverse momentum of $p_T > 16$ GeV the turn-on curve of the trigger has a moderate impact, only (figure 5.9). In the range of $16 \text{ GeV} \leq E_T < 18 \text{ GeV}$ 96% of the electrons are kept, rising to 97% in the range of $18 \text{ GeV} \leq E_T < 20 \text{ GeV}$. For electrons with $E_T > 20 \text{ GeV}$ the trigger efficiency reaches 99% (table 5.5). Keeping in mind that the transverse momentum has a steep decreasing distribution with most of the electrons yielding $p_T \leq 50 \text{ GeV}$, the event filter `EF_e15_medium` is the lowest possible value for electrons to be triggered on for the observed data taking period while preserving a high signal yield.

5.6.3 Jet cleaning

During data taking it may happen that localised high-energy calorimeter deposits not coming from beam-beam interactions are registered by the ATLAS detector. Possible sources are either cosmic ray muons undergoing a hard bremsstrahlung, other non-collision background, or hardware detector effects, like unexpected discharges in the liquid argon gaps of the endcaps of the HADRONIC CALORIMETER or coherent noise in the ELECTROMAGNETIC CALORIMETER. Although these incidents occur rarely, they disturb the E_T^{miss} measurement significantly. Therefore, dedicated cleaning requirements were derived from the full amount of data recorded by the ATLAS detector in 2010 [83]. They are obtained through the characteristics of the perturbation sources. Cleaning requirements against hardware effects are based on the quality of the registered energy deposits. The detector pulses must

agree with the expected pulse shape for electromagnetic energy deposits. In contrast, cleaning requirements against cosmic ray muons or other non-collision background rely on the comparison of calorimeter timing information with expected bunch crossings of protons. Furthermore, they are based on the fact that non-collision background, like interactions of protons with the residual gas within the beam pipe, mainly traverses the detector parallel to the beam-pipe and therefore emits its energy in one calorimeter layer only.

For the present study, the cleaning requirements are applied to jets with a transverse momentum larger than $p_T = 20$ GeV being reconstructed by the anti- k_t algorithm with a distance parameter of $R_r = 0.4$. In the following the cleaning procedure is specified and ordered by the source of the localised high-energy deposits.

- Discharges in the endcaps of the HADRONIC CALORIMETER
 - If more than 50% of the jet's energy is stored in the hadronic endcap (HEC), more than 50% of that energy must be stored in cells showing the predicted pulse shape.
 - The negative energy of a jet, resulting from the calibration to the jet energy scale, must not be greater than 60 GeV.
- Coherent noise in the ELECTROMAGNETIC CALORIMETER
 - If the fraction of the energy deposit of a central jet ($|\eta| < 2.8$) stored in the ELECTROMAGNETIC CALORIMETER exceeds 95%, less than 80% of the energy must be stored in cells not showing the predicted pulse shape.
- Cosmic ray muons, other non-collision background
 - The specific jet time, calculated as an energy weighted average of the timing information of all associated calorimeter cells with respect to the collision timing, must be smaller than 25 ns .
 - A variable addressing the momenta of associated tracks with respect to the jet momentum is the jet-track fraction. In detail, it corresponds to the sum of the transverse momenta of associated tracks of the jet relative to the calibrated jet p_T : $\sum p_T^{tracks} / p_T^{jet}$. If for central jets ($|\eta| < 2.0$) the jet-track fraction is smaller than 5%, at least 5% of the energy fraction must be deposited in the ELECTROMAGNETIC CALORIMETER.
 - Central jets ($|\eta| < 2.0$) must not contain more than 99% of their energy in one calorimeter layer.
 - For non-central jets ($|\eta| \geq 2$), the energy fraction in the ELECTROMAGNETIC CALORIMETER must exceed at least 5%.

If reconstructed and selected jets, which are not overlapping with selected electrons or muons in the $\eta - \phi$ space (section 5.5), fulfil the cleaning requirements, the considered event is kept. The cleaning procedure is applied to experimental data only, but not on simulated Monte Carlo samples. This procedure is chosen, as most

of the jet's quantities utilised for the cleaning are simulated with some inaccuracy. Its systematic uncertainty is described in section 5.10.

5.6.4 Selection of a lepton pair

Once an event is selected, which means it is triggered on, fulfils the requirements on the vertex multiplicity and the jet cleaning, it is required to contain a lepton pair. The lepton pair must exist of exactly one reconstructed muon and exactly one identified and reconstructed electron with opposite electric charge. The p_T and η distribution of the selected electrons and muons after the isolation requirement (section 5.6.6) are shown in figure 5.4.

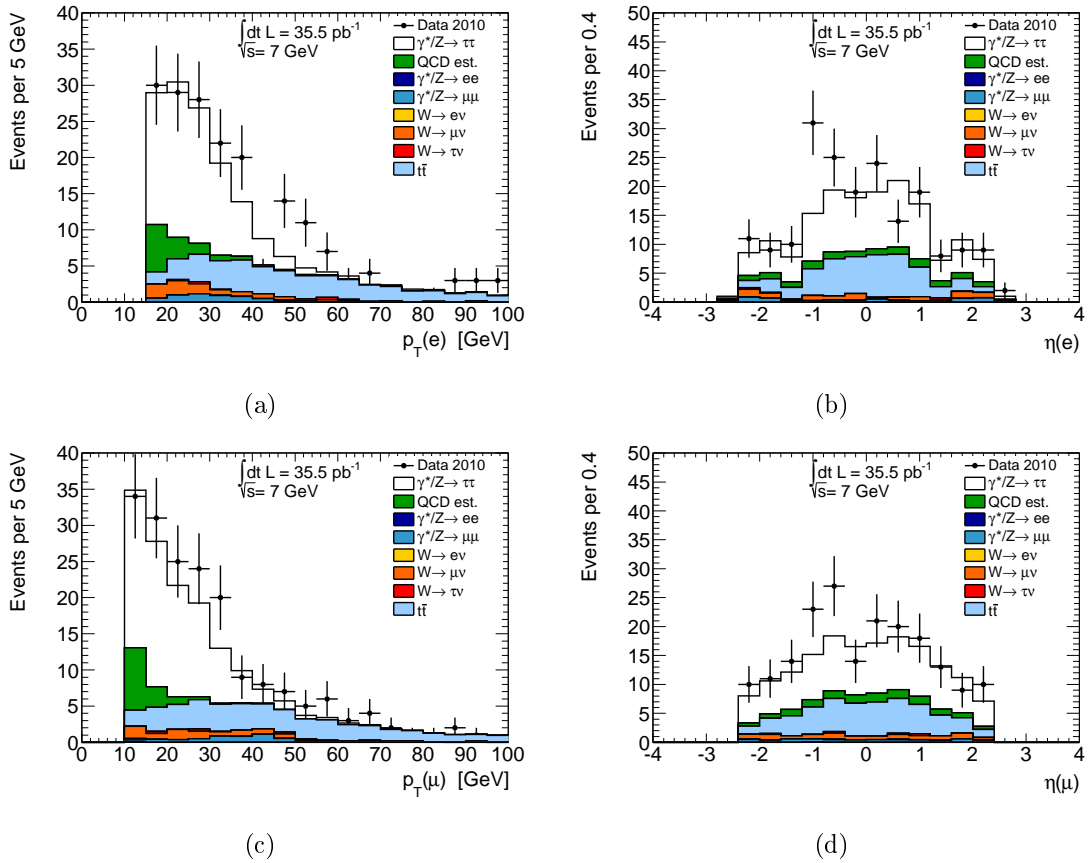


Figure 5.4: Kinematic variables of the selected leptons after the selection of an isolated electron-muon pair of opposite electric charge. Shown are selected events of data recorded in 2010, the signal process $Z^0/\gamma^* \rightarrow \tau^+\tau^-$ and its corresponding background samples (compare reference [56], figure 5.4 (a) to (d)). The amount of QCD multijet events is estimated from data as described in section 5.8.1.

5.6.5 Electron energy scale correction

The electron energy scale needs to be corrected in recorded experimental data. This is achieved with a set of correction factors binned in pseudorapidity. They are obtained by selecting $Z^0/\gamma^* \rightarrow e^+e^-$ events with 2010 data recorded by the ATLAS detector with an integrated luminosity of $L = 40 \text{ pb}^{-1}$. The basis electromagnetic energy scale was obtained from test beam measurements [84]. With the determination of a set of correction factors, α , the energy scale is improved as $E_{\text{corr}} = \frac{E_{\text{meas}}}{1+\alpha}$. They are derived by selecting $Z^0/\gamma^* \rightarrow e^+e^-$ events and fitting the mass distribution of the Z^0 boson with a logarithmic likelihood ratio [81]. Input parameters are the number of selected $Z^0/\gamma^* \rightarrow e^+e^-$ decays, the regions the electrons travel to, the measured di-electron mass and the probability density function quantifying the Z^0 mass lineshape. The energy scale correction factors are derived in 58 bins of η . Because of a lack of statistics of $Z^0/\gamma^* \rightarrow e^+e^-$ decays in 2010 data the intercalibration along ϕ is not considered. In figure 5.5 the spread of α along η is depicted, showing a $\pm 2\%$ variation in the barrel region. The variations along η are a result of the transition regions of the ELECTROMAGNETIC CALORIMETER. After a correction of the electron energy scale, the modification needs to be propagated to the value of the missing transverse energy, $E_{\text{T}}^{\text{miss}}$, as well. The linearity and resolution of the energy scale correction factors are verified with selected $J/\psi \rightarrow e^+e^-$ events. The results are used to obtain the uncertainty of the electron energy scale [81].

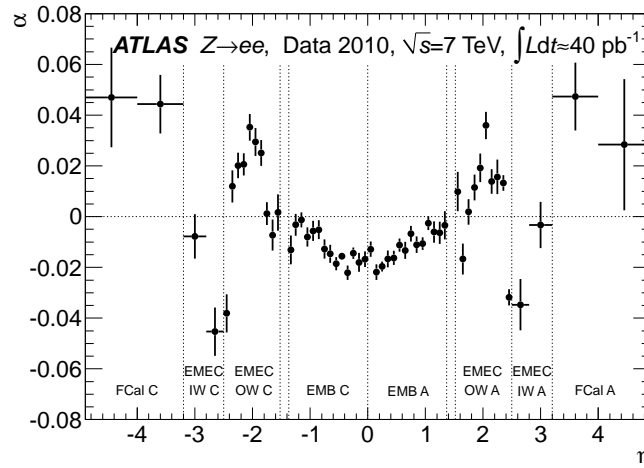


Figure 5.5: Display of the electron energy scale correction factors, α , needed to correct the electron energy scale in experimental data, $E_{\text{corr}} = \frac{E_{\text{meas}}}{1+\alpha}$ [81].

5.6.6 Isolation of leptons

The leptons of the $Z^0/\gamma^* \rightarrow \tau^+\tau^- \rightarrow e\mu + 4\nu$ decay traverse the detector as geometrically well isolated objects. Cutting on the isolation of leptons, background from QCD multijet events can be strongly reduced. Leptons from QCD multijets may be either real from a decaying heavy flavour quark or fake from charged hadrons being misinterpreted as lepton candidates. In either case, the lepton from QCD multijets is surrounded by a bundle of light hadrons composing a jet. Therefore, isolation variables are built by investigating the transverse energy or the transverse momentum around the lepton. The isolation variables are split into calorimeter and track isolation. In detail, for the calorimeter isolation a cone in the $\eta - \phi$ plane around the lepton is chosen in which the transverse energy of the cells around the lepton is summed up. For the track isolation the transverse momentum of tracks in a cone around the lepton in the INNER DETECTOR is taken into account. For both variables, the energy or momentum of the lepton itself is omitted in the sum but utilised to normalise it. The energy or momentum value which can be measured more precisely is applied for the normalisation. For electrons this is the transverse energy, whereas for muons it is the transverse momentum. Well isolated leptons, for which there is no or little additional detector activity in the chosen cone, yield a value for the isolation variable which is small. Further, the larger the chosen cone with a constant value of the isolation variable, the more isolated is the lepton.

For an optimisation of the isolation cuts, the isolation between the leptons of the $Z^0/\gamma^* \rightarrow \tau^+\tau^- \rightarrow e\mu + 4\nu$ decay is neglected. Therefore, the isolation of the electron and the muon is examined separately. Considering the fact that the aim of this analysis is the measurement of a cross section in contrast to a search, the isolation is optimised in terms of the figure of merit $\Sigma = s/\sqrt{s+b}$, with s being the number of signal events and b the number of events from background sources. A mixture of the calorimeter isolation, $E_T^{cone}/p_{T\mu}$ in the muons case and E_T^{cone}/E_{Te} in the electron case, and the track isolation variable, p_T^{cone}/p_{Tlep} , is utilised. For the cone around the lepton the values $\Delta R = \sqrt{(\Delta\eta)^2 + (\Delta\phi)^2} = 0.2, 0.3, 0.4$ are examined. The optimisation uses recorded experimental data as described in section 5.4 plus the simulated signal and background Monte Carlo samples listed in table 5.2. Events are selected with the standard selection of the analysis (table 5.6) up to the selection of one lepton pair. The ensemble of signal events, utilised for the calculation of the figure of merit, is represented by selected events of the $Z^0/\gamma^* \rightarrow \tau^+\tau^-$ Monte Carlo sample with a theoretical cross section times branching ratio of $\sigma = 990$ pb. The yield of $Z^0/\gamma^* \rightarrow \tau^+\tau^-$ events is 2% at this point.

The ensemble of background events is represented by selected data events. At this step of the selection procedure they are dominated by QCD multijet events with a share of 93%. Nevertheless, leptons from electroweak background processes and decays of top anti-top quark pairs contain isolated leptons as well. For this reason, this simulated background Monte Carlo samples, namely $W^\pm \rightarrow \ell^\pm \nu_\ell$, $Z^0/\gamma^* \rightarrow \ell\ell$ and $t\bar{t}$, with $\ell = e, \mu, \tau$, are subtracted from the selected data events. With this ansatz it is possible to optimise the isolation cuts with experimental data, instead of using simulated Monte Carlo samples of QCD multijet events.

This approach does not take into account fake leptons from the electroweak and $t\bar{t}$ background samples (section 5.2.2) as they are subtracted. Instead, the procedure is optimised to suppress leptons from QCD multijet events. Furthermore, the theoretical cross section of the $Z^0/\gamma^* \rightarrow \tau^+\tau^-$ signal is utilised, which is the value to be measured.

The most efficient isolation cuts for the electron and the muon are derived through a scan in the $E_T^{\Delta R}/p_{Tlep} - p_T^{\Delta R}/p_{Tlep}$ plane (figure 5.6). The points with the highest figure of merit are specified in table 5.3. The figure of merit increases with the size of the cone around the lepton, as expected. Consequently, the most efficient isolation for the muon is achieved by cutting on

$$E_T^{0.4}/p_{T\mu} < 0.055 \text{ and } p_T^{0.4}/p_{T\mu} < 0.085.$$

A separate study [55] revealed, that for electrons the isolation variable $E_T^{\Delta R}/E_{Te}$

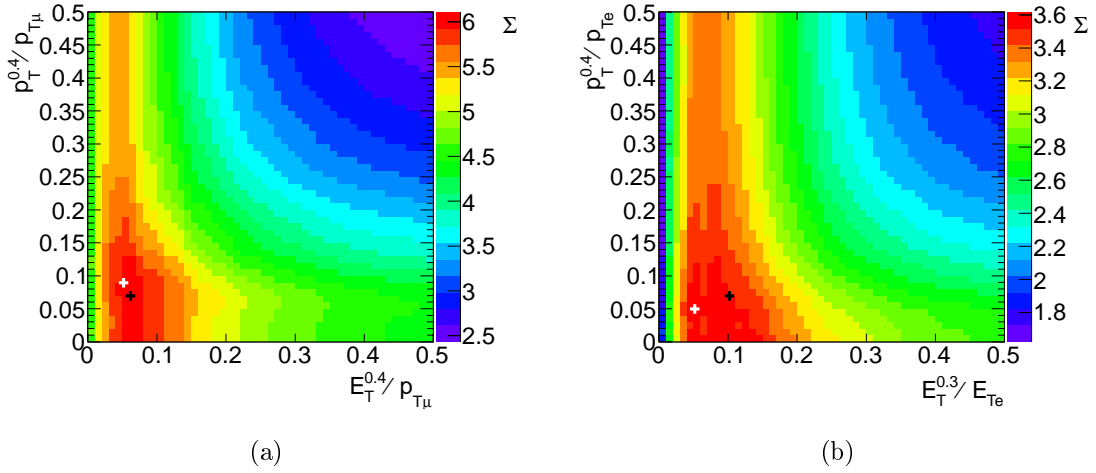


Figure 5.6: Distribution of the figure of merit $\Sigma = s/\sqrt{s+b}$ in the $E_T^{0.4}/p_{T\mu} - p_T^{0.4}/p_{T\mu}$ plane for muons (a) and the $E_T^{0.3}/E_{Te} - p_T^{0.4}/p_{Te}$ plane for electrons (b). The established cut optimum for muons is at (0.055, 0.085), for electrons (0.055, 0.045), highlighted as a white cross. For reasons of combination with the semi leptonic $Z^0/\gamma^* \rightarrow \tau^+\tau^-$ decay the chosen cut values are at (0.06, 0.06) for muons and at (0.1, 0.06) for electrons. These values are highlighted as a black cross.

is more dependend on the amount of pile-up⁶ in the event for a cone of $\Delta R = 0.4$ than for $\Delta R = 0.3$. For the variable $E_T^{0.3}/E_{Te}$ the sensitivity to the number of pile-up vertices in the event is within its statistical uncertainty. Since the isolation criteria should be as independent as possible of the amount of pile-up, the optimum cut for electrons is

$$E_T^{0.3}/E_{Te} < 0.055 \text{ and } p_T^{0.4}/p_{Te} < 0.045.$$

⁶With pile-up multiple proton-proton interactions per bunch crossing are denoted (section 4.3).

Table 5.3: Summary of the optimal cut values for the isolation variables at different cone sizes, ΔR , for electrons and muons. The optimal cut value is derived by maximising the figure of merit, $\Sigma = s/\sqrt{s+b}$. Furthermore, the chosen cut values are given separately with its dedicated Σ .

ΔR	Electrons			Muons		
	$E_T^{\Delta R}/E_{Te}$	$p_T^{\Delta R}/p_{Te}$	Σ	$E_T^{\Delta R}/p_{T\mu}$	$p_T^{\Delta R}/p_{T\mu}$	Σ
0.2	0.045	0.005	3.38	0.005	0.055	4.49
0.3	0.085	0.005	3.61	0.035	0.065	5.45
0.4	0.105	0.005	3.65	0.055	0.085	6.11
	$E_T^{0.3}/E_{Te}$	$p_T^{0.4}/p_{Te}$	Σ	$E_T^{0.4}/p_{T\mu}$	$p_T^{0.4}/p_{T\mu}$	Σ
	0.1	0.06	3.56	0.06	0.06	6.08

Considering, that the results of this analysis will be combined with that of the semi leptonic decay [55], and the resulting measured cross section will be compared to results from the $Z^0/\gamma^* \rightarrow e^+e^-$ and $Z^0/\gamma^* \rightarrow \mu^+\mu^-$ analysis ([85] and section 5.12), the cut on the isolation variables is chosen to agree with the cuts used in those analyses. Consequently, for this study the cut on the isolation variables for muons is chosen to be:

$$E_T^{0.4}/p_{T\mu} < 0.06 \text{ and } p_T^{0.4}/p_{T\mu} < 0.06 ,$$

whereas for electrons it is:

$$E_T^{0.3}/E_{Te} < 0.10 \text{ and } p_T^{0.4}/p_{Te} < 0.06 .$$

Figure 5.6 and table 5.3 confirm that this approach is justified, since the figure of merit, Σ , shows a plateau in the chosen region and does not vary much around the established maximum. The distribution of the isolation variables themselves is illustrated in figure 5.7. The amount of QCD multijet events is estimated from data (section 5.8.1). Its shape is taken from the control region where both leptons have identical electric charge independent of their isolation. The normalisation is done with the scaling factor $R^{OS/SS}$, which is the ratio of opposite to same sign events. This ansatz is justified since the ratio is independent of the isolation. This assumption is discussed in section 5.10, the uncertainty estimation of the method for the QCD multijet estimation.

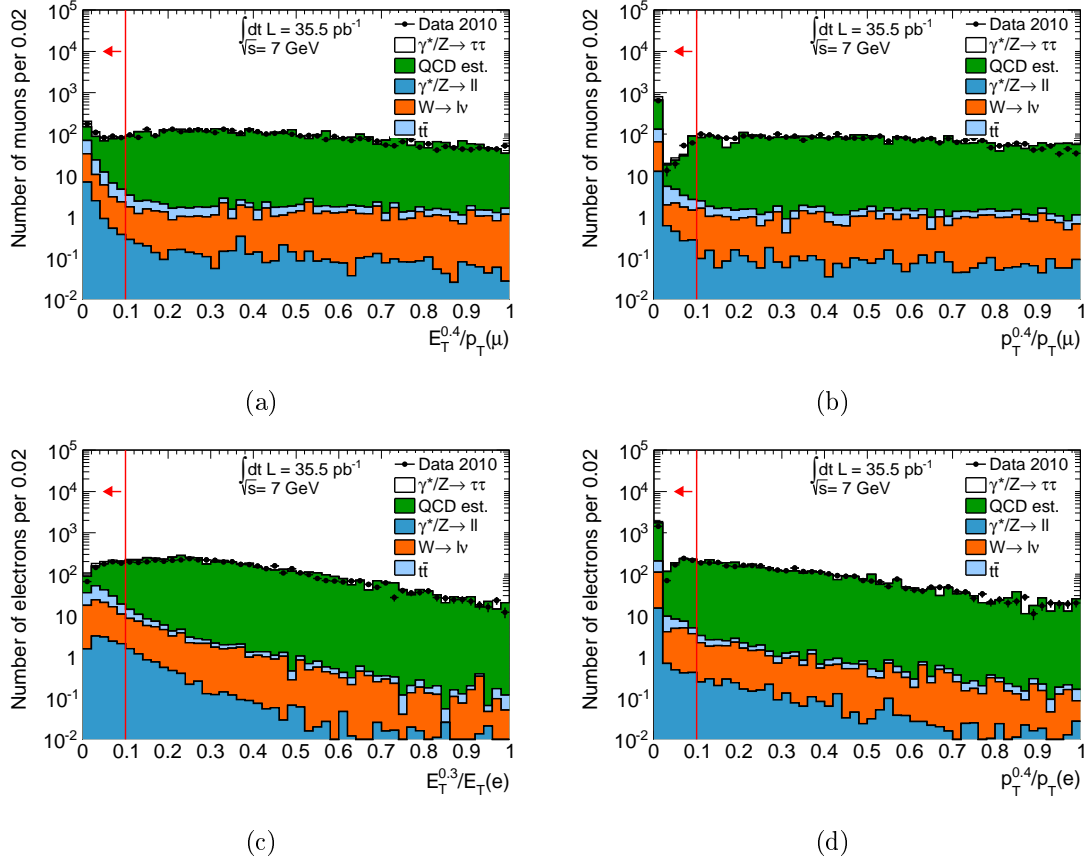


Figure 5.7: Illustration of the isolation variables for muons, (a) and (b), and electrons, (c) and (d) (compare reference [56], figure 5.2 (a) to (d)). The red line marks the cut value, while the arrow indicates the accepted region. The amount of QCD multijet events is estimated from data (section 5.8.1). Its shape is taken from the control region where both leptons have identical electric charge. The normalisation is done with the scaling factor $R^{OS/SS}$.

5.6.7 Monte Carlo corrections

For the measurement of the $Z^0/\gamma^* \rightarrow \tau^+\tau^- \rightarrow e\mu + 4\nu$ cross section, Monte Carlo simulated samples are used. Separate studies have shown that the simulated samples do not represent recorded experimental data as expected, but need to be corrected. In particular, these corrections contain the categories of vertex multiplicity, trigger efficiency, lepton isolation and lepton reconstruction and identification efficiency. To correct for the differences, scaling factors are obtained from the comparison of selected data and simulated samples. The factors are used as weights, C_{scale} , in each event. For the case of the electron-muon final state of the $Z^0/\gamma^* \rightarrow \tau^+\tau^-$ decay the weight would be the following:

$$C_{scale} = C_{Vertex} \cdot C_{Trigger} \\ \cdot (C_{e,reco} \cdot C_{e,id} \cdot C_{e,iso}) \\ \cdot (C_{\mu,reco} \cdot C_{\mu,iso})$$

Most of the scaling factors mentioned above are obtained by tag-and-probe methods. For this, one particular object or event property is tagged and “triggers” the selection. A different object of the event then serves as a probe and its characteristics can be measured independently and in an unbiased way. The method is applied to both, experimental data and simulated samples. Comparison between them leads to the correction factors for the simulated Monte Carlo samples to account for the difference.

Beyond that, corrections also need to be applied to the lepton momentum resolution to make simulated Monte Carlo samples reflecting the recorded experimental data properly.

Vertex reweighting

Each bunch crossing inside the ATLAS detector leads to more than one proton-proton interaction, consequently resulting in more than one vertex at the proton-proton interaction point. The primary vertex of the event is identified as the vertex with the highest sum of the quadratic transverse track momenta, $\sum p_{T,tracks}^2$. All other reconstructed vertices are either labeled as pile-up or secondary vertices from heavy particle decays. The Monte Carlo samples used in this analysis, are simulated with an average number of additional interactions per bunch crossing. The distribution of the number of vertices is chosen to be Poisson distributed with an expectation value of 2.2 (section 5.2.3).

During data taking the beam conditions changed frequently, leading to a varying amount of pile-up in the events. In data the average number of vertices is slightly smaller than in simulated Monte Carlo samples, but still may reach up to nine vertices per event. Therefore, simulated Monte Carlo samples need to be adjusted and are reweighted according to the vertex multiplicity distribution. After the selection steps of data quality (section 5.4), vertex multiplicity, trigger and jet cleaning, the vertex multiplicities between recorded experimental data and simulated Monte Carlo

samples are compared. Both distributions are utilised to calculate the weight factors. In detail, the factors are obtained for each data taking period, separately. The bin-by-bin ratio of the normalised distributions of the number of vertices from data and Monte Carlo is calculated, representing the weighting factors. According to the recorded luminosity, the scaling factors are combined percental for all data taking periods and then used as an event weight in the Monte Carlo simulated samples. The factors used for this analysis are listed in table 5.4. Figure 5.8 shows the vertex multiplicities for experimental data and simulated Monte Carlo samples before and after the vertex reweighting.

Table 5.4: Number of reconstructed vertices and corresponding pile-up weighting factors for simulated Monte Carlo samples (compare reference [56], table C.6).

N(vertices)	pile-up weighting factors
1	1.891 ± 0.013
2	1.234 ± 0.006
3	0.861 ± 0.004
4	0.654 ± 0.004
5	0.539 ± 0.004
6	0.465 ± 0.006
7	0.415 ± 0.010
8	0.448 ± 0.021
9	0.407 ± 0.038
≥ 10	0.582 ± 0.106

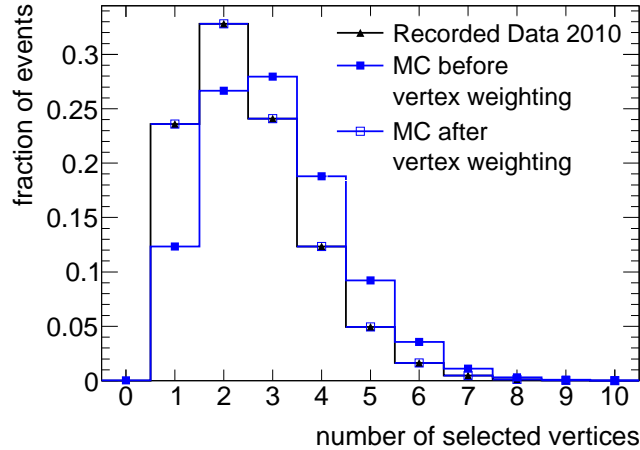


Figure 5.8: Comparison of the vertex multiplicities after the jet cleaning between recorded experimental data from 2010 and simulated Monte Carlo before (filled blue box) and after (open blue box) vertex reweighting.

Trigger efficiency

The present analysis uses the trigger `EF_e15_medium` for selecting events. Its efficiency is determined with the tag-and-probe and the fact that other trigger signatures are uncorrelated [43]. For the tag-and-probe method the $Z^0/\gamma^* \rightarrow e^+e^-$ process is used. One electron of the decay triggers the read-out of the event, while the efficiency of the trigger is measured using the second one as a probe. To confirm the measurement, the efficiency was also analysed using $W^\pm \rightarrow e^\pm\nu_e$ events with an independent missing transverse energy trigger with thresholds between 20 and 40 GeV. The efficiency of the electron trigger is then gained using the offline reconstructed electron as a probe. Exemplarily, figure 5.9 shows the efficiency of the `EF_e15_medium` trigger measured with respect to offline reconstructed electrons passing the `Tight` identification in $W^\pm \rightarrow e^\pm\nu_e$ and $Z^0/\gamma^* \rightarrow e^+e^-$ events. The measured efficiencies for electrons passing the `Medium` identification is similar. Both methods indicate that the plateau of the turn-on curve is reached at about $E_T \approx 20$ GeV and give a cumulative efficiency of $\geq 99\%$. The trigger efficiency for lower energetic electrons was derived in a separate study [55] using a high statistic sample of W bosons decaying to electrons and neutrinos. The trigger efficiency is determined with the uncorrelated missing energy trigger signature.

Trigger efficiencies are derived for experimental data and for simulated Monte Carlo samples, separately. To correct for differences between them, scaling factors are formed from the ratio of experimental data and Monte Carlo samples. They are applied to the simulated Monte Carlo samples. In Table 5.5 the obtained efficiencies and corresponding scaling factors are listed for offline reconstructed `Medium` electrons with $16 \text{ GeV} \leq E_T < 18 \text{ GeV}$, $18 \text{ GeV} \leq E_T < 20 \text{ GeV}$ and $E_T > 20 \text{ GeV}$.

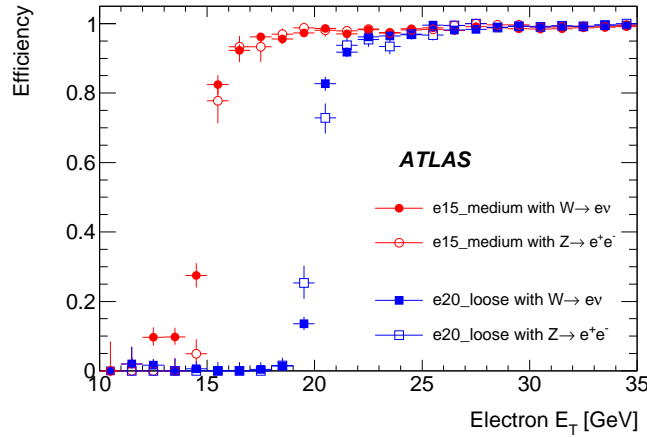


Figure 5.9: Exemplary distribution of the efficiency of the event filter trigger `EF_e15_medium` measured with respect to offline reconstructed `Tight` electrons using $W^\pm \rightarrow e^\pm\nu_e$ and $Z^0/\gamma^* \rightarrow e^+e^-$ events with ATLAS 2010 data [43]. The measured efficiency for `Medium` identified electrons is similar.

Table 5.5: Trigger efficiencies for the event filter trigger `EF_e15_medium` measured with respect to offline reconstructed `Medium` electrons [43]. The corresponding scaling factor is applied to the simulated Monte Carlo samples.

E_T range	Trigger efficiency (%)		scaling factor
	Data	Simulation	
$16 \leq E_T < 18$ GeV	$95.7 \pm 2.4(\text{stat.}) \pm 0.3(\text{syst.})$	$95.3 \pm 0.3(\text{stat.})$	1.004 ± 0.025
$18 \leq E_T < 20$ GeV	$96.3 \pm 2.2(\text{stat.}) \pm 0.4(\text{syst.})$	$97.50 \pm 0.16(\text{stat.})$	0.987 ± 0.023
$E_T > 20$ GeV	$98.97 \pm 0.09(\text{stat.}) \pm 0.09(\text{syst.})$	$99.45 \pm 0.01(\text{stat.})$	0.995 ± 0.005

Electron reconstruction and identification efficiency

The electron reconstruction efficiency was determined using a tag-and-probe method with selected $Z^0/\gamma^* \rightarrow e^+e^-$ decays. It is defined as the probability, that a cluster, selected by sliding window procedure, leads to a reconstructed electron object passing the track quality cuts. The measurement shows, that data and Monte Carlo simulated samples are compatible [81], making a correction factor unnecessary.

Measurements, studying the identification efficiency on the other hand, show a disagreement between observed data and Monte Carlo simulation [81]. The identification efficiency is defined as the probability of a reconstructed electron object being identified with the appropriate cuts. The corresponding scaling factors for Monte Carlo simulated samples are derived by the ratio of the efficiencies from data to Monte Carlo. With tag-and-probe methods on $Z^0/\gamma^* \rightarrow e^+e^-$, $W^\pm \rightarrow e^\pm\nu_e$ and $J/\psi \rightarrow e^+e^-$ decays the identification efficiency with respect to reconstructed electrons of the class `Medium` was obtained. The measurements were carried out separately as a function of η and E_T , leading to correction factors in 8 η bins for the central region $|\eta| < 2.47$ and 6 E_T bins in the range $E_T = 4 - 50$ GeV. Whereas the observed deviation between experimental data and simulated Monte Carlo samples for the η dependence is small, it is significant for the E_T dependence. The identification efficiency reaches its plateau only at about $E_T \approx 30$ GeV. The central identification correction factors are obtained through the combination of the studies of the three distinct decays in different E_T regimes and are listed in table A.1 of the appendix. Because of limited statistics, a two-dimensional map of the correction factors is not utilised. Instead, the E_T and η dependent factors are multiplied.

Muon reconstruction efficiency

The scale factors for the muon reconstruction efficiency were investigated using 2010 recorded ATLAS data with an integrated luminosity of $L = 40 \text{ pb}^{-1}$. They are defined as the ratio between the efficiencies from data and simulated Monte Carlo samples. For the determination of the reconstruction efficiencies a tag-and-probe method with selected $Z^0/\gamma^* \rightarrow \mu^+\mu^-$ decays was chosen. The tags are defined as

combined muons (see section 4.5.2), while the probes are defined as tracks measured in the INNER DETECTOR of the ATLAS detector. With this, the efficiency is calculated from probe tracks, which match a reconstructed muon, and the total number of selected probe tracks. If both, the reconstructed muon and the probe track, have the same measured charge and a small distance to each other in the $\eta - \phi$ plane ($\Delta R \leq 0.01$), they are considered to be matched successfully. The study [86] reveals that the reconstruction efficiency varies from 90% to 99%, as predicted by Monte Carlo simulated samples. It shows a small dependence on the transverse momentum of the muon, but a large dependence on the part of the MUON SPECTROMETER the muon is measured with. The lowest efficiency is observed in the transition region at $\eta \approx 0$. This drop of the efficiency can be explained by the limited accuracy of the magnetic field map, being used in the reconstruction of experimental data. This fact leads to small mismeasurements of the stand-alone muon momentum. The derived scale factors are on average 0.98 ± 0.01 , with the largest deviation of 0.93 ± 0.01 in the transition region. Their dependency in bins of the muon momentum agree within 1.5 standard deviations with the average scale factors and, therefore, were not taken into account for the correction of Monte Carlo predictions. Instead, only different detector regions were regarded when applying the scaling factors. At this point of the ATLAS data taking this approach was suggested by the Muon Combined Performance group.

Isolation efficiencies

The efficiency of an identified lepton to pass the isolation criteria (section 5.6.6) is evaluated using experimental data and simulated Monte Carlo samples. Similar to the aforementioned, correction factors were derived [55]. They are used as a weight for each lepton instead for each event.

Muons

With the help of a tag-and-probe method pairs of $Z^0/\gamma^* \rightarrow \mu^+\mu^-$ decays were identified to determine the efficiency of the track and the calorimeter isolation. The selection of the tag muon is chosen to be very close to the muon selection of this analysis (section 5.5). The isolation efficiency was found to be dependent on the transverse momentum. This dependency is reproduced in simulated Monte Carlo samples very well. The efficiency is independent of η , showing a good agreement between data and Monte Carlo, likewise. Therefore, the isolation correction factors for muons are close to 1.

Electrons

The correction for the isolation efficiency of electrons was evaluated similarly to the approach for muons. First, $Z^0/\gamma^* \rightarrow e^+e^-$ pairs were identified with a tag-and-probe method. The tag electron had to fulfil the same object selection used in this study (section 5.5), except for the isolation, and with a harder cut on the transverse momentum of $p_T > 20$ GeV. The cut on the transverse

momentum ensures a further suppression of electrons from heavy flavour decays of the QCD multijet background. The isolation efficiency was determined in bins of p_T and η , revealing that the efficiency of the Monte Carlo samples is higher than in experimental recorded data. The ratio between data and Monte Carlo samples is dependent on both, p_T and η . Because of a lack of statistics, the correction factors were determined independently as a function of η and p_T . Here, the p_T correction was normalised to the average isolation correction factor.

Electron energy resolution

After applying the appropriate electron energy scale correction to experimental data (section 5.6.5), simulated samples do not reproduce the $Z^0/\gamma^* \rightarrow e^+e^-$ mass distribution properly. Therefore, the electron energy resolution needs to be corrected for in Monte Carlo samples. The fractional electron energy resolution consists of three distinct terms and can be parametrised as a function of the energy as follows:

$$\frac{\sigma_E}{E} = \frac{a}{\sqrt{E/\text{GeV}}} \oplus \frac{b}{E} \oplus c.$$

The parameter a refers to the stochastic term, b the noise term and c is a constant term. All three are η dependent. Considering the insufficient statistics in 2010 data, only the constant term was derived from recorded experimental data with selected $Z^0/\gamma^* \rightarrow e^+e^-$ events [81]. The stochastic and the noise term were taken from Monte Carlo simulation. This approach can be legitimated as the noise term has a contribution at low energies, only. On the other hand, comparison between data and Monte Carlo simulation of selected $J/\psi \rightarrow e^+e^-$ events show a reasonable agreement. For the low energy regime of this decay the electron energy resolution is dominated by the stochastic term. This justifies to take both, the noise and the stochastic term from Monte Carlo simulation. The determination of the constant term of the fractional electron energy resolution was achieved with fits to the invariant mass distribution of $Z^0/\gamma^* \rightarrow e^+e^-$ decays. The fit was implemented using a Breit-Wigner function convoluted with a Crystal Ball function in the mass range 80 – 100 GeV.

Subsequently, the modification of the electron energy resolution needs to be propagated to the value of the missing transverse energy, E_T^{miss} . This is accomplished under the requirement that the sum of unshifted values equals the sum of modified values:

$$\vec{p}_{T,e} + \vec{p}_{T,\mu} + E_T^{\text{miss}} = \vec{p}'_{T,e} + \vec{p}'_{T,\mu} + E_T^{\text{miss}'} . \quad (5.6)$$

Muon momentum resolution

In analogy to the electron energy resolution, the muon momentum resolution needs to be corrected in the simulated Monte Carlo samples. Correction factors are obtained by the comparison of experimental data and simulation. The muon momentum resolution is evaluated for the two detector parts responsible for the recon-

struction of the class of combined muons (section 4.5.2), the INNER DETECTOR and the MUON SPECTROMETER. For a given η value, the fractional muon momentum resolution of the MUON SPECTROMETER can be parametrised as a function of the transverse momentum as follows:

$$\frac{\sigma_p}{p} = \frac{p_0^{MS}}{p_T} \oplus p_1^{MS} \oplus p_2^{MS} \cdot p_T. \quad (5.7)$$

The coefficients p_0^{MS} , p_1^{MS} and p_2^{MS} refer to the energy loss in the calorimeter systems, multiple scattering and intrinsic resolution terms, respectively. A similar parametrisation can be given for the INNER DETECTOR. Within this detector part the muon momentum resolution shows a uniform response in the central part, yet rapidly deteriorating at $|\eta| > 1.9$ because of the limited volume of the TRT (section 4.2.2). The resolution is measured separately for four different η regions, corresponding to the geometrical acceptance of the detector segments within the INNER DETECTOR and the MUON SPECTROMETER, namely: $\eta \in [0, 1.05]$, $[1.05, 1.7]$, $[1.7, 2.0]$, $[2.0, 2.5]$. Although the resolution varies also along ϕ in the MUON SPECTROMETER, this fact is neglected considering the limited available statistics of experimental data. For the correction of the momentum resolution the two processes $Z^0/\gamma^* \rightarrow \mu^+\mu^-$ and $W^\pm \rightarrow \mu^\pm\nu_\mu$ were evaluated [87]. The data used was collected in 2010 by the ATLAS detector, corresponding to an integrated luminosity of $L = 40 \text{ pb}^{-1}$. With the $Z^0/\gamma^* \rightarrow \mu^+\mu^-$ process the width of the reconstructed di-muon invariant mass peak is measured, which is a convolution of the muon momentum resolution and the natural width of the Z^0 boson. In contrast, $W^\pm \rightarrow \mu^\pm\nu_\mu$ gives access to the difference of the independent momentum measurements of the INNER DETECTOR and the MUON SPECTROMETER, being sensitive to the quadratic sum of the separate detector resolutions. The two methods are combined, leading to the final resolution parameters from equation (5.7) and the corresponding formula of the INNER DETECTOR. From this, correction parameters are provided for the simulated muon momentum to reproduce experimental data.

Subsequently, the correction of the muon momentum resolution needs to be transferred to the value of the missing transverse energy. In analogy to the electrons, this is achieved with requirement (5.6).

5.6.8 Rejection of W + jets events

As described in section 5.2.2, events from W + jets decays represent one of the physical background processes. They mimic the signal with one lepton from the W decay, the other lepton through at least one additional jet being misidentified as a lepton candidate and existing missing transverse energy from the neutrino. The probability for jets to be reconstructed as electrons is considerably higher than that for muons, making the $W^\pm \rightarrow \mu^\pm\nu_\mu$ + jets decay more important for the mixed leptonic decay of $Z^0/\gamma^* \rightarrow \tau^+\tau^- \rightarrow \ell^+\ell^- + 4\nu$. To suppress this background, the direction of the missing transverse momentum with respect to the opening angle of

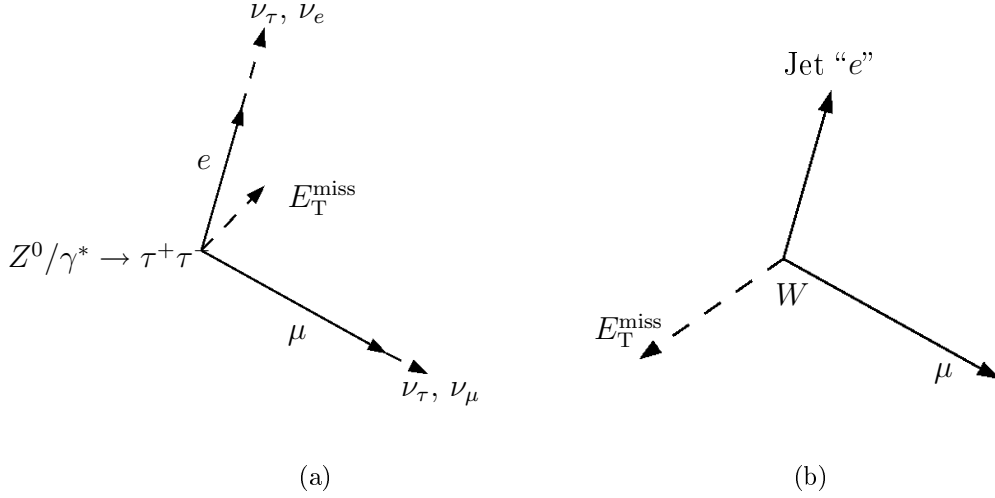


Figure 5.10: Difference of the event topology for (a) $Z^0/\gamma^* \rightarrow \tau^+\tau^-$ and (b) W decays concerning the direction of the E_T^{miss} vector with respect to the opening angle of the two identified lepton candidates.

the two leptons in the transverse plane is used.

With the mass of the Z^0 boson being clearly larger than the τ lepton mass, the τ leptons from the Z^0 decay are highly boosted. This implies that their decay products are collinear, meaning that the light leptons are emitted with the corresponding neutrinos approximately along the direction of flight of the τ lepton. Furthermore, Z^0 bosons are predominantly produced with a low transverse momentum, p_T . Consequently, the decay components are produced back-to-back in the transverse plane. The resulting missing transverse momentum is approximately zero. If the p_T of the Z^0 boson is considerably larger, the direction of the arising E_T^{miss} lies within the opening angle of the visible τ decay products in the transverse plane (figure 5.10). Concerning the W background one of the reconstructed leptons stems from an additional jet in the event. The momenta of the leptons and the neutrino should be balanced in the transverse plane. As the missing transverse momentum is dominated by the neutrino, the direction of the E_T^{miss} points outside the opening angle of the low mass lepton and the misidentified jet. This characteristic is employed in the following formula, designing a variable to suppress events from $W + \text{jets}$ decays.

$$\sum \cos(\Delta\phi) = \cos(\phi(e) - \phi(E_T^{\text{miss}})) + \cos(\phi(\mu) - \phi(E_T^{\text{miss}})) .$$

The difference in the event topology considering the direction of the E_T^{miss} vector with respect to the opening angle of the two identified lepton candidates is depicted in figure 5.10. Illustrated is the W decay to light leptons like electrons and muons. For the W decay to τ leptons, though, the situation does not change. The direction of the E_T^{miss} vector changes slightly with the additional τ neutrino being one of the

decay products, but does not move inside the opening angle of the lepton candidates. The variable $\sum \cos(\Delta\phi)$ yields positive values if the vector of the missing transverse energy lies within the plane spanned by the two lepton vectors. Negative values are obtained when it lies outside. To enrich the data ensemble with $Z^0/\gamma^* \rightarrow \tau^+\tau^-$ events and suppress $W + \text{jets}$ events the tail with positive values is to be kept and events are selected if they fulfil the condition

$$\sum \cos(\Delta\phi) > -0.15.$$

This variable, $\sum \cos(\Delta\phi)$, yields values around zero if the final state products are back-to-back in the transverse plane. By cutting on a value slightly smaller than zero, events with back-to-back topology are selected, as well.

The variable $\sum \cos(\Delta\phi)$ is robust against mismeasurements of the missing transverse energy. First, the variable uses only the direction of E_T^{miss} which is measured more accurately than the magnitude. Secondly, the direction is susceptible to mismeasurements if the magnitude of E_T^{miss} is small which is the case for events with the final state products being back-to-back. Its distribution for $Z^0/\gamma^* \rightarrow \tau^+\tau^-$ events and the relevant background samples is given in figure 5.11(a) after selecting an isolated lepton pair of opposite electric charge and in figure 5.11(b) after cutting on the variable itself.

5.6.9 Rejection of top-quark pair events

Events from the decay of top anti-top quark pairs need to be suppressed further, as well. They contribute to the ensemble of background samples with either two real leptons in the full leptonic decay or with misidentified leptons from jets in the semi or full hadronic decay (section 5.2.2). The topology of its decay contributes with jets and leptons with high transverse momenta as well as a large missing transverse energy. This characteristic is translated into the following cut variable:

$$\sum E_T + E_T^{\text{miss}} = E_{T_e} + E_{T_\mu} + E_{T_{\text{jets}}} + E_T^{\text{miss}}$$

The candidates have to pass the object selection described in section 5.5 and the lepton isolation of section 5.6.6. The distribution is given in figure 5.11(c) for events with an isolated lepton pair of opposite electric charge and in figure 5.11(d) before cutting on the variable itself. Events are kept if they satisfy $\sum E_T + E_T^{\text{miss}} < 150 \text{ GeV}$.

5.6.10 Visible mass window

The final cut in this analysis considers the invariant mass of the selected lepton pair from the τ decays. For its calculation the lepton four-vectors are used. For the electron this is the energy of the electron cluster and the direction of the electron track. The muon four-vector is built from the transverse momentum and the η -,

ϕ - direction, all variables measured with the INNER DETECTOR and the MUON SPECTROMETER. The visible mass window covers the range

$$25 \text{ GeV} < m_{e\mu} < 80 \text{ GeV}$$

and suppresses mostly QCD multijetevents at low masses and $Z^0 \rightarrow e^+e^-/\mu^+\mu^-$ events at high masses. Its distribution is illustrated in figure 5.11(e) after selecting an isolated lepton pair of opposite electric charge and in figure 5.11(f) before the cut on the visible mass.

5.7 Cut summary

The approach to select events from $Z^0/\gamma^* \rightarrow \tau^+\tau^- \rightarrow e\mu + 4\nu$ decays and to enlarge its ensemble while suppressing the corresponding background events can be separated into cuts concerning data quality criteria and event cleaning, object selection, Monte Carlo and energy scale corrections and background suppression cuts. They are fully explained in the sections 5.4 to 5.6 and summarised in table 5.6. Figures 5.4 and 5.11 display important kinematic variables and appropriate distributions after the selection of an isolated electron-muon pair and after subsequent cuts, respectively.

Table 5.6: Summary of the cuts concerning the data quality, object selection and event selection for the enrichment of the signal process $Z^0/\gamma^* \rightarrow \tau^+\tau^- \rightarrow e\mu + 4\nu$.

Data quality criteria	
GoodRunsList	provided by WZ physics group
Object Selection	
Electrons	$E_T > 16$ GeV, $ \eta < 2.47$, $1.37 < \eta < 1.52$ identified with class Medium standard or soft reconstruction algorithm restriction to calorimeter regions without detector problems
Muons	$p_T > 10$ GeV, $ \eta < 2.4$ combined INNER DETECTOR and MUON SPECTROMETER track $ z_0 < 10$ mm pass quality criteria on INNER DETECTOR tracks
Jets	anti- k_t algorithm with distance parameter $\Delta R = 0.4$ $p_T > 20$ GeV, $ \eta < 4.5$
Missing transverse energy	$\vec{E}_T^{\text{miss}} = \vec{E}_T^{\text{miss}}(\text{calo}) + \vec{E}_T^{\text{miss}}(\mu) - \vec{E}_T^{\text{miss}}(\mu \text{ calo})$
Overlap ambiguity	$\mu - \mu$: $\Delta R = 0.2$ $e - e, \mu$: $\Delta R = 0.2$ jet- e, μ, jet : $\Delta R = 0.4$
Event Selection	
Trigger	identified electrons of the class Medium with $p_T > 15$ GeV
Vertex	$n_{vtx} \geq 1$ with $n_{trk} \geq 3$
Jet cleaning	
Lepton pair	$N_e = 1$ and $N_\mu = 1$ $q_e \cdot q_\mu = -1$
Isolation	electron: $E_T^{0.3}/E_{Te} < 0.10$ and $p_T^{0.4}/p_{Te} < 0.06$ muon: $E_T^{0.4}/p_{T\mu} < 0.06$ and $p_T^{0.4}/p_{T\mu} < 0.06$
Electron energy scale correction	
Monte Carlo corrections	
W + jets rejection	$\sum \cos \Delta\phi > -0.15$
$t\bar{t}$ rejection	$\sum E_T + E_T^{\text{miss}} < 150$ GeV
Invariant lepton mass	$25 \text{ GeV} < m_{e\mu} < 80 \text{ GeV}$

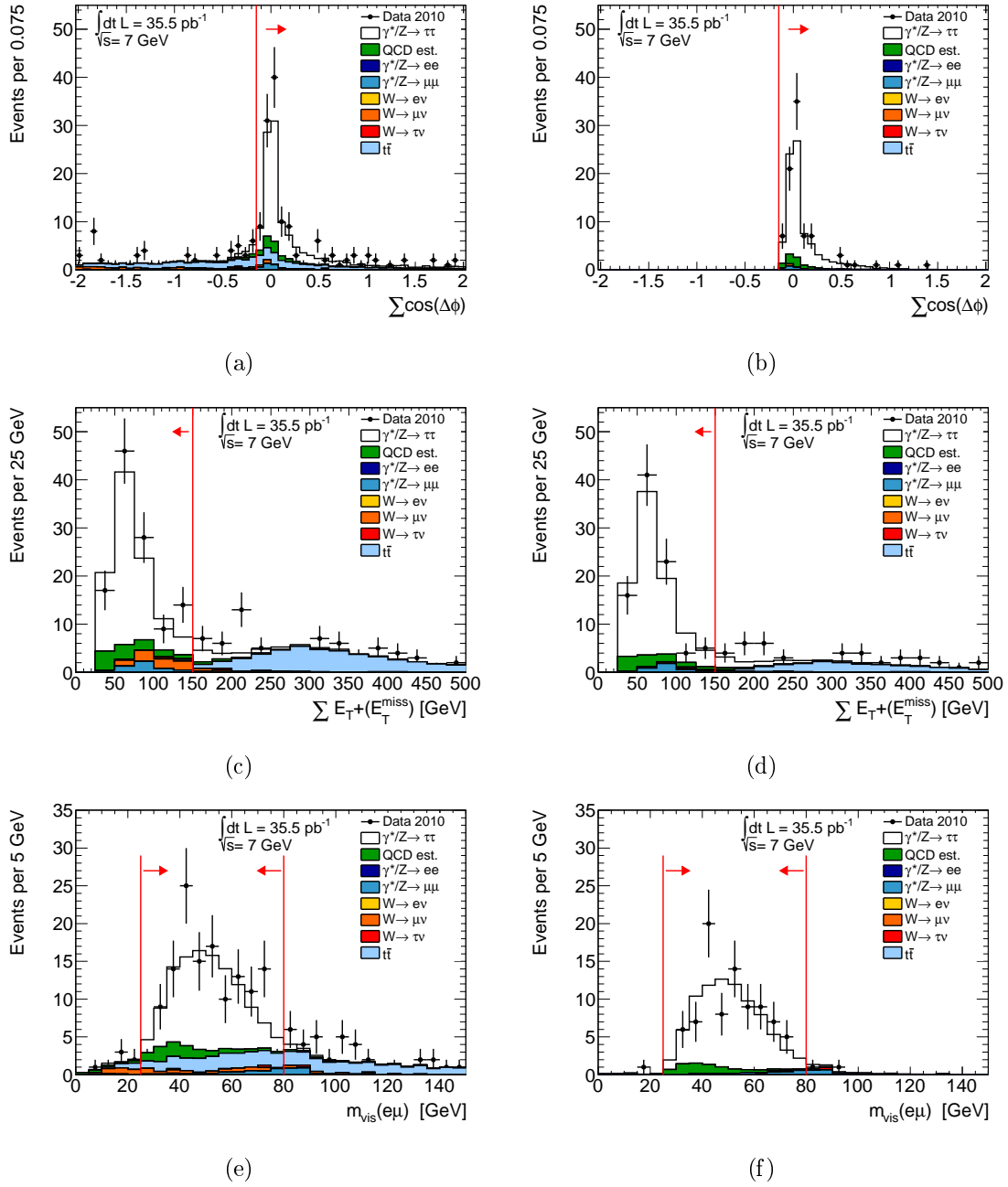


Figure 5.11: Illustration of variables used for the background suppression after the selection of an isolated electron-muon pair of opposite electric charge (left column) and before cutting on the variable itself (right column, except for the variable $\sum \cos(\Delta\phi)$ which is presented after cutting on it, compare [56], figure 5.4 (e),(f), figure 5.5 and [55], figure 6, 7). Represented are selected events of recorded data from 2010, the signal process $Z^0/\gamma^* \rightarrow \tau^+\tau^-$ and its corresponding background samples. The red line marks the cut value, while the arrow indicates the accepted region. The amount of QCD multijet events is estimated from data as described in section 5.8.1.

5.8 Estimation of background processes from data

As already stated in section 5.2.2, background processes for the signal $Z^0/\gamma^* \rightarrow \tau^+\tau^-$ are electroweak processes from the production and subsequent decay of W and Z^0 bosons and $t\bar{t}$ decays. For the specific process of $Z^0/\gamma^* \rightarrow \tau^+\tau^- \rightarrow e\mu + 4\nu$ the decay $W^\pm \rightarrow \mu^\pm\nu_\mu + \text{Jets}$ is dominant among the electroweak processes, since the probability for jets to fake electrons is higher than that for muons. Besides the backgrounds mentioned, QCD multijet events give the major fraction of background processes.

The following section describes methods, how the amount of background events is estimated from data and how important kinematic variables, the taken cross sections and branching ratios are validated against measured data.

5.8.1 QCD multijet processes

As already noted in section 5.2.2 the amount of QCD multijet events cannot be evaluated using Monte Carlo simulated samples. Though the rate of QCD multijet events being misidentified as an electron-muon pair is relatively low, the cross section of the process is rather high. Considering the integrated luminosity of $L = 35.51 \text{ pb}^{-1}$, the generation of the corresponding Monte Carlo samples and especially the simulation of the ATLAS detector response and the reconstruction of all particle objects is extremely computing time consuming. Further, the dedicated algorithms for the identification and reconstruction of electrons and muons are designed to yield low fake rates. This leaves only a small phase space of the simulated QCD multijet events which needs to be understood and simulated with high precision.

The listed circumstances make it mandatory to estimate the amount of QCD multijet events from data rather than from Monte Carlo simulated samples. For this study, the estimation is accomplished via a matrix method. For this, two variables are selected, spanning a two-dimensional plane, segmented into four regions. The four regions are defined such, that only one region contains a significant amount of $Z^0/\gamma^* \rightarrow \tau^+\tau^-$ events. This region is referred to as the “signal region”, while the others are called “control regions”. The control regions are chosen to contain an amount of signal events as small as possible, but in contrast are dominated by QCD multijet events. Further, the variables defining the regions need to be uncorrelated. For the present analysis, the electric charge product of the leptons and their isolation are the variables chosen for the matrix method. After the selection of an electron-muon pair the four regions are determined as follows:

- **Region A:** isolated lepton pair with opposite electric charge
- **Region B:** isolated lepton pair with same electric charge
- **Region C:** both leptons non-isolated with opposite electric charge
- **Region D:** both leptons non-isolated with same electric charge

	$q_e \times q_\mu$			
OS	<table> <tr> <td>A Signal region</td> <td>C QCD dominated</td> </tr> </table>	A Signal region	C QCD dominated	
A Signal region	C QCD dominated			
SS	<table> <tr> <td>B EW bkg, $t\bar{t}$, QCD</td> <td>D QCD dominated</td> </tr> </table>	B EW bkg, $t\bar{t}$, QCD	D QCD dominated	
B EW bkg, $t\bar{t}$, QCD	D QCD dominated			
	isolated	non-isolated isolation		

Figure 5.12: Matrix for the QCD multijet estimation from measured data. The utilised variables are the charge product of the selected electron-muon pair and their isolation. The charge product is abbreviated with OS (opposite sign) for opposite electric charge and SS (same sign) for same electric charge of the lepton pair. Region A is the signal region, whereas the others are QCD multijet enriched control regions with a small signal amount.

This definition, sketched in figure 5.12, makes Region A the signal region with an isolated electron-muon pair of opposite sign. The number of events from the signal process, its corresponding background processes and the measured data events in the four regions are listed in table 5.7. The charge product and the isolation of the leptons are uncorrelated for QCD multijet events. With this, it can be assumed that the ratio of electron-muon pairs with opposite and same electric charge from multijet events stays unmodified regardless of their isolation:

$$\frac{N_{QCD}^A}{N_{QCD}^B} = \frac{N_{QCD}^C}{N_{QCD}^D}. \quad (5.8)$$

Here, N_{QCD}^i illustrates the number of events from multijet events, only. Comparing the number of Monte Carlo simulated signal and background events in the four regions with the measured data events, as stated in table 5.7, it is evident, that only region C and D are QCD multijet dominated, with a purity of 99.7%. Therefore, the number of QCD multijet events is approximately equal to the number of data events in these regions. In contrast, Region B also contains a significant amount of background events from electroweak processes and $t\bar{t}$ events. The number of QCD multijet events N_{QCD}^i in formula 5.8 is estimated as:

$$N_{QCD}^i = N_{Data}^i - N_{EW_bkg}^i - N_{t\bar{t}}^i,$$

with $N_{EW_bkg}^i = \sum_{\ell} N_{Z^0 \rightarrow e\ell/\mu\mu}^i + \sum_{\ell} N_{W^\pm \rightarrow \ell^\pm \nu_\ell}^i$, ($\ell = e, \mu, \tau$), and for all control regions, i.e. $i = B, C, D$ and . The number of events from the signal process $Z^0/\gamma^* \rightarrow \tau^+\tau^- \rightarrow e\mu + 4\nu$ is not subtracted from the measured data events, explicitly, as its cross section times branching ratio is to be measured. In figure 5.13

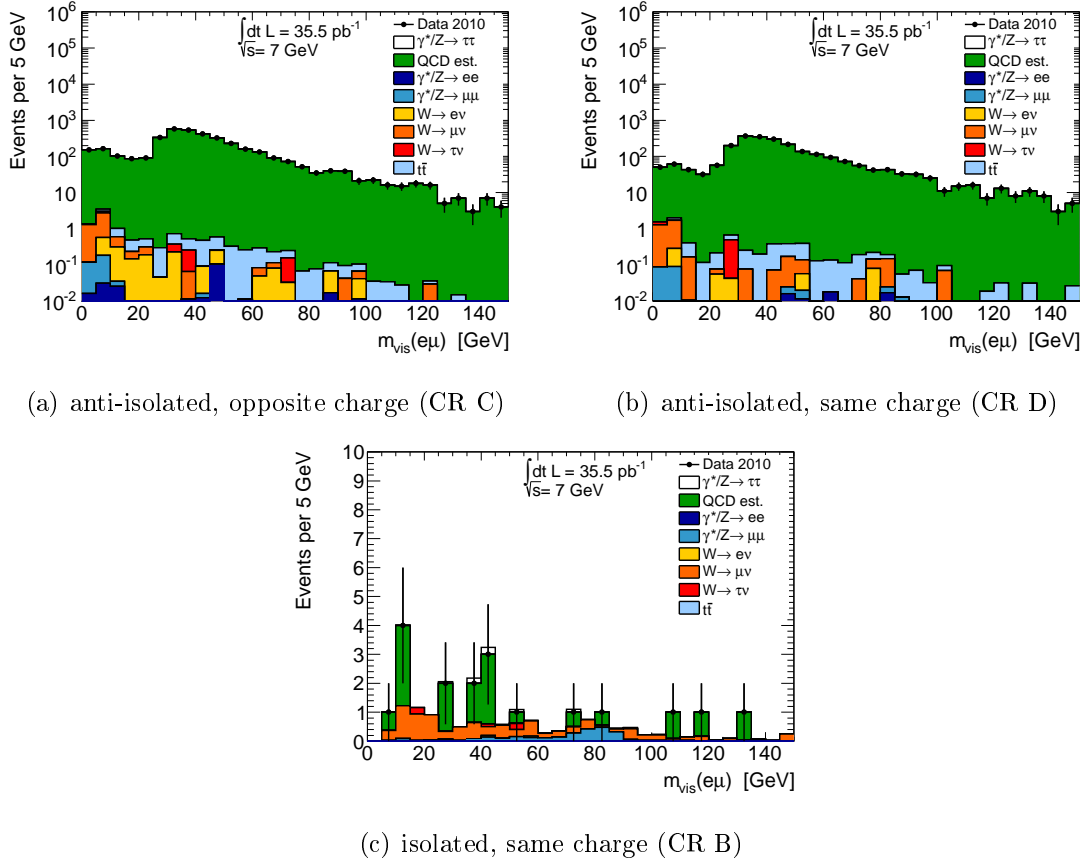


Figure 5.13: Distribution of the visible mass after the selection of a lepton pair in the QCD multijet dominated control regions (CR) C and D (top) and the control region B (bottom).

the distribution of the visible mass is given for the QCD multijet dominated control regions C and D and for the control region B after the selection of a lepton pair. With equation (5.8) the amount of QCD multijet events in the signal region can be estimated through:

$$N_{QCD}^A = N_{QCD}^B \cdot \frac{N_{QCD}^C}{N_{QCD}^D} = N_{QCD}^B \cdot R^{OS/SS}. \quad (5.9)$$

$R^{OS/SS}$ is the ratio of opposite to same sign events in the non-isolated regions. With the numbers of table 5.7 it is calculated to be

$$R^{OS/SS} = \frac{3759}{2423} = 1.55 \pm 0.04(\text{stat.}).$$

Limited data statistics after the full selection, especially in the region with isolated leptons of the same electric charge (region B), make it necessary to estimate the final amount of QCD multijet events earlier in the cut flow instead of the end of the

Table 5.7: Number of events after the lepton pair selection used for the QCD multijet estimation via the matrix method. The uncertainties given are of statistical nature.

Region	Event yield
A: opp. electr. charge, isolated	$N_{Signal} = 86.9 \pm 1.3$
	$N_{EW_bkg+t\bar{t}} = 64.1 \pm 1.0$
	$N_{Data} = 190$
B: same electr. charge, isolated	$N_{Signal} = 1.45 \pm 0.18$
	$N_{EW_bkg+t\bar{t}} = 13.41 \pm 0.79$
	$N_{Data} = 22$
	$N_{QCD} = 8.6 \pm 4.8$
C: opp. electr. charge, anti-isolated	$N_{Signal} = 0.61 \pm 0.10$
	$N_{EW_bkg+t\bar{t}} = 11.61 \pm 0.73$
	$N_{Data} = 3771$
	$N_{QCD} = 3759 \pm 61$
D: same electr. charge, anti-isolated	$N_{Signal} = 0.51 \pm 0.15$
	$N_{EW_bkg+t\bar{t}} = 8.06 \pm 0.62$
	$N_{Data} = 2432$
	$N_{QCD} = 2423 \pm 49$

event selection. The number of QCD multijet events is therefore estimated after the lepton pair selection (see table 5.6) and then propagated to the final selection. The propagation is conducted with the usage of the efficiency of the subsequent cuts. This selection efficiency for QCD multijet events is obtained from the region with non-isolated leptons of the same electric charge (region D). For this, it is assumed that the selection efficiency is uncorrelated with the leptons charge product and their isolation. Further it is mandatory, that the selection efficiency is not influenced by subsequent cuts. In section 5.10 these assumptions are examined more closely. Finally, the selection efficiency is calculated as

$$\epsilon_{QCD} = \frac{N_{QCD}^{D, final}}{N_{QCD}^{D, e\mu pair}} = \frac{1366}{2423} = 0.56 \pm 0.02(\text{stat.}) . \quad (5.10)$$

With the numbers of table 5.7 the amount of QCD multijet events after the final selection is therefore estimated as:

$$\begin{aligned} N_{QCD}^{A, final} &= N_{QCD}^{B, e\mu pair} \cdot R^{OS/SS} \cdot \epsilon_{QCD} \\ &= 7.51 \pm 4.17(\text{stat.}) . \end{aligned}$$

Figure 5.4 and 5.11 display the signal and background Monte Carlo simulated processes in comparison with measured data. The amount of QCD multijet events is estimated from data with the method explained above. The shape of the QCD multijet contribution is obtained from the selected data ensemble of region D,

which has a purity of 99.7%. It is then scaled to the corresponding amount of QCD multijet events in the signal region with the ratio $R^{OS/SS}$ and the appropriate cut efficiency.

For the isolation distributions in figure 5.7 the shape and amount of QCD multijet events is obtained after the selection of an electron-muon pair. Regardless of their isolation the pairs are split according to their product of the electric charge. The signal process $Z^0/\gamma^* \rightarrow \tau^+\tau^- \rightarrow e\mu + 4\nu$ occurs in the region of pairs with opposite electric charge. The amount of QCD multijet events in this region is calculated from the same sign region with the ratio $R^{OS/SS}$. This step is possible as the electric charge of the lepton is independent of its isolation. The shape of the QCD multijet events is taken from the same sign region.

The official ATLAS study [55], which examines the same amount of data, has a slightly different ansatz of the QCD multijet estimation from data. Reference [55] subtracts the amount of signal events $Z^0/\gamma^* \rightarrow \tau^+\tau^- \rightarrow e\mu + 4\nu$ in the control region B, which contains an isolated lepton pair of same electrical charge. With this, the cross section of the signal process calculated from theory needs to be deployed. The study at hand however, refrains from this ansatz, since the cross section is the variable to be measured and therefore should not be utilised in the analysis. In reference [56] the estimation of QCD multijet background events differs in the evaluation of QCD multijet events in the control regions. While the study at hand subtracts the amount of background events from electroweak processes and $t\bar{t}$ events for all control regions, reference [56] implements this only for control region B. Consequently, the amount of QCD multijet events in the signal region is 20% less in the official ATLAS study [55] and 8% less in reference [56] compared to this study.

5.8.2 Electroweak processes

For this study, the ensemble of electroweak processes is taken from Monte Carlo simulation. With this, one relies on the correct calculation at matrix element level, the hadronisation, the initial and final state radiation and the full simulation and reconstruction of the detector response. Besides being major backgrounds to the signal $Z^0/\gamma^* \rightarrow \tau^+\tau^-$, electroweak processes also have to be considered in the estimation of the QCD multijet background (section 5.8.1), being subtracted from measured data events. It is therefore important to check whether the normalisation with the cross sections and branching ratios used is correct and corresponds to the number of measured events from electroweak processes. Furthermore, distributions of important kinematic variables are investigated and compared.

For the validation of the $W^\pm \rightarrow e^\pm \nu_e / \mu^\pm \nu_\mu + \text{Jets}$ background a phase space of the collected data ensemble is used in which W decays are enriched but others are suppressed. This is achieved by selecting an electron-muon pair as described for the signal selection in section 5.6.4. For this, the second lepton stems from present jets, with either a real lepton from decaying heavy flavour quarks or a misidentified lepton. The electron-muon pair is asked to have the same electric charge, primarily

to suppress $Z^0/\gamma^* \rightarrow \tau^+\tau^- \rightarrow e\mu + 4\nu$ events. For the enhancement of the specific decay $W^\pm \rightarrow \mu^\pm\nu_\mu$ the muon ought to be isolated as described in section 5.6.6, whereas the electron candidate does not have to pass any isolation criteria. In contrast, for the W boson decaying to an electron and neutrino, the electron has to pass the isolation requirements, whereas the muon has not to. Furthermore, the cut on the sum of the transverse energy from jets and leptons and the missing transverse energy is applied to suppress decays from $t\bar{t}$. The particular cut is set to $\sum E_T + E_T^{\text{miss}} < 150$ GeV. Finally, the analysis makes use of the transverse mass. To enhance W boson decays this variable is built from the transverse momentum of the selected lepton and the missing transverse energy and their angular separation:

$$m_T = \sqrt{2 \cdot p_{T\mu} \cdot E_T^{\text{miss}} \cdot (1 - \cos(\Delta\phi(\vec{\mu}, \vec{E}_T^{\text{miss}})))}.$$

Here, $\vec{\mu}$ and \vec{E}_T^{miss} represent vectors in the three dimensional space. The same variable is built for the $W^\pm \rightarrow e^\pm\nu_e$ decay with the electron contribution. Events require a transverse mass in the range $60 \text{ GeV} < m_T < 100 \text{ GeV}$ to pass the cut. Just as for the selection of the signal $Z^0/\gamma^* \rightarrow \tau^+\tau^- \rightarrow e\mu + 4\nu$ the contribution from QCD multijet events needs to be estimated for the validation of the W decay background. Likewise, the matrix method is employed (section 5.8.1). The method uses two uncorrelated variables with two distinct regions, resulting in one signal enriched region and three control regions dominated by background processes. For the QCD multijet estimation of this section the term “signal” refers to the decay of W bosons. The two variables used are the charge product of the selected lepton pair and their isolation. The phase space of *isolation* is divided into one region where both leptons show non-isolation, i.e. they fail the isolation cuts of section 5.6.6. The other region depends on the specific decay of the W boson. For $W^\pm \rightarrow \mu^\pm\nu_\mu$ the selected muon ought to be isolated, while there is no particular requirement on the electron isolation. For the $W^\pm \rightarrow e^\pm\nu_e$ decay the specification is reversed; the electron shows isolation, while there is no isolation requirement for the muon. The matrix for the QCD multijet estimation in the W decay enriched region is depicted in figure 5.14.

Based on the procedure of QCD multijet estimation from data described in section 5.8.1 the number of QCD multijet events is calculated as

$$N_{QCD}^A = N_{QCD}^B \cdot \frac{N_{QCD}^C}{N_{QCD}^D}.$$

The variable N_{QCD}^i , with $i = B, C, D$, is the number of selected data events with the electroweak samples being subtracted including the processes $Z^0/\gamma^* \rightarrow \tau^+\tau^-$ and $t\bar{t}$. In the control region which is not dominated by QCD multijet events, the share of W decays is approximately 10% out of selected data events. As the normalisation and the shape of important distributions are ought to be checked only, it is considered to subtract the number of events from W decays, as well. After the full selection of the W enriched region, the number of selected data events show sufficient statistics, that the amount of QCD multijet events can be calculated

	$q_e \times q_\mu$			
OS	<table> <tr> <td>A Signal region</td> <td>C QCD dominated</td> </tr> </table>	A Signal region	C QCD dominated	
A Signal region	C QCD dominated			
SS	<table> <tr> <td>B EW bkg, $t\bar{t}$, QCD</td> <td>D QCD dominated</td> </tr> </table>	B EW bkg, $t\bar{t}$, QCD	D QCD dominated	
B EW bkg, $t\bar{t}$, QCD	D QCD dominated			
	isolated e/μ	non-isolated isolation		

Figure 5.14: Matrix for the QCD multijet estimation from measured data for the validation of the Monte Carlo simulated samples of the W decay to leptons. The variables used are the charge product of the selected electron-muon pair and their isolation. The charge product is abbreviated with OS (opposite sign) for opposite electric charge and SS (same sign) for same electric charge of the lepton pair. Region A is the signal region for the W decays, whereas the others are QCD multijet enriched control regions.

directly and the utilisation of a cut efficiency is unnecessary.

In the selected phase space, the signal region A, the decay $W^\pm \rightarrow e^\pm \nu_e$ shows a fraction of 18%, the decay $W^\pm \rightarrow \mu^\pm \nu_\mu$ dominates with 60%. The normalisation with measured data events is validated with the results listed in table 5.8 and 5.9. Further, the distribution of representative kinematic variables for the W decay is illustrated in figures 5.15 and 5.16. The shape of the QCD multijet contribution is taken from measured data from the control region D. This region is characterised by the presence of an electron and a muon, both are not isolated and show opposite charge. Region D is dominated by QCD multijet events with 94% for both W decay channels. The distributions in figures 5.15 and 5.16 show an appropriate agreement between data and simulated Monte Carlo samples; tables 5.8 and 5.9 indicate an appropriate normalisation. As a whole, they show that the cross sections and branching ratios are well agreeing with data. On the other hand, it also proves the correctness of the Monte Carlo simulation showing that any kind of scaling factors are unnecessary.

5.8.3 Background from top-quark pairs

Similarly to the validation of the W decay, important kinematic variables and the normalisation of the $t\bar{t}$ process are studied. Likewise, the process presents an important background to the signal $Z^0/\gamma^* \rightarrow \tau^+\tau^- \rightarrow e\mu + 4\nu$ and is subtracted from measured data events in the procedure of the QCD multijet background estimation. To enrich an ensemble with decays from a top anti-top quark pair events are selected comprising a pair of an electron and a muon passing the requirements

Table 5.8: Number of selected events in the $W^\pm \rightarrow \mu^\pm \nu_\mu$ control region from data and Monte Carlo simulation. The amount of QCD multijet events is estimated from data via the matrix method making use of the isolation of the chosen lepton pair and their charge product. The presented numbers are after the cut on the sum of the transverse energy from jets and leptons and the missing transverse energy and the transverse mass, respectively (compare [56] table 5.4). The uncertainties given are of statistical nature, only.

	$N_{\sum E_T + E_T^{\text{miss}} < 150 \text{ GeV}}$	$N_{60 < m_T < 100 \text{ GeV}}$
$Z^0/\gamma^* \rightarrow \tau^+ \tau^-$	4.95 ± 0.34	0.11 ± 0.05
$Z^0/\gamma^* \rightarrow e^+ e^-$	0.06 ± 0.03	0.01 ± 0.01
$Z^0/\gamma^* \rightarrow \mu^+ \mu^-$	7.55 ± 0.31	0.59 ± 0.06
$W^\pm \rightarrow e^\pm \nu_e$	0.11 ± 0.07	0.05 ± 0.05
$W^\pm \rightarrow \tau^\pm \nu_\tau$	2.23 ± 0.64	0.62 ± 0.35
$t\bar{t}$	0.06 ± 0.02	0.02 ± 0.01
QCD est.	48.6 ± 9.9	5.8 ± 4.1
$\sum \text{Bkg} + \text{QCD}$	63.5 ± 9.9	7.3 ± 4.1
$W^\pm \rightarrow \mu^\pm \nu_\mu$	25.3 ± 1.3	10.69 ± 0.78
Data	77	18

Table 5.9: Number of selected events in the $W^\pm \rightarrow e^\pm \nu_e$ control region from data and Monte Carlo simulation. The amount of QCD multijet events is estimated from data via the matrix method making use of the isolation of the chosen lepton pair and their charge product. The numbers presented are after the cut on the sum of the transverse energy from jets and leptons and the missing transverse energy and the transverse mass, respectively (compare [56] table 5.4). The uncertainties given are of statistical nature, only.

	$N_{\sum E_T + E_T^{\text{miss}} < 150 \text{ GeV}}$	$N_{60 < m_T < 100 \text{ GeV}}$
$Z^0/\gamma^* \rightarrow \tau^+ \tau^-$	2.21 ± 0.22	0.18 ± 0.06
$Z^0/\gamma^* \rightarrow e^+ e^-$	3.43 ± 0.28	0.34 ± 0.07
$Z^0/\gamma^* \rightarrow \mu^+ \mu^-$	2.88 ± 0.15	0.10 ± 0.02
$W^\pm \rightarrow \mu^\pm \nu_\mu$	9.15 ± 0.68	2.81 ± 0.39
$W^\pm \rightarrow \tau^\pm \nu_\tau$	1.25 ± 0.53	0.40 ± 0.32
$t\bar{t}$	0.37 ± 0.05	0.12 ± 0.03
QCD est.	167.4 ± 14.1	19.4 ± 7.4
$\sum \text{Bkg} + \text{QCD est.}$	186.7 ± 14.2	23.3 ± 7.5
$W^\pm \rightarrow e^\pm \nu_e$	8.51 ± 0.77	5.24 ± 0.62
Data	232	29

of the $Z^0/\gamma^* \rightarrow \tau^+\tau^- \rightarrow e\mu + 4\nu$ selection (section 5.6.4). The pair ought to have opposite electric charge. Furthermore, the cut on the angular correlation of the lepton and the missing transverse energy is inverted, to be specific the cut becomes $\sum \cos(\Delta\phi) < -0.15$. This suppresses contributions from the signal strongly while keeping most of the $t\bar{t}$ events. To enhance contribution from top anti-top quark pairs further, the cut on the sum of the transverse energy of leptons and jets and missing transverse energy is inverted as well, namely $\sum E_T + E_T^{\text{miss}} > 150$ GeV. The procedure yields a purity of 81% $t\bar{t}$ events.

The amount of QCD multijet background is estimated from data, as well. Again, the matrix method is used with the two variables *charge product* and *isolation* spanning the ABCD plane. The *charge product* is split into the two distinct states of same and opposite sign, whereas the *isolation* is split into the regions of having two isolated leptons or two leptons showing non-isolation (section 5.6.6). Compared to the QCD multijet estimation for the signal process $Z^0/\gamma^* \rightarrow \tau^+\tau^- \rightarrow e\mu + 4\nu$, the matrix is chosen to be the same. The step at which the contribution from QCD multijet events is calculated differs, namely after the inverted cuts on $\sum \cos(\Delta\phi)$ and $\sum E_T + E_T^{\text{miss}}$. Sufficient data statistics make it possible to calculate its number of events in the signal region after the final cut. The number of QCD multijet events in the control regions is estimated by subtracting the amount of electroweak background processes from measured data events. The number of events of the Monte Carlo simulated $t\bar{t}$ sample is not subtracted. The shape of the QCD multijet background is taken from the region with non-isolated leptons with the same electric charge, e.g. region D in figure 5.12.

The result of the test for the normalisation of the $t\bar{t}$ process is stated in table 5.10. The numbers give an appropriate agreement between measured data and the sum of the contributions from the simulated Monte Carlo signal process and the estimated QCD multijet background. Important kinematic variables for the decay of top anti-top quark pairs are displayed in figure 5.17. They present agreement within the uncertainties for the normalisation, as well as for the shape of the variables. As for the cross check of the electroweak background in section 5.8.2 the results approve the cross sections, branching ratios used and the correctness of the Monte Carlo simulated samples. Again, the application of scaling factors is not required.

Table 5.10: Number of selected events in the $t\bar{t}$ control region from data and Monte Carlo simulated samples. The amount of QCD multijet events is estimated from measured data via the matrix method as described in section 5.8.3. The numbers presented are selected after the inverted cuts on $\sum \cos(\Delta\phi)$ and $\sum E_T + E_T^{\text{miss}}$ (compare [56] table 5.5). The uncertainties given are of statistical nature, only.

	N
$Z^0/\gamma^* \rightarrow \tau^+\tau^-$	0.31 ± 0.08
$Z^0/\gamma^* \rightarrow e^+e^-$	0.00 ± 0.00
$Z^0/\gamma^* \rightarrow \mu^+\mu^-$	0.19 ± 0.04
$W^\pm \rightarrow e^\pm\nu_e$	0.08 ± 0.08
$W^\pm \rightarrow \mu^\pm\nu_\mu$	1.29 ± 0.26
$W^\pm \rightarrow \tau^\pm\nu_\tau$	0.33 ± 0.33
QCD est.	2.63 ± 2.81
$\sum \text{Bkg+QCD est.}$	4.83 ± 2.84
$t\bar{t}$	26.98 ± 0.40
Data	31.00

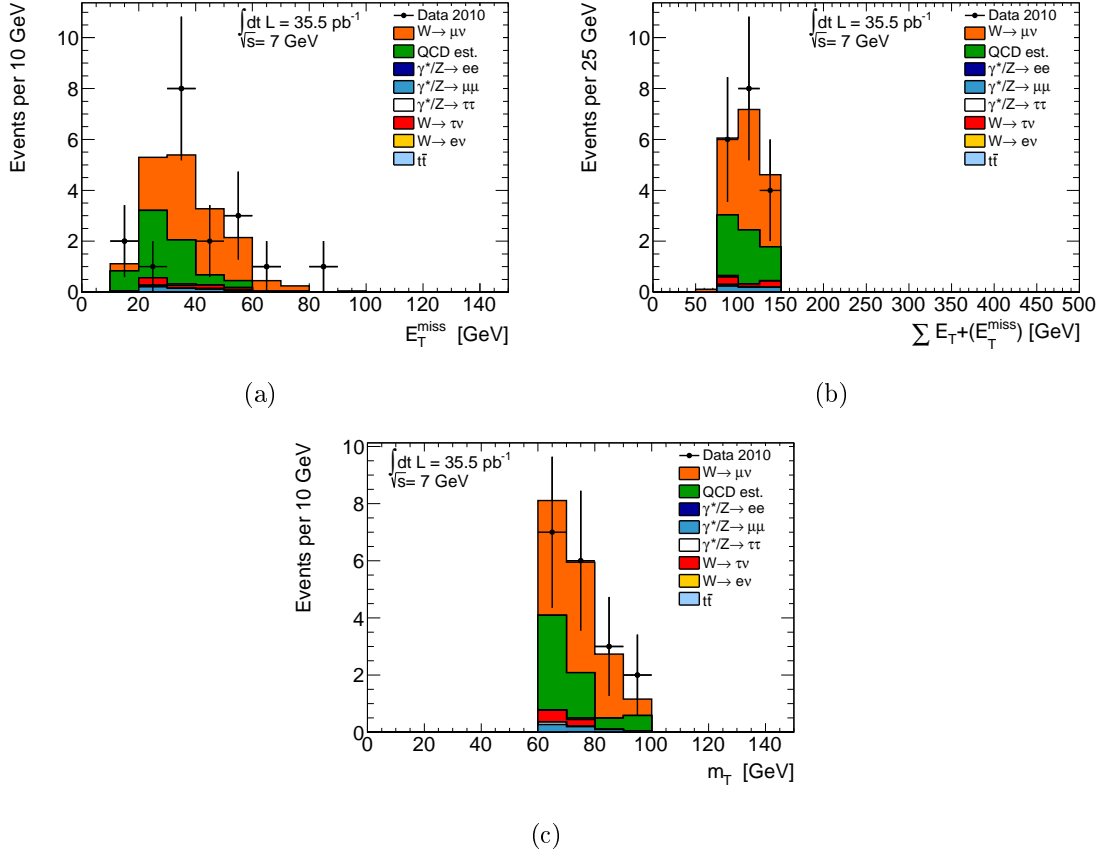


Figure 5.15: Distributions for the cross check of the normalisation of Monte Carlo simulated samples for the process $W^\pm \rightarrow \mu^\pm \nu_\mu$. Represented are the variables of the (a) missing transverse energy, E_T^{miss} , (b) the sum of the transverse energy from jets and leptons and the missing transverse energy and (c) the transverse mass, m_T . The ensembles of data and simulated events are selected with the cuts referring to the $W^\pm \rightarrow \mu^\pm \nu_\mu$ signal region. The amount of events stemming from QCD multijet processes are evaluated with measured data. Its shape refers to measured data events in the control region D with two non isolated leptons of opposite charge.

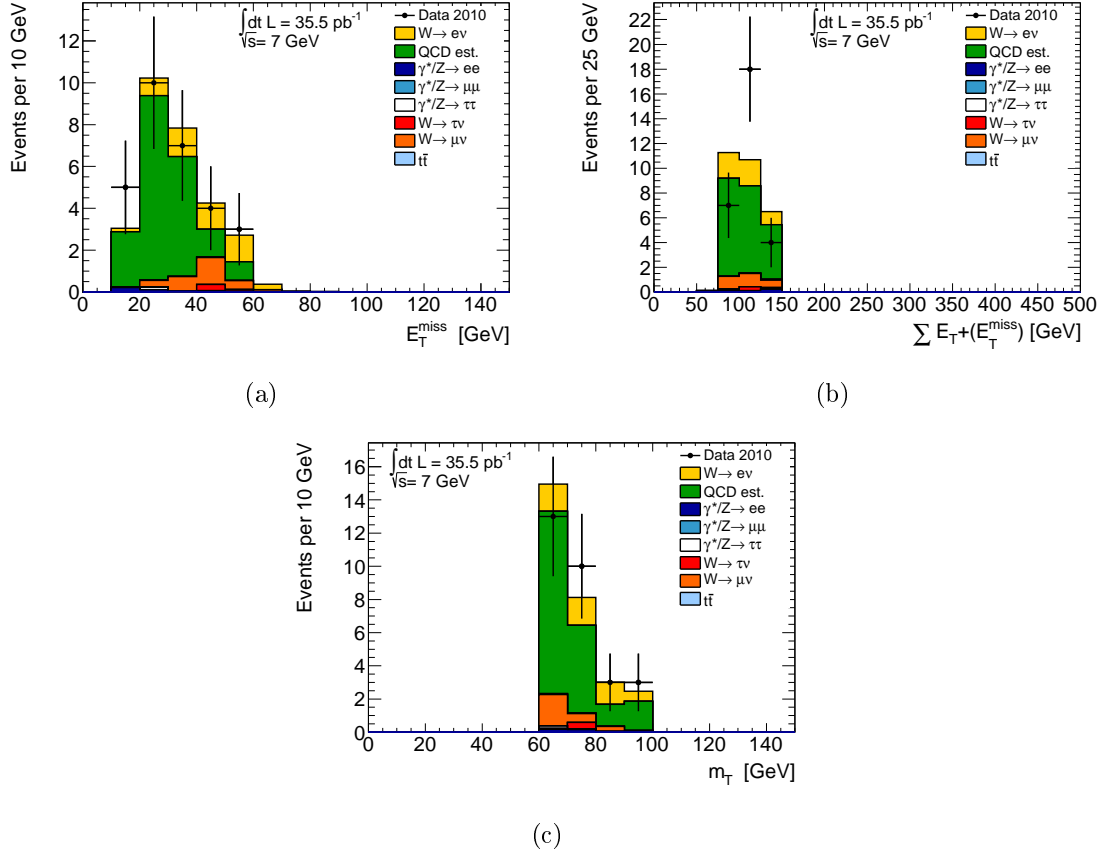


Figure 5.16: Distributions for the cross check of the normalisation of Monte Carlo simulated samples for the process $W^\pm \rightarrow e^\pm \nu_e$. Represented are the variables of the (a) missing transverse energy, E_T^{miss} , (b) the sum of the transverse energy from jets and leptons and the missing transverse energy and (c) the transverse mass, m_T . The ensembles of data and simulated events are selected with the cuts referring to the $W^\pm \rightarrow e^\pm \nu_e$ signal region. The amount of events stemming from QCD multijet processes are evaluated with measured data. Its shape refers to measured data events in the control region D with two non isolated leptons of opposite charge.

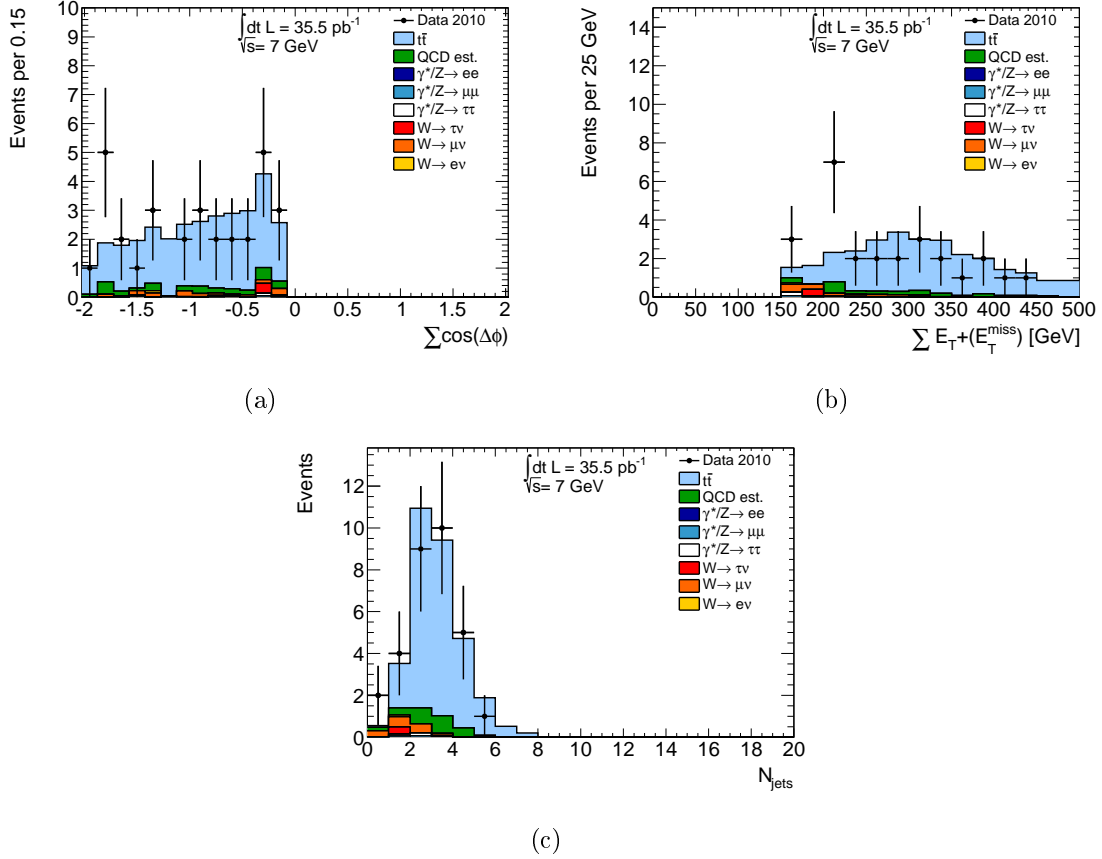


Figure 5.17: Distribution of characteristic variables of the $t\bar{t}$ process after the specific selection of the $t\bar{t}$ signal phase space. Represented are (a) the angular correlation of the lepton and the missing transverse energy, (b) the sum of the transverse energy of leptons and jets and missing transverse energy and (c) the number of present jets in the event. The amount of QCD multijet events is estimated from measured data, its shape is taken from measured data events of the control region D with two non isolated leptons of the same electric charge.

5.9 Determination of the $Z^0/\gamma^* \rightarrow \tau^+\tau^-$ cross section

The cross section of a process is calculated using the number of observed signal events detected with a certain integrated luminosity. The integrated luminosity, L , can be measured directly at the accelerator. In contrast, the number of signal events, N_{Signal} , is evaluated by the observation of events in a certain phase space. For each sought-after process the phase space is determined individually on the basis of its intrinsic characteristics. The number of observed events, N_{obs} , contains background events whose amount needs to be estimated and subtracted. The number of background events, N_{bkg} , can either be determined from Monte Carlo generated samples or from measured data. With this, the cross section, σ , can be derived through:

$$\sigma = \frac{N_{Signal}}{L} = \frac{N_{obs} - N_{bkg}}{L} . \quad (5.11)$$

As mentioned above, the cross section from equation (5.11) is calculated with events selected in a specific phase space. In order to compare the measured cross sections across different experiments and with results from theory, the fully inclusive cross section, σ_{incl} , needs to be determined. This is achieved by correcting the cross section from equation 5.11 with factors accounting for detector efficiencies and the selection of a phase space region :

$$\sigma_{incl} = \sigma \cdot \frac{1}{\epsilon} = \sigma \cdot \frac{1}{A_Z \cdot C_Z} . \quad (5.12)$$

The correction factor, ϵ , can be calculated with Monte Carlo generated samples. It is derived as the ratio of the number of reconstructed and selected events and the number of generated events. The correction factor can be split into two parts, A_Z and C_Z . The first, A_Z , denotes the kinematic and geometric acceptance by describing the probability that the signal process generates a final state within the fiducial phase space. A_Z is therefore also called the acceptance factor. In contrast, C_Z accounts for the efficiency of triggering, reconstructing and identifying signal events in this certain phase space. With N_{gen} being the number of generated events, N_{ps} the number of events within the specific phase space region and N_{sel} the number of events passing the full event selection, ϵ can be calculated using a Monte Carlo generated sample as

$$\epsilon = \frac{N_{sel}}{N_{gen}} = \frac{N_{ps}}{N_{gen}} \cdot \frac{N_{sel}}{N_{ps}} = A_Z \cdot C_Z . \quad (5.13)$$

By definition the numbers N_{gen} and N_{ps} can be calculated already at generator level (section 3.2), whereas N_{sel} takes into account detector simulation processes and efficiencies of the reconstruction and identification algorithms, and needs to be estimated with final reconstructed objects.

For the present analysis the inclusive cross section, $\sigma_{Z/\gamma^*}^{\text{tot.}}$, times branching ratio, BR , for the process $Z^0/\gamma^* \rightarrow \tau^+\tau^- \rightarrow e\mu + 4\nu$ is calculated in an invariant mass range of $66 \text{ GeV} \leq m_{\tau^+\tau^-} \leq 116 \text{ GeV}$. This is done using equations (5.11), (5.12) and (5.13). One obtains:

$$\sigma_{Z/\gamma^*}^{\text{tot.}} \times BR(Z \rightarrow \tau\tau) \times BR(\tau\tau \rightarrow e\mu + 4\nu) = \frac{N_{\text{obs}} - N_{\text{bkg}}}{L \cdot A_Z \cdot C_Z}. \quad (5.14)$$

In contrast, the fiducial cross section times branching ratio is calculated as:

$$\sigma_{Z/\gamma^*}^{\text{fid.}} \times BR(Z \rightarrow \tau\tau) \times BR(\tau\tau \rightarrow e\mu + 4\nu) = \frac{N_{\text{obs}} - N_{\text{bkg}}}{L \cdot C_Z}. \quad (5.15)$$

For the fiducial cross section the acceptance factor A_Z is one and therefore does not take into account the extrapolation to the full phase space. With this, the effect of uncertainties from the modeling of the gauge boson production and its subsequent decays is reduced.

As already mentioned, the acceptance and correction factors A_Z and C_Z are determined with the help of Monte Carlo generated samples. In this case a PYTHIA Monte Carlo sample of the signal process is used. For its generation the modified LO parton distribution functions MRST2007LO* [67] and the corresponding ATLAS MC10 tune [69] are used.

From equation (5.13) the acceptance factor is defined as:

$$A_Z = \frac{N_{ps}}{N_{gen}}. \quad (5.16)$$

The denominator corresponds to the number of generated events with an invariant mass range of $66 \text{ GeV} \leq m_{\tau^+\tau^-} \leq 116 \text{ GeV}$. The invariant mass is determined from the di-tau lepton system, built from the summed four-momenta of their decay products. In detail, these are an electron, a muon and four neutrinos. The momenta of possible photons being radiated either off the τ -lepton before its decay or off the charged decay products within a cone of $\Delta R = 0.1$ are taken into account as well. With this construction, a partial correction of the QED final state radiation back to Born level is achieved. The numerator, N_{ps} , comprises all events which fall inside the fiducial phase space volume, particularly those objects and events which fulfil the following restrictions on generator level:

Electron:	$E_T > 16 \text{ GeV}, \eta < 2.47$ excluding $1.37 < \eta < 1.52$
Muon:	$p_T > 10 \text{ GeV}, \eta < 2.4$
Event:	$\sum \cos(\Delta\phi) > -0.15$ $\sum E_T + E_T^{\text{miss}} < 150 \text{ GeV}$ $25 \text{ GeV} < m_{e\mu} < 80 \text{ GeV}$

With N_{gen} being the number of generated events with an invariant mass range of $66 \text{ GeV} \leq m_{\tau^+\tau^-} \leq 116 \text{ GeV}$, N_{ps} is not necessarily a sub-sample of N_{gen} . Therefore, the construction of the acceptance factor allows to correct for migration of events from outside the invariant mass window into the fiducial cuts. The value obtained with its statistical uncertainty is $A_Z = 0.114 \pm 0.0004$.

The correction factor C_Z which accounts for the detector and analysis efficiencies of triggering, reconstructing and identifying signal events in the fiducial phase space is defined by:

$$C_Z = \frac{N_{sel}}{N_{ps}}. \quad (5.17)$$

Here, the numerator corresponds to those events which pass the full selection described in sections 5.4, 5.5 and 5.6. The denominator is defined just as in the case of A_Z . Again by construction, C_Z allows to correct for events migrating from outside the fiducial phase space into the final signal region. The calculation leads to the following value with its statistical uncertainty $C_Z = 0.286 \pm 0.006$.

5.10 Systematic uncertainties

The total systematic uncertainty of the number of signal and background events is evaluated by considering experimental and theoretical uncertainties. Sources for experimental uncertainties are the efficiency of detecting, measuring and identifying objects in the detector, insufficiencies of the detector itself and the luminosity measurement and deficits in the energy scales and resolutions. The theoretical uncertainty of the number of signal and background events stems from the cross sections taken. Evaluated are the systematic uncertainties on the number of selected events from Monte Carlo simulated samples, as well as on the number of estimated QCD multijet events. A summary of the relative uncertainties is given in table 5.12.

The uncertainty on the acceptance and correction factors A_Z and C_Z is evaluated as well. Whereas the uncertainty on A_Z is based on theoretical sources only, the uncertainty of C_Z is calculated through experimental sources, exclusively.

5.10.1 Uncertainty on signal and background events

Luminosity

Systematic uncertainties on the luminosity from beam-scan measurements at the LHC are estimated to be 3.4% [80].

Vertex multiplicity

Regarding the vertex multiplicity, measured data show different conditions compared to the simulation. To correct for this, the Monte Carlo simulated samples

are reweighted according to the vertex multiplicity distribution from data, as described in section 5.6.7. The systematic uncertainty resulting from this procedure is estimated with the help of the uncertainties of the scaling factors (table 5.4). The scaling factors are shifted coherently by $\pm 1\sigma$, the standard deviation of their uncertainty. With this, the yield of the Monte Carlo simulated samples is estimated once more. The systematic uncertainty obtained through this procedure is estimated to be approximately 0.6%.

It should be mentioned that the ansatz of varying scaling factors by $\pm 1\sigma$ for all bins coherently leads to a conservative estimate of the uncertainty. The largest contribution on the systematic uncertainty for the correction factors arises from limited statistics and, thus, are uncorrelated between the bins. In contrast, by estimating the total uncertainty through the coherent variation by $\pm 1\sigma$ all bins are treated as being correlated.

Jet cleaning

The procedure of jet cleaning removes localised high-energy deposits in the calorimeter, which do not come from beam-beam interactions but are registered by the ATLAS detector. Their source is explained in section 5.6.3. It is applied on data only with a selection efficiency of 99.6%. Instead of reducing the integrated luminosity of the datasample by 0.4%, an additional systematic uncertainty of 0.4% is added to the event yield obtained from simulated Monte Carlo samples.

Trigger

The trigger used for the present analysis is the single electron trigger `EF_e15_medium`. Its efficiency is found to be different in data and Monte Carlo simulations (section 5.6.7). A correction is therefore applied to the generated samples as described in section 5.6.7. The corresponding scaling factors are derived from a tag-and-probe method with $Z^0/\gamma^* \rightarrow e^+e^-$ decays and an orthogonal trigger method with $W^\pm \rightarrow e^\pm\nu_e$ events. The uncertainties on the scaling factors range from 2.5% for electrons with low transverse momentum to 0.5% for electrons with $p_T > 20$ GeV. To estimate the total uncertainty from the scaling of the trigger efficiency the factors are varied by $\pm 1\sigma$, coherently for all bins of p_T . The total yield of the Monte Carlo simulated samples is then obtained with the transformed scaling factors. The total uncertainty of the individual backgrounds varies from 0.4% to 0.8%.

Lepton identification and isolation efficiency

Since Monte Carlo simulated samples and measured data show differences in the efficiency of lepton identification and isolation efficiencies, leptons from the simulated samples are weighted with dedicated scaling factors. For the evaluation of this systematic uncertainty the scale factors are shifted by $\pm 1\sigma$ and the study is repeated to estimate the change of the result with respect to default scaling factors.

In addition to the η and p_T binned electron identification and the electron isolation scale factors, an uncertainty of 1.5% is considered to account for the uncertainty on the reconstruction efficiency. The relative changes of the three mentioned scale factors are added in quadrature. This combined uncertainty is then used to shift the overall scale factor of electrons.

For muons the scale factors for isolation and identification efficiencies are shifted coherently as well. The uncertainty of the isolation efficiency is composed of a statistical and a systematic part. The relative changes of the three mentioned are added in quadrature and used as a combined uncertainty of the muon scaling factor.

Missing transverse energy, energy scale and resolution

The systematic uncertainty of the energy scale of muons is evaluated by varying their transverse momentum by $\pm 1\sigma$, separately for the MUON SPECTROMETER and the INNER DETECTOR. The altered momentum of the muon is then propagated to the calculation of the missing transverse energy. To obtain the total systematic uncertainty of the number of background events the study is repeated.

To evaluate the systematic uncertainty of the calorimetric component of the missing transverse energy calculation, the energy scale of electrons, jets and topological calorimeter clusters not associated with any reconstructed object needs to be shifted coherently. The electron energy scale is varied by $\pm 1\sigma$. Since the uncertainty of the jet energy scale is studied in a wide regime [88], its validation is performed with a dedicated tool provided by the respective combined performance group. The energy of the topological calorimeter clusters are scaled with factors, f , depending on η and the transverse momentum of the cluster:

$$\begin{aligned} f &= 1.01 + \frac{0.07 \text{ GeV}}{p_T} & \text{for } |\eta| < 3.2 \\ f &= 1.1 & \text{for } |\eta| > 3.2 . \end{aligned}$$

The factors are derived from single hadron studies [89], [90]. Scaled are only clusters which cannot be associated with a lepton. This means that they have a geometrical distance of at least $\Delta R > 0.2$.

Because of the specific definition of the missing transverse momentum, the changes of the electron and cluster energy is propagated to the calculation of E_T^{miss} , whereas this is not done for the altered energy of the jets. Again, the systematic uncertainty is estimated by repeating the analysis with the altered values and comparing to the default result.

Electrons from calorimeter regions with detector problems

The procedure of selecting electrons instructs to match them with an $\eta \times \phi$ map in which readout-problems or non-nominal high voltage conditions are stored. With this, electrons built from clusters, which are affected by detector problems, are

avoided. As described in section 5.5, the $\eta \times \phi$ map corresponding to the data taking period with the highest integrated luminosity is chosen to represent all data periods. This data taking period includes about 52% of the data used for this analysis. The fact that only one $\eta \times \phi$ map is chosen, leads to a systematic uncertainty of 0.4% [85].

Method of background estimation

Since the amount of QCD multijet events cannot be evaluated using Monte Carlo simulated samples as described in section 5.8.1, it is estimated from measured data. The matrix method is used, dividing the phase space into four distinct regions. The variables employed are the charge product of the two selected leptons and their isolation. The estimation of the specific background of QCD multijet events is based on three assumptions, namely that:

- the two variables, charge product of the electron-muon pair and their isolation, are uncorrelated for QCD multijet events. This means, that the ratio of events with opposite electric charge to same electric charge, $R^{OS/SS}$, is independent of the isolation of the leptons.
- the selection efficiency, ϵ_{QCD} , is uncorrelated to the variables of electric charge product and isolation of the leptons. This assumption makes it valid to estimate the number of QCD multijet events earlier in the cut flow which is necessary due to limited statistics. The number of events is then being propagated with the efficiency of the subsequent cuts. This efficiency is estimated from a region with high statistics and with QCD multijet events being the dominant ensemble.
- the ratio $R^{OS/SS}$ does not vary with the subsequent cuts after the di-lepton selection.

In this section the validity of these assumptions is investigated and systematic uncertainties are assessed.

The study, whether the ratio of events with opposite electric charge to same electric charge, $R^{OS/SS}$, is independent of the isolation of the leptons, is conducted for electrons and muons, separately. For the estimation of the uncertainty the ratio is exposed as a function of the four variables of the isolation used for electrons and muons, respectively (appendix A.2, figure A.1, from reference [55]). The isolation variables are described in section 5.6.6. If the isolation of the leptons and the ratio, as calculated from measured data events, are independent of each other, the distribution should be flat. Therefore, a linear fit is applied. This fit uses the region of anti-isolation, only. This step is necessary since the region of isolated leptons comprises a significant share of signal events. Since the cross section and therefore the normalisation of the signal process is to be measured, it is not possible to simply subtract this share from the measured data events. If the slope of the fit is consistent with zero within the uncertainties, the assumption of independence between $R^{OS/SS}$ and the lepton isolation is verified. If this is not the case, the systematic uncertainty is estimated as follows [55]:

1. The slope of the fit is extrapolated to the region of isolated leptons, resulting in a hypothetical ratio $R_{ex}^{OS/SS}$.
2. The results of $R^{OS/SS}$ of the anti-isolation region are averaged to one ratio, $R'^{OS/SS}$.
3. The relative uncertainty of the ratio is then evaluated as

$$\frac{R_{ex}^{OS/SS} - R'^{OS/SS}}{R'^{OS/SS}} .$$

With the assumption, that the cluster and track isolation of one specific lepton are fully correlated but independent of the other lepton, the total systematic uncertainty is estimated as the average of the individual contributions from the different variables. The uncertainty of the ratio $R^{OS/SS}$ is estimated in reference [91] with 13.1%. It is dominated by statistics in the selected regions.

The strategy to evaluate the second assumption, whether the selection efficiency is uncorrelated to the electric charge product and the isolation of the leptons, is similar to the one used before. Again the selection efficiency is displayed as a function of the isolation variable (appendix A.2, figure A.2, from reference [55]). The region of anti-isolation is fitted with a straight line and extrapolated to the signal region to a hypothetical $\epsilon_{ex, QCD}$. In addition, the results of ϵ_{QCD} in the anti-isolation region are averaged, resulting in ϵ'_{QCD} . The systematic uncertainty is then calculated as described before, resulting in 2.4% on ϵ_{QCD} . In order to check the correlation to the electric charge product, the selection efficiency is derived with results from the control region C with two leptons of opposite charge. This is in contrast to its definition in equation (5.10), where the efficiency is calculated from the control region of not-isolated, same sign leptons. One obtains:

$$\epsilon_{QCD} = \frac{N_{QCD}^{C, final}}{N_{QCD}^{C, e\mu pair}} = \frac{2100.76}{3759.39} = 0.56 \pm 0.02(\text{stat.}) ,$$

which is the same result as from equation (5.10) and consequently proves the second part of the assumption.

In order to check assumption three whether the ratio $R^{OS/SS}$ is independent of the subsequent cuts after the di-lepton selection, it is calculated as defined in equation (5.9) in the non-isolated regions for each step. In contrast to the isolated regions, the ensemble of selected data shows sufficient statistics. The results are listed in table 5.11. Within the statistical uncertainty they agree among each other which proves the assumption.

Here, it may be referred to reference [56], where the evaluation of systematic uncertainties, stemming from the estimation of the QCD multijet background from data, is executed in more detail.

Table 5.11: Comparison of the ratio $R^{OS/SS}$ after each cut of the selection strategy. The agreement within statistical uncertainties proves the assumption that the ratio is independent of the subsequent cuts.

Cut	$R^{OS/SS}$
2 selected leptons	1.55 ± 0.04
$\sum \cos(\Delta\phi) > -0.15$	1.55 ± 0.05
$\sum E_T + E_T^{\text{miss}} < 150 \text{ GeV}$	1.56 ± 0.05
$25 \text{ GeV} < m_{e\mu} < 80 \text{ GeV}$	1.54 ± 0.05

Cross sections

Uncertainties stemming from the normalisation of Monte Carlo samples and therefore from the choice of the cross section are evaluated for the production of W and Z^0 bosons, as well as for the production of pairs of top anti-top quarks. The former is obtained in the context of the W and Z^0 boson cross section measurement [85] performed by ATLAS. The cross sections are calculated at NNLO accuracy with the programme FEWZ [54, 70]. Their uncertainty is estimated by varying the factorisation and renormalisation scale and by including uncertainties on the parton density functions and the strong coupling constant. The overall uncertainty is found to be 5% for the $W^\pm \rightarrow \ell^\pm \nu$ and $Z^0/\gamma^* \rightarrow \tau^+\tau^- \rightarrow \ell^+\ell^- + 4\nu$ Monte Carlo samples. A similar study is performed for the measurement of the top anti-top quark pair production cross section [92] at ATLAS, including uncertainties on the parton density functions. Here, the overall uncertainty is estimated as $^{+7\%}_{-9.5\%}$.

Table 5.12: Summary of relative systematic uncertainties on simulated Monte Carlo samples and number of estimated events from QCD multijet processes (compare [56] table 5.11). The relative uncertainty is given in %.

Source of Uncertainty	$Z^0/\gamma^* \rightarrow \ell^+\ell^-$	$W^\pm \rightarrow \ell^\pm \nu_\ell$	$t\bar{t}$	est. QCD
Luminosity	3.40	3.40	3.40	3.79
Vertex multiplicity	0.55	0.55	0.58	0.64
Jet cleaning	0.40	0.40	0.40	0.40
Trigger	0.70	0.80	0.40	1.10
Electron identification, isolation	5.38	6.37	5.92	4.66
Muon identification, isolation	1.23	1.82	1.72	4.89
Muon energy scale	0.12	0.00	0.42	0.05
Energy scale of electron, jets, clusters	7.48	11.86	9.27	2.59
Electrons with calorimeter problems	0.37	0.37	0.40	0.30
Method of background estimation	-	-	-	13.30
Cross Sections	5.00	5.00	9.00	5.64
Total systematics	11.1	14.9	14.8	16.7

5.10.2 Uncertainty on the correction factor C_Z

The source of the uncertainty on the correction factor C_Z , as defined in equation (5.17), is of experimental nature, only. It is derived by applying all experimental uncertainties described above to the signal Monte Carlo sample $Z^0/\gamma^* \rightarrow \tau^+\tau^-$ with the factor C_Z being recalculated, respectively. The individual contributions are displayed in table 5.13 and are added in quadrature for the total uncertainty of C_Z . It is evaluated as:

$$\Delta C_Z/C_Z = 6.9\%.$$

Table 5.13: Relative systematic uncertainties of the correction factor C_Z (compare [56] table 5.10).

Source of Uncertainty	$\Delta C_Z/C_Z(\%)$
Vertex multiplicity	0.6
Jet cleaning	0.4
Electron identification, isolation, trigger efficiency	6.1
Muon identification, isolation efficiency	2.6
Energy scale of electron, jets and clusters	1.7
Muon energy scale	0.1
Electron resolution	0.1
Electron charge misidentification	0.3
Electrons with calorimeter problems	0.4
Total uncertainty	6.9

5.10.3 Uncertainty on the acceptance factor A_Z

The uncertainty on the acceptance factor A_Z , defined in equation (5.16), is based on theoretical uncertainties, only. These are the limited knowledge of the proton parton distribution function (PDF) on the one hand and the modeling of the W and Z^0 production at the LHC on the other hand.

As described in section 5.2.3, the set of proton distribution functions used for this work is chosen to be MRST2007LO* [67]. The uncertainty stemming from the specific choice of the PDF set is estimated by reweighting the default sample to different PDF sets. The study makes use of two distinct sets, namely the CTEQ6.6 [68] and the HERA-PDF1.0 [93] proton density functions. The uncertainty is derived from the maximum deviation between the default acceptance and the acceptances obtained with the reweighted samples.

To obtain the uncertainty connected with the choice of the default PDF set, the PDF error eigenvectors of the CTEQ6.6 NLO proton density function are utilised. The uncertainty is estimated by reweighting the default sample to the error eigenvectors and calculating the acceptance with the variations.

For the uncertainty of the modeling of the W and Z^0 production at the LHC the signal process is produced with a different Monte Carlo generator. As an alternative to

the default PYTHIA [22] generator, MC@NLO [64] interfaced with HERWIG [65] for the parton showering is used. Further, the CTEQ6.6 PDF set, the ATLAS MC10 [69] tune and a lower bound on the W and Z^0 boson mass of $m_{Z/W} = 60$ GeV are studied. The uncertainty is calculated as the deviation to the acceptance obtained with the default sample but reweighted to the CTEQ6.6 PDF set instead to the MRST2007LO*. The lower bound is as well $m_{Z/W} = 60$ GeV. While the polarisation of the τ lepton is considered to be treated correctly with the PYTHIA generator, this is not the case for the samples generated with HERWIG in association with an external generator. This effect of the order of 8% is taken into account by correcting the acceptance.

Uncertainties stemming from the modelling of the QED radiation are negligible compared to the uncertainties discussed above. For the default sample the radiation is generated with PHOTOS [66] with an accuracy of better than 0.2%.

The uncertainties obtained are stated in table 5.14. For the total uncertainty they are added in quadratures, resulting in

$$\Delta A_Z/A_Z = 2.9\% .$$

Table 5.14: Relative systematic uncertainties of the acceptance factor A_Z (compare [56] table 5.9).

Source of Uncertainty	$\Delta A_Z/A_Z(\%)$
Choice of PDF set	1.8
Uncertainty within PDF set	1.3
Model dependence on W and Z^0 production	1.8
Total uncertainty	2.9

5.11 Results

5.11.1 Observation of $Z^0/\gamma^* \rightarrow \tau^+\tau^- \rightarrow e\mu + 4\nu$ decays

The previous sections described an approach to select events out of registered proton-proton collisions with the ATLAS detector to measure the cross-section times branching ratio of the process $Z^0/\gamma^* \rightarrow \tau^+\tau^- \rightarrow e\mu + 4\nu$. The number of selected data events and events from simulated signal and background processes is given in table 5.15. The amount of QCD multijet background events is estimated from measured data and stated in the table, as well. At a centre of mass energy of $\sqrt{s} = 7$ TeV with an integrated luminosity of $L = 35.51 \text{ pb}^{-1}$ the ATLAS detector observes 85 data events. The amount of background contribution is estimated to be $10.27 \pm 4.18(\text{stat.}) \pm 1.62(\text{syst.})$. This leaves an observed excess of $74.73 \pm 4.18(\text{stat.}) \pm 1.62(\text{syst.})$ which is compatible with the prediction of $72.91 \pm 1.15(\text{stat.})$ events from the simulated Standard Model Monte Carlo sample. This result was also published in reference [94].

5.11.2 Cross section measurement

For a qualitative comparison with the measured cross sections of $Z^0/\gamma^* \rightarrow e^+e^-$ and $Z^0/\gamma^* \rightarrow \mu^+\mu^-$, the results need to be corrected for the branching ratio of $BR(\tau\tau \rightarrow e\mu + 4\nu)$. With the numbers of table 5.1 one obtains:

$$\begin{aligned} BR(\tau^+\tau^- \rightarrow e\mu + 4\nu) &= 2 \cdot BR(\tau \rightarrow e\nu_e\nu_\tau) \cdot BR(\tau \rightarrow \mu\nu_\mu\nu_\tau) \\ &= 2 \cdot 0.18 \cdot 0.17 \\ &= 0.062. \end{aligned}$$

The fiducial and total cross sections are calculated following equations (5.15) and (5.14). The essential input variables are summarised in table 5.15. With this, the product of the fiducial or total cross section and the branching ratio for the signal process in the mass range of $66 \text{ GeV} \leq m_{\tau^+\tau^-} \leq 116 \text{ GeV}$ at the centre of mass energy of $\sqrt{s} = 7$ TeV is measured as:

$$\begin{aligned} \sigma_{Z/\gamma^*}^{\text{fid.}} \times BR(Z \rightarrow \tau\tau)/\text{pb} &= 119 \pm 16(\text{stat.}) \pm 2(\text{bkg.}) \pm 8(\delta C_Z) \pm 4(\text{lumi.}) \\ &= 119 \pm 16(\text{stat.}) \pm 8(\text{syst.}) \pm 4(\text{lumi.}) \\ \sigma_{Z/\gamma^*}^{\text{tot.}} \times BR(Z \rightarrow \tau\tau)/\text{pb} &= 1041 \pm 143(\text{stat.}) \pm 23(\text{bkg.}) \pm 27(\delta A_Z) \pm 69(\delta C_Z) \\ &\quad \pm 35(\text{lumi.}) \\ &= 1041 \pm 143(\text{stat.}) \pm 78(\text{syst.}) \pm 35(\text{lumi.}) \end{aligned}$$

The statistical uncertainties (stat.) arise from the limited amount of simulated Monte Carlo background samples. The systematic uncertainties (syst.) base on detector and reconstruction uncertainties, on the method of the background estimation and on limited statistics of simulated samples, utilised in the background estimation. Further, the uncertainty stemming from the luminosity measurement (lumi.) is denoted.

Table 5.15: Inputs for the calculation of the fiducial and total cross section with their statistical (stat.) and systematic (syst.) uncertainty (compare [56] table 5.12 and [55] table III).

Observed data events	85
Expected signal events	$72.91 \pm 1.15(\text{stat.})$
Background contribution	
$Z^0/\gamma^* \rightarrow e^+e^-$	$0.02 \pm 0.01(\text{stat.}) \pm 0.00(\text{syst.})$
$Z^0/\gamma^* \rightarrow \mu^+\mu^-$	$1.92 \pm 0.15(\text{stat.}) \pm 0.22(\text{syst.})$
$W^\pm \rightarrow e^\pm\nu_e$	$0.05 \pm 0.05(\text{stat.}) \pm 0.01(\text{syst.})$
$W^\pm \rightarrow \mu^\pm\nu_\mu$	$0.63 \pm 0.17(\text{stat.}) \pm 0.09(\text{syst.})$
$t\bar{t}$	$0.15 \pm 0.03(\text{stat.}) \pm 0.02(\text{syst.})$
QCD est.	$7.5 \pm 4.2(\text{stat.}) \pm 1.3(\text{syst.})$
Total background contribution	$10.3 \pm 4.2(\text{stat.}) \pm 1.3(\text{syst.})$
Integrated luminosity $L[\text{pb}^{-1}]$	$35.51 \pm 1.2(\text{syst.})$
A_Z	$0.114 \pm 0.0004(\text{stat.}) \pm 0.003(\text{syst.})$
C_Z	$0.286 \pm 0.006(\text{stat.}) \pm 0.019(\text{syst.})$

5.12 Discussion

As stated in section 5.2.1, theoretical calculations [59–61] result in a cross section of

$$\sigma_{SM}(pp \rightarrow Z^0/\gamma^* \rightarrow \tau^+\tau^-)/\text{pb} = 964 \pm 48$$

in the invariant $\tau\tau$ mass range of $66 \text{ GeV} \leq m_{\tau^+\tau^-} \leq 116 \text{ GeV}$ at a centre of mass energy of $\sqrt{s} = 7 \text{ TeV}$ for the Standard Model. The result of this analysis is compatible with this prediction.

From the electroweak theory it follows that the branching fraction of the intermediate gauge bosons Z^0 and γ^* for the three families of charged leptons is the same. This means, that the cross section times branching ratio, $\sigma(pp \rightarrow Z^0/\gamma^* \rightarrow \ell^+\ell^-)$, should be the same for all three charged leptons $\ell = e, \mu, \tau$. The cross sections of the processes $Z^0/\gamma^* \rightarrow e^+e^-$ and $Z^0/\gamma^* \rightarrow \mu^+\mu^-$ were measured with the ATLAS detector in the invariant mass range of $66 \text{ GeV} < m_{\ell^+\ell^-} < 116 \text{ GeV}$ with the following results [85]:

$$\sigma_{Z/\gamma^*}^{\text{fid.}} \times \text{BR}(Z^0/\gamma^* \rightarrow e^+e^-)/\text{pb} = 952 \pm 10(\text{stat.}) \pm 26(\text{syst.}) \pm 32(\text{lumi.}) \pm 19(\text{acc.})$$

$$\sigma_{Z/\gamma^*}^{\text{fid.}} \times \text{BR}(Z^0/\gamma^* \rightarrow \mu^+\mu^-)/\text{pb} = 935 \pm 9(\text{stat.}) \pm 9(\text{syst.}) \pm 32(\text{lumi.}) \pm 19(\text{acc.}) .$$

The quoted uncertainties result from statistical (stat.), systematic (syst.), luminosity (lumi.) and from extrapolation (acc.) uncertainties. The three measured cross

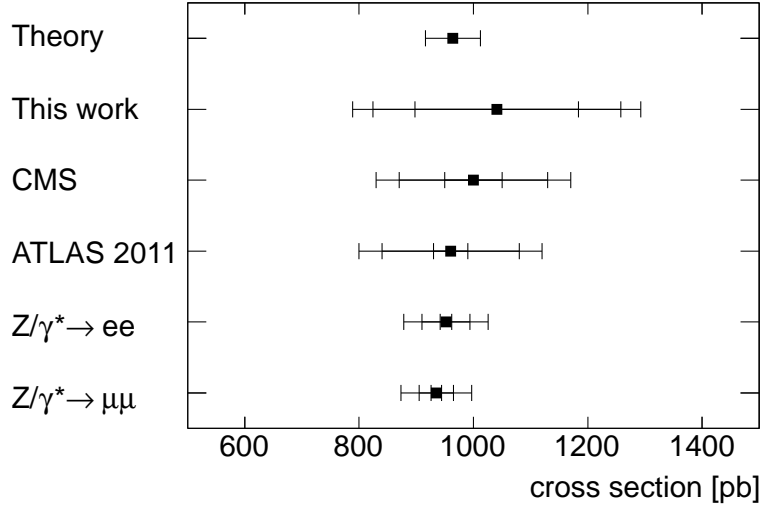


Figure 5.18: Comparison of the cross section measured with this analysis to results from theory and other studies. Given are the statistical, systematic and luminosity induced uncertainties, in this order. If not stated otherwise, the cross section of the process $Z^0/\gamma^* \rightarrow \tau^+\tau^-$ is presented.

sections of proton-proton collisions to Z^0/γ^* decaying to a pair of electrons, muons or τ leptons are compatible within their uncertainties.

The CMS collaboration has measured the $Z^0/\gamma^* \rightarrow \tau^+\tau^-$ cross section as well [95]. The experiment analysed an integrated luminosity of 36 pb^{-1} and an invariant mass range of $60 \text{ GeV} < m_{\tau\tau} < 120 \text{ GeV}$. They combined the results from the semi-leptonic and fully leptonic (electron-muon and muon-muon) τ -decay channels. For the cross section times branching ratio the experiment obtains:

$$\sigma_{Z/\gamma^*}^{\text{tot.}} \times \text{BR}(Z \rightarrow \tau\tau)/\text{pb} = 1000 \pm 50(\text{stat.}) \pm 80(\text{syst.}) \pm 40(\text{lumi.}) .$$

Within their uncertainties, this result is also in agreement with the cross section times branching ratio of this analysis.

The value of the cross section measured with this analysis is presented and compared to results from theory and other studies mentioned above in figure 5.18. The achievements acknowledge a set of predictions. First, they show agreement between theory calculations and the measurement, confirming the cross section calculation including NNLO QCD and electroweak corrections. Secondly, they show an agreement between the measured cross sections for the Z^0 boson decaying to a pair of electrons, muons or τ leptons, as predicted by the lepton universality. Furthermore, the results are compatible with the measurement of the CMS collaboration. This and the successful re-discovery of the massive Z^0 boson of the weak interaction verify the correct functioning of the ATLAS detector. Finally, as mentioned, the process $Z^0/\gamma^* \rightarrow \tau^+\tau^- \rightarrow e\mu + 4\nu$ is the dominant background

to Higgs studies in the τ decay channel in the Standard Model and the Minimal Supersymmetric Standard Model. Because of the same decay kinematics it is not only dominant but even irreducible. The agreement between the measurement and the expected amount of $Z^0/\gamma^* \rightarrow \tau^+\tau^- \rightarrow e\mu + 4\nu$ events (table 5.15) and its mass shape (figure 5.11(f)) show a good comprehension of the $Z^0/\gamma^* \rightarrow \tau^+\tau^-$ decay for the Higgs search.

5.12.1 Comparison with other ATLAS results

The cross section times branching ratio of the process $Z^0/\gamma^* \rightarrow \tau^+\tau^- \rightarrow e\mu + 4\nu$ was measured in reference [55] with the same amount of integrated luminosity with the ATLAS detector. There it was found to be

$$\sigma_{Z/\gamma^*}^{\text{tot.}} \times \text{BR}(Z \rightarrow \tau\tau)/\text{pb} = 1060 \pm 140(\text{stat.}) \pm 80(\text{syst.}) \pm 40(\text{lumi.}) ,$$

which is 2% higher than the result of this analysis but compatible within the uncertainties quoted. This is due to the fact, that the analysis of reference [55] estimates the amount of QCD multijet events slightly differently. The official ATLAS study subtracts the amount of signal events $Z^0/\gamma^* \rightarrow \tau^+\tau^- \rightarrow e\mu + 4\nu$ in the control region B, which is characterised by two isolated leptons with the same electric charge, and uses the theoretical cross section for the normalisation. This study however, does not make use of this approach but leaves the signal contribution untouched. This procedure is chosen since the cross section is the variable to be measured and therefore should neither be used in the background estimation nor in the whole analysis. The amount of QCD multijet events estimated in this study is in that effect slightly higher and therefore reducing the cross section by some pb.

The uncertainty on the cross section measurement is dominated by the statistical uncertainty. The study analyses an integrated luminosity of $L = 35.51 \text{ pb}^{-1}$, which covers the recorded data of the ATLAS detector of the year 2010. A different analysis investigated the data of the year 2011 recorded with the ATLAS detector [96]. It is based on a total integrated luminosity of $L = 1.55 \text{ fb}^{-1}$ and comes to the following result in the invariant $\tau\tau$ mass range of $66 \text{ GeV} < m_{\tau^+\tau^-} < 116 \text{ GeV}$:

$$\sigma_{Z/\gamma^*}^{\text{tot.}} \times \text{BR}(Z \rightarrow \tau\tau)/\text{pb} = 960 \pm 30(\text{stat.}) \pm 90(\text{syst.}) \pm 40(\text{lumi.}) .$$

The outcome is compatible with the cross section measurement of this analysis within the stated uncertainties. The dominant source of uncertainty of the analysis with 2011 data stems from systematic uncertainties. A more precise measurement can therefore only be achieved by reducing these sources of uncertainty.

6 Comparison of mass reconstruction techniques

6.1 Motivation

The first part of this thesis describes the observation and cross section measurement of the Z^0 boson decay to τ -leptons in the mixed leptonic final state, $Z^0/\gamma^* \rightarrow \tau^+\tau^- \rightarrow e\mu + 4\nu$. Besides providing a successful comparison with the theoretically calculated cross section and a good agreement with the experimental value obtained by the ATLAS and the CMS experiment, this measurement is also a preparing analysis searching for the Higgs boson. For low Higgs boson masses, $90 \text{ GeV} < m_H < 160 \text{ GeV}$, the decay to τ -leptons is one of the favoured decay modes in both the Standard Model as well as in the Minimal Supersymmetric Standard Model (MSSM) (figure 5.1). Because of the same decay kinematics of the Higgs boson and the Z^0 boson to τ -leptons, $Z^0/\gamma^* \rightarrow \tau^+\tau^-$ is an irreducible and also dominant background for the Higgs boson search. For this reason it is mandatory to understand the mass shape and cross section of the $Z^0/\gamma^* \rightarrow \tau^+\tau^-$ decay with high precision.

After the independent observation of a new boson at the LHC with the ATLAS detector [2] and the CMS detector [1], characteristics of the boson need to be analysed. Measurements of intrinsic characteristics of the boson indicate whether it may be the Higgs boson. Furthermore, they will reveal with which theory nature might be described (at least in the nowadays accessible energy regime). The particle characteristics are, among others, the mass, the spin and branching fractions.

For the Higgs boson decay into τ -leptons, $H \rightarrow \tau^+\tau^-$, the mass reconstruction is a challenging task. Because of four neutrinos in the final state for the fully leptonic decay, the full reconstruction of the $\tau\tau$ -system is not possible. The mass reconstruction of the semi-leptonic decay is similarly challenging with three neutrinos in the final state. Nevertheless or rather because of this fact, there exists a vast variety of different mass reconstruction techniques. Which mass reconstruction method gives the best performance is dependent on the intended purpose of the analysis and the decay scenario. As indicated, a fully leptonic decay of the $\tau\tau$ final state offers different challenges than the semi-leptonic decay. Furthermore, it is essential whether the mass distribution will be utilised to make an observation of a particle or to measure the Higgs boson mass. A good mass reconstruction therefore depends on a set of different parameters. Analyses studying the performance of a given mass reconstruction technique are usually based on Monte Carlo simulated samples. With this, the mass and the width of the Higgs boson are well known and a comparison of

qualitative and quantitative nature between the mass reconstruction methods can be achieved.

In reference [97] different mass reconstruction techniques are compared for the fully leptonic $H \rightarrow \tau^+\tau^-$ decay in the scope of the background separation, dependency on event variables and the possibility to calibrate the mass of a Higgs boson in the MSSM. That work was supervised and developed in collaboration with the study at hand. This study proceeds with the examination, especially in the scope of an elimination of the dependency from event variables.

6.2 Mass reconstruction methods

In this section four different mass reconstruction techniques are described. All of them reconstruct the invariant mass, $m_{\tau\tau}$, of decays into two τ -leptons. They are based on different input variables, resulting in a different behaviour which is being analysed. As this thesis concentrates on the mixed-leptonic decay to an electron, a muon and four neutrinos, the mass reconstruction techniques are described for this case, exclusively.

In the following sections the notation is as follows. Four-vectors are denoted with a capital letter, P_ℓ^ν , whereas three-dimensional vectors are denoted with a lowercase letter, \vec{p}_ℓ . The four-vector of the missing transverse energy is utilised, as well. By definition, E_T^{miss} is a two-dimensional vector in the $x - y$ plane of the ATLAS detector. With the sum of the transverse momentum of the colliding protons, as well as of the interacting partons being approximately zero, the transverse components of the momenta of particles leaving the detector undetected can be determined. In contrast, it is not possible to determine the z -component. A four-vector of the missing transverse momentum is therefore constructed by setting the z -component to zero. The energy component, E , is built from the square-root of the quadratic sum of the x - and y -components:

$$P^\nu(E_T^{\text{miss}}) = \begin{pmatrix} \sqrt{(E_x^{\text{miss}})^2 + (E_y^{\text{miss}})^2} \\ E_x^{\text{miss}} \\ E_y^{\text{miss}} \\ 0 \end{pmatrix}. \quad (6.1)$$

6.2.1 Visible mass

The visible mass is the most elementary mass reconstruction method. Input variables are the four-vectors of the visible τ -decay products, namely the electron and the muon. Additional energy and momenta of the four neutrinos, which leave the detector undetected and are therefore invisible, are neglected. The visible mass is defined as:

$$m_{\text{vis}} = \sqrt{\left(\sum_\ell P_\ell^\nu\right)^2} = \sqrt{(P_e^\nu + P_\mu^\nu)^2}. \quad (6.2)$$

With the usage of only well-known particle attributes the visible mass produces a sharp mass distribution. For this reason, this method is favoured for analyses with the purpose of observing new particles. On the other hand, this method will, by definition, not reproduce the true invariant mass of the $\tau\tau$ -system, but a lower mass instead. Nevertheless, this circumstance can be corrected for by finding a calibration function between the reconstructed visible mass and the invariant $m_{\tau\tau}$ mass.

6.2.2 Effective mass

By utilising the four-vector of the missing transverse energy, $P^\nu(E_T^{\text{miss}})$, the effective mass [98] includes energy information coming from the four neutrinos. Similar to the visible mass, this mass definition is constructed from the sum of the four-vectors of the light leptons and additionally of the missing transverse energy:

$$m_{eff} = \sqrt{(P_e^\nu + P_\mu^\nu + P^\nu(E_T^{\text{miss}}))^2}. \quad (6.3)$$

Because of the additional information from the missing transverse energy, the effective mass leads to results closer to the invariant mass, than the visible mass. Still, the reconstructed mass does not reproduce the invariant mass, since the value of the missing transverse energy is always underestimated with respect to the real missing energy, carried away by the neutrinos, as described in section 5.2.1.

As a further unfavourable item the distribution of the reconstructed mass is broader than that for the visible mass. This effect stems from the measurement of the missing transverse momentum, as the reconstruction of E_T^{miss} is a complicated procedure with a limited accuracy.

6.2.3 Projected transverse mass

A different mass reconstruction method concentrates on the summation and the projection to the transverse plane of the four-vectors of the decay products. Reference [99] distinguishes between the order of the projection and the summation, explicitly. The masses are built from the vectorial sum of the visible and invisible decay products. The early projection method projects the four-vectors first into the transverse plane and then sums up the constituents of the visible or invisible decay products, separately. The projection transforming a four-vector with one energy-like and three momentum-like components to a transverse four-vector with one energy-like and two momentum-like components. This procedure yields the early projected transverse mass, \mathcal{M}_{TS} . The so-called late projected transverse mass, \mathcal{M}_{ST} , switches the order and sums first the constituents and projects them to the transverse plane, afterwards. The order of summation and projection is indicated by the labels. For projecting first and then summing up the constituents the label $\{TS\}$ is used, whereas the switched order is denoted with $\{ST\}$.

Bearing in mind the relation

$$E = \sqrt{M^2 + \vec{p}^2} = \sqrt{M^2 + \vec{p}_T^2 + p_z^2},$$

with M being the invariant mass of the four-vector, the energy component is projected to the transverse plane via

$$e_T = \sqrt{M^2 + \vec{p}_T^2} = \sqrt{E^2 - p_z^2}.$$

The early projected transverse mass, \mathcal{M}_{TS} , and the late projected transverse mass, \mathcal{M}_{ST} , are then defined as:

$$\mathcal{M}_{TS} \equiv \sqrt{g_{\mu\nu}(P_{TS}^\mu + Q_{TS}^\mu)(P_{TS}^\nu + Q_{TS}^\nu)} \quad (6.4)$$

$$\mathcal{M}_{ST} \equiv \sqrt{g_{\mu\nu}(P_{ST}^\mu + Q_{ST}^\mu)(P_{ST}^\nu + Q_{ST}^\nu)}, \quad (6.5)$$

where P_{TS}^ν and P_{ST}^ν are projected (1+2) vectors of the sum of visible decay products and Q_{TS}^ν and Q_{ST}^ν the hypothetical (1+2) vector of the ensemble of invisible particles of the event. A central assumption is the constraint that the missing momentum of an event stems from the momenta, \vec{q}_i of the N_u undetected decay particles, exclusively. Under exploitation of momentum conservation in the transverse plane the missing momentum, \vec{q}_T , is obtained from the sum of the N_v visible decay products:

$$\sum_i^{N_u} \vec{q}_{Ti} = \vec{q}_T = - \sum_j^{N_v} \vec{p}_{Tj}. \quad (6.6)$$

As only the vectorial sum of the missing momentum is known but not its constituents, formulae (6.4) and (6.5) are minimised over all possible values of the unknown invisible momenta consistent with this constraint. This leads to

$$m \equiv \min_{\sum_i^{N_u} \vec{q}_{Ti} = \vec{q}_T} [\mathcal{M}]. \quad (6.7)$$

The minimisation is always well-defined and leads to an analytical solution [100]. With the minimisation, a lower bound on the calculated mass is obtained. It guarantees that the result gives always lower values than the mass of the decaying particle. Therefore, the early and late projected transverse mass yield mass values which do not provide a mass distribution but rather a mass bound.

The experiment obtains the missing transverse momentum from the sum of energy deposits in the calorimeter and tracks of the muon detector. Therefore, the definition of E_T^{miss} also includes the energy of possible jets in the event. For the Higgs boson decay into two τ -leptons and further to an electron-muon pair and four neutrinos, this leads to:

$$\vec{p}_{\text{miss}} = -\vec{p}_e - \vec{p}_\mu - \vec{p}_{\text{jets}}. \quad (6.8)$$

Especially in the b -quark associated Higgs boson production (section 6.3.1), jets are present in the event. However, they do not stem from the decay of the Higgs boson. To obtain the invariant $\tau\tau$ -mass, $m_{\tau\tau}$, it is therefore necessary to subtract their contribution from the measured missing momentum. Using the definition of

the measured missing transverse momentum (6.1), the minimisation (6.7) and equation (6.8) the formulae of the early (6.4) and late projected transverse mass (6.5) can be rewritten as:

$$m_{TS} = \sqrt{\left(\sum_{\ell}^{\ell=e, \mu} \sqrt{M_{\ell}^2 + \vec{p}_{T\ell}^2} + \vec{p}_T(E_T^{\text{miss}})\right)^2 - (\vec{p}_{Tjets})^2} \quad (6.9)$$

and

$$m_{ST} = \sqrt{\left(\sqrt{M_{e, \mu}^2 + \vec{p}_{Te, \mu}^2} + \vec{p}_T(E_T^{\text{miss}})\right)^2 - (\vec{p}_{Tjets})^2}. \quad (6.10)$$

The index ℓ runs over the visible decay products of the final state, the electron and the muon. The invariant mass, $M_{e, \mu}$, as well as the transverse momentum vector, $\vec{p}_{Te, \mu}$, are components of the summation of the electron and the muon four-vectors. If there are no jets present in the event, the transverse momentum \vec{p}_{Tjets} is set to zero.

It is obvious, that with the early projected transverse mass, information about the longitudinal constituents are lost by transforming first to the transverse plane and then executing the summation. The late projected mass, on the other hand, contains all information of the longitudinal and the transverse component.

As explained with the minimisation in equation (6.7) a lower bound on the calculated mass is obtained. However, the mass distributions obtained from measured quantities do not reflect this fact. Instead, the distributions obtained are washed out, delivering Poission-like mass distributions. The reason for this stems from the resolution of the input variables, in particular the resolution of the missing transverse energy.

6.3 Signal and background processes

6.3.1 Signal process

The production of a neutral Higgs boson in the MSSM is driven by the direct and the b -quark associated production [40]. The direct production is realised through a gluon fusion process. Possible Feynman graphs of the production are displayed in figure 6.1 and 6.2. The b -quark associated production can be described as Higgs boson radiation off a b -quark. For large $\tan\beta$ it is enhanced¹ because of the relatively large Yukawa coupling to b -quarks. Other processes like vector boson fusion or Higgs-strahlung are suppressed or even absent due to the coupling between neutral Higgs bosons of the MSSM and vector bosons. This analysis takes into account the b -quark associated Higgs boson production, only. Nevertheless, it may be extended to the gluon fusion production process with little effort. With the dedicated software

¹The variable $\tan\beta$ is the tangent of the ratio of the vacuum expectation values of the two Higgs doublets in the MSSM.

the masses, branching ratios and couplings of the neutral CP-even MSSM Higgs boson can be calculated. At tree level, the cross sections of the production processes are dependent on the mass of the CP-odd Higgs boson, m_A , and the variable $\tan\beta$. The other parameters of the MSSM are defined within the m_h^{max} scenario (section 2.2.1).

As depicted in figure 5.1(b) in section 5.1 for the low mass regime, the decay into two b -quarks or two τ -leptons is favoured, yielding the second highest branching ratio. The analysis concentrates on the latter decay with a subsequent decay to an electron-muon pair plus four neutrinos, $\phi \rightarrow \tau^+\tau^- \rightarrow e\mu + 4\nu$. Here, ϕ stands for either of the three neutral Higgs boson, $h/H/A$. The event kinematics are similar to the decay of the Z^0 boson to two τ -leptons as described in section 5.2.1. In most of the cases, the Higgs boson is produced with only a small transverse momentum, for which reason the decay products are emitted in a back-to-back topology. The resulting measured missing transverse energy is therefore relatively small. If nothing else, E_T^{miss} always underestimates the sum of the non visible momenta of the neutrinos, making the exact determination of the invariant mass of the decay products impossible.

The transverse momentum of the Higgs boson is larger than zero when having b -quarks in the final state (e.g. figure 6.1(b) and 6.1(c)). In the b -quark associated Higgs boson production, jets stemming from the b -quark in the final state exhibit a transverse momentum. For reasons of momentum conservation, the transverse momentum of the Higgs boson increases as well.

For this analysis, Monte Carlo simulated samples of the b -quark associated Higgs boson production process are utilised. The samples are simulated at a centre of mass energy of $\sqrt{s} = 7$ TeV with the software SHERPA [21]. This generator conducts the event generation, initial and final state radiation as well as the hadronisation. The samples are further processed making use of ATHENA release 17.0.5. The samples are generated with the mass of the neutral CP-odd Higgs boson ranging from $90 \text{ GeV} \leq M_A \leq 200 \text{ GeV}$, in 20 GeV steps up to $m_A = 170 \text{ GeV}$ and separately for $m_A = 200 \text{ GeV}$. The value of $\tan\beta$ is fixed at $\tan\beta = 20$.

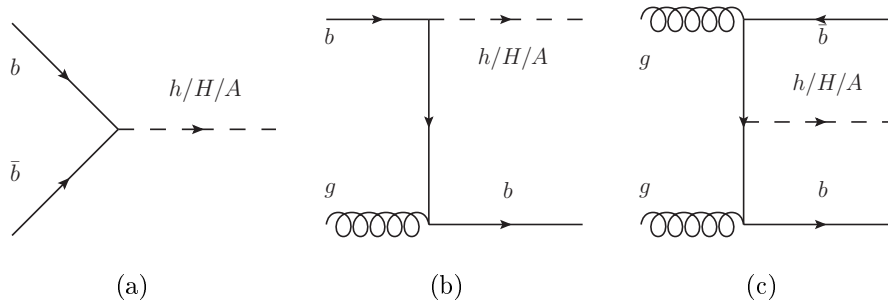


Figure 6.1: Possible Feynman graphs for the b -quark associated Higgs boson production in proton-proton collisions at the LHC.

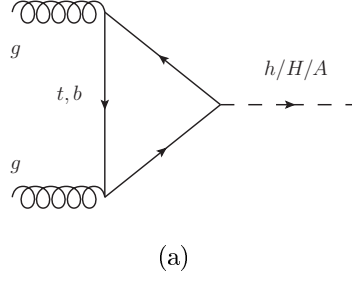


Figure 6.2: Possible Feynman graph for the gluon fusion Higgs boson production.

6.3.2 Background processes

For the mass reconstruction analysis of the Higgs boson decay into two τ -leptons the two largest contributing background processes are discussed in the following. These are the Z^0 boson decay to a τ -lepton pair and the decay of a top anti-top quark pair.

- $Z^0/\gamma^* \rightarrow \tau^+\tau^-$: This decay is dominant for low Higgs boson masses ($m_A \approx 100$ GeV), with the invariant mass of the Z^0 boson being $m_Z = 91.2$ GeV [5]. As mentioned, the process is not only dominant but irreducible at low Higgs boson masses having the same decay kinematics as the signal process. The Monte Carlo simulated sample is generated at a centre of mass energy of $\sqrt{s} = 7$ TeV with the generator PYTHIA v6.423 [22], interfaced with PHOTOS [66] for final state QED radiation and TAUOLA [63] for simulation of τ -leptons. Like SHERPA, PYTHIA conducts the event generation, initial and final state radiation as well as the hadronisation.
- $t\bar{t}$: The second background is dominant for higher masses of the Higgs boson ($m_A \approx 170$ GeV). The fully leptonic decay of the top anti-top quark pair is a direct background to the signal process. However, also the semi-leptonic and fully hadronic decay give contributions if at least one or two additional jets are present. The jets may comprise light hadrons which decay into real leptons and therefore mimic the signal process. Furthermore, the jet may also provide characteristics, being misinterpreted as a lepton candidate. The Monte Carlo simulated sample of this background process is generated using MC@NLO v3.3 [64]. For the generation of the parton shower and the hadronisation, the sample is interfaced to HERWIG [65].

Both background samples are processed with the ATHENA release 17.0.5.

6.4 Selection strategy

For the analysis of different mass reconstruction methods of a boson decaying to two τ -leptons and further to an electron, a muon and four neutrinos, a simple event selection is conducted. This selection is not optimised for a Higgs boson observation, nor for a precise measurement of its properties, but a basic selection of an electron-muon pair with reasonable additional decay characteristics. To be consistent, it is in line with the selection strategy of the cross section measurement of $Z^0/\gamma^* \rightarrow \tau^+\tau^- \rightarrow e\mu + 4\nu$. Furthermore, it is in line with the selection of measured data events of Higgs boson analyses conducted so far [58].

6.4.1 Object selection

Electrons

As described in section 4.5.1 electrons are reconstructed using a sliding window of a set of cells in the $\eta-\phi$ plane of the ELECTROMAGNETIC CALORIMETER. The sliding window searches for energy deposits in the calorimeter which can be matched with reconstructed tracks of the INNER DETECTOR. For the identification of electron candidates this analysis makes use of the class **Tight**. The electron identification places requirements on shower shape variables and hadronic leakage, on the track quality, the track-cluster matching and on energy deposits in the strip layer of the ELECTROMAGNETIC CALORIMETER [45]. To make use of information from the inner tracking system, the pseudorapidity range is set to $|\eta| < 2.47$, excluding the transition region between the barrel and the end-cap calorimeters, $1.37 < |\eta| < 1.52$. The electron candidate is only accepted if the absolute value of its reconstructed charge is unity and is reconstructed by the standard or the soft electron algorithm (section 4.5.1). Furthermore, the transverse momentum is set to be larger than $p_T > 15$ GeV.

Muons

Muons used in this analysis are reconstructed through a matching combination of tracks in the INNER DETECTOR and the MUON SPECTROMETER (section 4.5.2). Further identification requirements are set on the track quality of the INNER DETECTOR track (section 5.5). The difference, z_0 , between the z -position of the muon track extrapolated to the beam line and the z -position of the primary vertex must be less than 10 mm to reduce contamination from cosmic muons. Similar to the electron candidate selection, the absolute value of the charge of muon candidates must be unity. Last, the transverse momentum must exceed $p_T > 10$ GeV and the pseudorapidity range is set to $|\eta| < 2.5$.

Jets

The jets used in this analysis are reconstructed with the anti- k_t algorithm with a distance parameter of $R_\tau = 0.4$ (section 4.5.4). The inputs are three-dimensional

topological calorimeter energy clusters [48] which are noise suppressed. The pseudorapidity range of the jet candidates is set to $|\eta| < 2.5$. Furthermore, they should exceed a transverse momentum of $p_T > 20$ GeV.

Overlap ambiguity

Different reconstruction algorithms may reconstruct objects originating from the same track of the INNER DETECTOR or the same energy deposit in the calorimeters. To avoid double counting of objects, these overlap ambiguities are resolved by ordering and giving priorities to the reconstructed objects. As described in section 5.5 a procedure is employed which searches for objects overlapping in the $\eta \times \phi$ space. An overlap is given if they are located within the distance parameter $\Delta R = \sqrt{\Delta\phi^2 + \Delta\eta^2}$. It is resolved by selecting muons, electrons and jets in the following ordering with the distance parameters chosen as:

- a muon is selected if it overlaps with a muon or an electron within $\Delta R < 0.2$ or a jet within $\Delta R < 0.4$,
- an electron is selected if it overlaps with an electron within $\Delta R < 0.2$ or a jet within $\Delta R < 0.4$,
- a jet is selected if it overlaps with another jet within $\Delta R < 0.4$.

If objects of the same class overlap, then the one with the higher transverse momentum is selected.

Missing transverse energy

The reconstruction of missing transverse energy is based upon energy deposits in the calorimeter and on reconstructed muon tracks. A detailed explanation of the method is given in section 4.5.5). The construction of a four-vector of the missing transverse momentum is described in section 6.2.

6.4.2 Event Selection

Vertex multiplicity

Events of the simulated Monte Carlo samples are accepted if they contain at least one vertex with more than three associated tracks. This cut is introduced to obtain an event sample which is as similar to the selected data as possible.

Selection of a lepton pair

The selection of events stemming from a Higgs boson decay into two τ -leptons and further to an electron and a muon is conducted by demanding exactly one reconstructed electron candidate and one reconstructed muon candidate. The pair ought to have opposite electric charge. These leptons are geometrically isolated in the

detector. For the event selection a dedicated cut is conducted, cutting on variables which investigate the transverse energy or the transverse momentum around a lepton. In detail, the transverse momenta of all tracks coming from the same vertex as the light lepton are summed up. They must exceed $p_T > 1$ GeV and should be in a cone of $\Delta R = 0.4$ around the lepton. The resulting transverse momentum must be less than 6% of the lepton transverse momentum. The same applies to the transverse energy of calorimeter cells in a cone of $\Delta R = 0.2$ around the lepton. Here, it must be less than 8% of the electron transverse momentum and 4% of the muon p_T . The values of the isolation variables are in line with the Higgs boson selection of reference [58].

A summary of the object and event cuts applied is given in table 6.1.

Table 6.1: Summary of the cuts to select events stemming from the Higgs boson decay $\phi \rightarrow \tau^+\tau^- \rightarrow e\mu + 4\nu$.

Object Selection	
Electrons	$E_T > 15$ GeV, $ \eta < 2.47$, $1.37 < \eta < 1, 52$ identified with class Tight unit charge
Muons	$p_T > 10$ GeV, $ \eta < 2.5$ combined INNER DETECTOR and MUON SPECTROMETER track $ z_0 < 10$ mm pass quality criteria on INNER DETECTOR tracks unit charge
Jets	anti- k_T algorithm with distance parameter $\Delta R = 0.4$ $p_T > 20$ GeV, $ \eta < 2.5$
Missing transverse energy	$\vec{E}_T^{\text{miss}} = \vec{E}_T^{\text{miss}}(\text{calo}) + \vec{E}_T^{\text{miss}}(\mu)$
Overlap ambiguity	$\mu - \mu$: $\Delta R = 0.2$ $e - e, \mu$: $\Delta R = 0.2$ jet- e, μ, jet : $\Delta R = 0.4$
Event Selection	
Vertex	$n_{vtx} \geq 1$ with $n_{trk} \geq 3$
Lepton pair	$N_e = 1$ and $N_\mu = 1$ $q_e \cdot q_\mu = -1$
Isolation	electron: $E_T^{0.2}/p_{Te} < 0.08$ and $p_T^{0.4}/p_{Te} < 0.06$ muon: $E_T^{0.4}/p_{T\mu} < 0.04$ and $p_T^{0.4}/p_{T\mu} < 0.06$

6.5 Comparison of mass reconstruction methods

This section compares the behaviour of the different mass reconstruction techniques, described in section 6.2. Similar to reference [97], the following points are emphasised:

- the bias between the generated and the mean $\langle m \rangle$ of the reconstructed mass,
- the width of the distribution, calculated as the relative standard deviation, $\sigma_{rel} = \sigma / \langle m \rangle$, with σ being the standard deviation of the distribution and
- the separation power with respect to the background processes.

The separation power is evaluated by the search for an optimal cut value on the reconstructed mass at which the signal is separated from background processes. To derive the cut value, the figure of merit $N_S / \sqrt{N_B}$, the fraction of selected signal events, N_S , with respect to the square root of the number of selected background events, N_B , is utilised. With the selection strategy being not optimised for an observation or a high-precision measurement, but being rather a basic selection of an electron-muon pair, the mass distributions are scaled to the number of selected events. For this analysis the figure of merit is chosen, since the respective cross sections of the signal and background processes, σ_S and σ_B , can be neglected. The optimal cut value, at which the signal is separated from the background, is searched for by finding the maximum of (see also section 5.3):

$$\Sigma = \frac{N_S}{\sqrt{N_B}} \quad (6.11)$$

This procedure gives reasonable results, since for the separation power the cut values found are compared among different mass reconstruction techniques but not to form a significance.

The mass distributions, scaled to the number of selected events, are given in figure 6.3. They show the signal process $\phi \rightarrow \tau^+ \tau^-$ at different mass points in the range $90 \text{ GeV} \leq m_A \leq 200 \text{ GeV}$, and the two background samples utilised, $Z^0/\gamma^* \rightarrow \tau^+ \tau^-$ and $t\bar{t}$.

It can be seen that the visible mass, equation (6.2), gives the lowest values for the mean of the distributions. The other three mass definitions yield values which are comparable. It is obvious, that the behaviour of the $t\bar{t}$ background is different with respect to the reconstruction methods, whereas the signal process at different mass points and the $Z^0/\gamma^* \rightarrow \tau^+ \tau^-$ background respond similarly. The observations are quantified in table 6.2, exemplarily for the mass points $m_A = 90 \text{ GeV}$, 130 GeV , 200 GeV .

From table 6.2 it can be seen, that the visible mass gives the largest bias with respect to the generated mass. For the mass points chosen the bias composes approximately half the mass. The bias of the late projected mass, on the other hand, is the smallest but increases with m_A like for all mass reconstruction

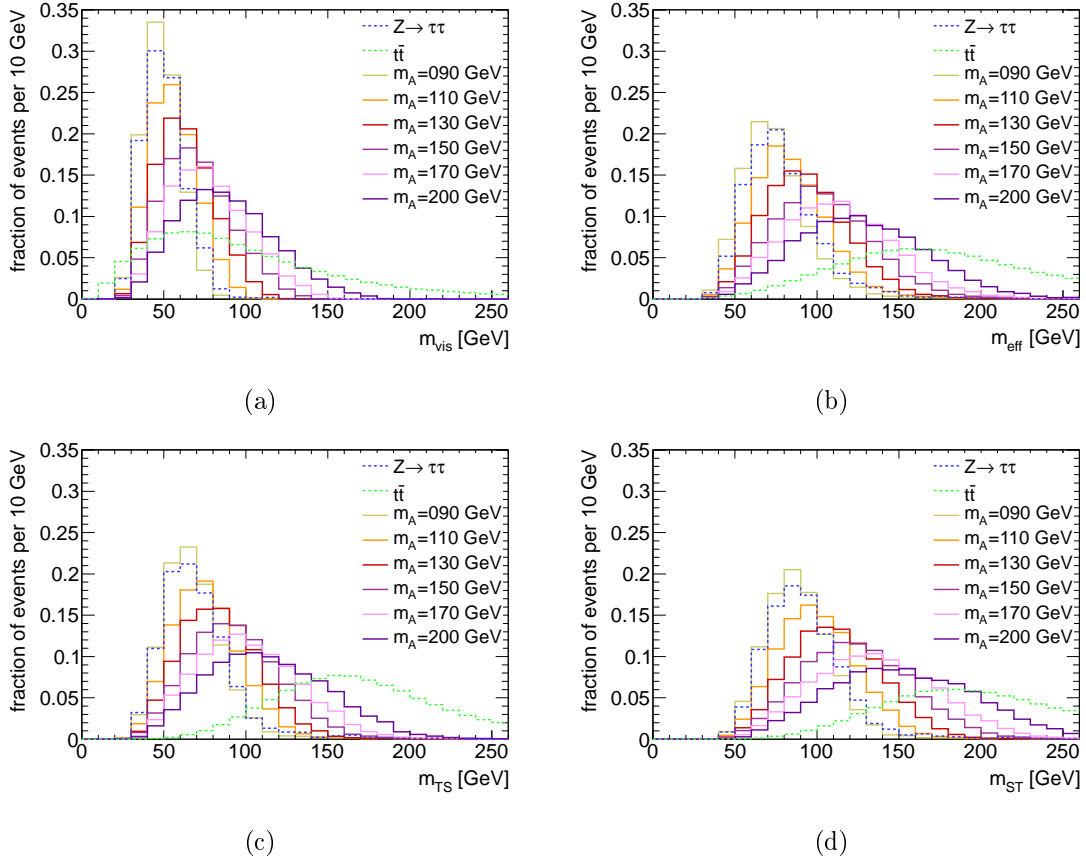


Figure 6.3: Distribution of the (a) visible mass, (b) the effective mass, (c) the early projected and (d) the late projected transverse mass. Depicted are the signal process $\phi \rightarrow \tau^+\tau^-$ and the background processes $Z^0/\gamma^* \rightarrow \tau^+\tau^-$ and $t\bar{t}$. The distributions are scaled to the number of selected events. The value $\tan\beta$ is fixed to $\tan\beta = 20$.

techniques. Another variable, which is used for the comparison, is the relative standard deviation, σ_{rel} , of a distribution. It is desired to be small, which means that the distributions ought to be sharp to yield a good separation power. It is also desired to be small for an accurate mass determination if through calibration the bias can be reduced to zero. This is discussed in section 6.7. The relative standard deviation is the smallest for the visible mass. This is the case, as this reconstruction technique considers only the two visible decay products, which can be measured with high precision. The other techniques discussed utilise the amount of the measured missing transverse energy as a further input which has a worse resolution. On the one hand, this results in reconstructed masses closer to the generated mass, as can be seen from the table. On the other hand, with this the resolution of E_T^{miss} is a further limiting factor, broadening the mass distribution. The early projected transverse mass gives the largest values for σ_{rel} . This results from the early projection to the transverse plane before executing the summation

Table 6.2: Quantitative mass reconstruction comparison for selected Higgs boson mass points. Given is the mean and the bias with their statistical uncertainty. Furthermore, the relative standard deviation, σ_{rel} , of the mass distribution and the separation power, $\Sigma = N_S/\sqrt{N_B}$, with respect to the background sources $Z^0/\gamma^* \rightarrow \tau^+\tau^-$ and $t\bar{t}$ (compare [97], table 4.1 and 6.1). The statistical uncertainty on σ_{rel} can be neglected.

	mean (GeV)	bias (GeV)	σ_{rel}	$\Sigma_{Z \rightarrow \tau\tau}$	$\Sigma_{t\bar{t}}$
m_{vis}					
$m_A = 90.00$ GeV	49.02 ± 0.13	-40.98 ± 0.13	0.23	1.00	1.60
$m_A = 130.00$ GeV	63.55 ± 0.17	-66.45 ± 0.17	0.28	1.28	1.28
$m_A = 200.00$ GeV	88.22 ± 0.23	-111.78 ± 0.23	0.33	5.26	1.08
m_{eff}					
$m_A = 90.00$ GeV	74.48 ± 0.23	-15.52 ± 0.23	0.27	1.01	3.34
$m_A = 130.00$ GeV	94.16 ± 0.25	-35.84 ± 0.25	0.28	1.07	2.11
$m_A = 200.00$ GeV	128.20 ± 0.31	-71.80 ± 0.31	0.31	2.30	1.27
m_{TS}					
$m_A = 90.00$ GeV	68.69 ± 0.24	-21.31 ± 0.24	0.30	1.00	6.21
$m_A = 130.00$ GeV	84.84 ± 0.23	-45.16 ± 0.23	0.29	1.06	3.26
$m_A = 200.00$ GeV	114.14 ± 0.30	-85.86 ± 0.30	0.33	2.25	1.53
m_{ST}					
$m_A = 90.00$ GeV	89.68 ± 0.26	-0.32 ± 0.26	0.25	1.00	5.07
$m_A = 130.00$ GeV	112.53 ± 0.27	-17.47 ± 0.27	0.25	1.16	2.52
$m_A = 200.00$ GeV	153.11 ± 0.35	-46.89 ± 0.35	0.29	2.98	1.25

of the particle constituents. With this procedure, momentum components in the longitudinal plane are neglected, yielding a less precise mass reconstruction.

Besides providing a sharp distribution, a good mass reconstruction should also isolate the distributions of the signal and the background. To quantify this ability, the separation power as defined in equation (6.11) is exploited. Table 6.2 shows that the separation power with respect to the Z^0 boson background decay into two τ -leptons is very similar among the different techniques for the low mass points. This is due to the same decay kinematics of the signal and this background process. For higher masses, the visible mass gives the highest separation power, because of the non-usage of E_T^{miss} , which leads to a better resolution of the reconstructed mass. The distributions of the top-pair decay background respond differently. The mass reconstruction method of the visible mass yields a separation power which is similar for all mass points chosen. For other reconstruction techniques, the separation power changes with different Higgs boson masses. This behaviour results from the fact, that the decay of an top anti-top quark pair has a different decay kinematic with respect to the Higgs boson decay into two τ -leptons. In particular, the selected lepton pair of the $t\bar{t}$ background has similar momentum values compared to the signal. With this being the only input variables of the visible mass, the resulting mass distributions are similar. In contrast,

the $t\bar{t}$ background yields larger values for the missing transverse momentum than the signal. For this reason, a larger separation power is obtained for the other mass reconstruction methods. The highest separation power at low Higgs boson mass points can be achieved with the early and late projected transverse mass.

Taking into account both background sources analysed, $Z^0/\gamma^* \rightarrow \tau^+\tau^-$ and $t\bar{t}$, the mass reconstruction techniques yielding the best performance at low Higgs boson masses, $m_A \approx 90$ GeV, is the early and the late projected transverse mass. Considering a Higgs boson of intermediate mass, $m_A \approx 130$ GeV, as being probable with the recent discoveries, the highest separation power is obtained with the late projected transverse mass. Taking into account $t\bar{t}$ as the only background source, the early projected transverse mass delivers the highest separation power, whereas for $Z^0/\gamma^* \rightarrow \tau^+\tau^-$ this would be the visible mass. For a mass reconstruction method choice for high Higgs boson masses of approximately $m_A \approx 200$ GeV, it is necessary to analyse which of the background sources is the dominant one. If the top anti-top quark pair gives the higher contribution, the mass reconstruction technique of the effective mass and the early projected transverse mass yield the best performance. For $Z^0/\gamma^* \rightarrow \tau^+\tau^-$ this would be the visible mass and the late projected transverse mass.

The comparison of mass reconstruction methods in reference [97] comes to similar conclusions.

6.6 Variable dependence

6.6.1 Dependency on event variables

Besides providing a good signal-to-background separation and a possible calibration to the real invariant mass, a good mass reconstruction technique should be independent of event variables. If a reconstruction method shows a dependency on such a variable, it is evident that either not all necessary information is used for the mass calculation or the variable is under- or overestimated in a certain range. If this is the case, the mass reconstruction is not robust.

As an example, the definition of the visible mass, c.f. equation (6.2), makes use of only a part of the possible event information. In particular, it does not use the missing transverse momentum, but only the four-vectors of the electron-muon pair. It is therefore expected that it shows a strong dependency on E_T^{miss} . Because of the energy conservation of the decay, with a rising value of the missing energy the momenta of the leptons decrease. The mass distribution of the visible mass would therefore be expected to be decreasing with increasing missing transverse energy. With an ideal mass reconstruction technique the width of the resulting mass distribution would reproduce the natural width of the Z^0 or the Higgs boson. As none of the introduced mass reconstruction techniques can make use of the real missing energy it is expected that all methods show a dependency on the momenta of the leptons and on E_T^{miss} .

For the present analysis, the robustness of the reconstruction methods with respect

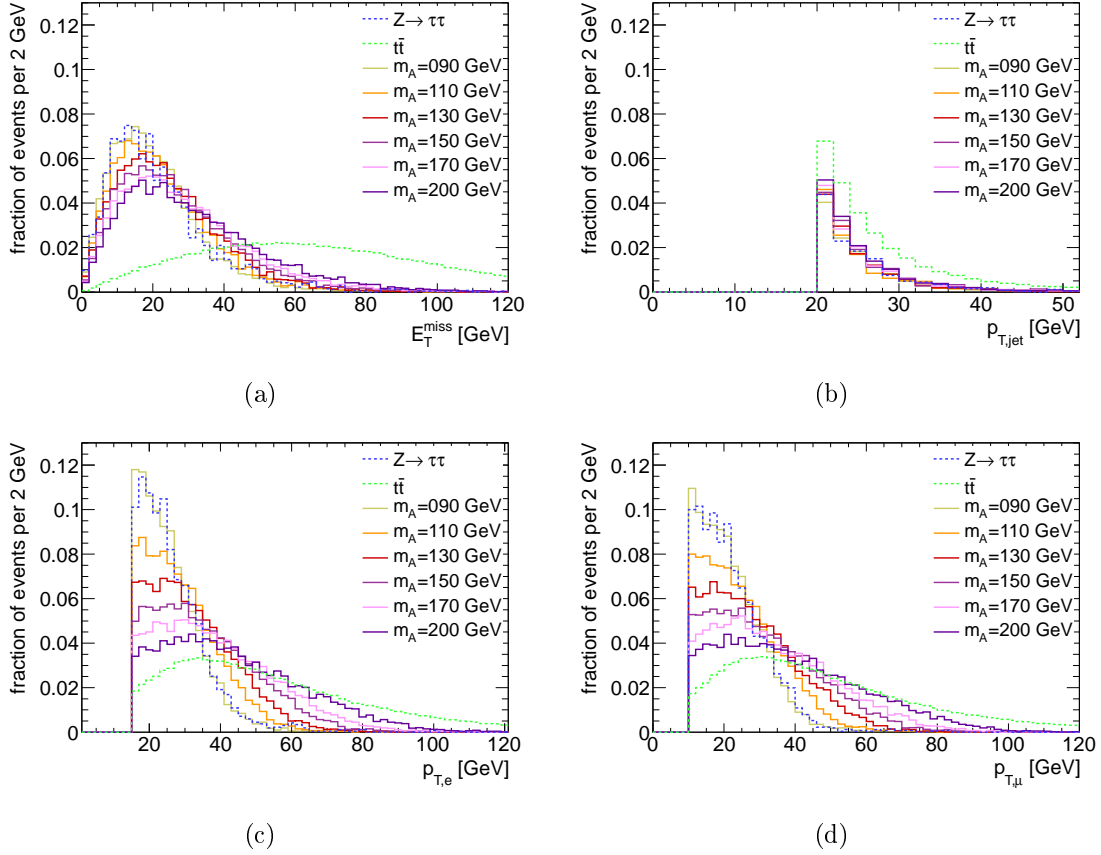


Figure 6.4: Distribution of (a) the missing transverse energy, (b) the transverse momentum of the leading jet, (c) of the electron and (d) the muon after the full object and event selection. The distributions are scaled to the number of selected events. Events from $t\bar{t}$ decays yield more jets in the final state than the signal and $Z^0/\gamma^* \rightarrow \tau^+\tau^-$.

to the missing transverse energy, the transverse momentum of the light leptons and of the jet with the highest p_T are examined. In the following, the jet with the highest p_T will be denoted as the leading jet. For the signal process the dependency on the missing transverse energy as well as on the p_T of the leading jet is examined in [97]. Those results will be compared with this work in the subsequent sections. Figure 6.4 presents distributions of the variables mentioned for the signal process at certain mass points and the background sources $Z^0/\gamma^* \rightarrow \tau^+\tau^-$ and $t\bar{t}$ after the full object and event selection, c.f. table 6.1. If a selected event does not contain a jet, it is not considered for the variable dependency on the transverse momentum of the leading jet. This fact explains the excess of $t\bar{t}$ events in figure 6.4(b), as this process contains more selected events with at least one jet than the signal or $Z^0/\gamma^* \rightarrow \tau^+\tau^-$ process. It is confirmed in [97] that the mass reconstruction methods are independent from pile-up, additional proton-proton interactions (section 4.3). This proves the applicability of the mass reconstruction techniques described at higher instan-

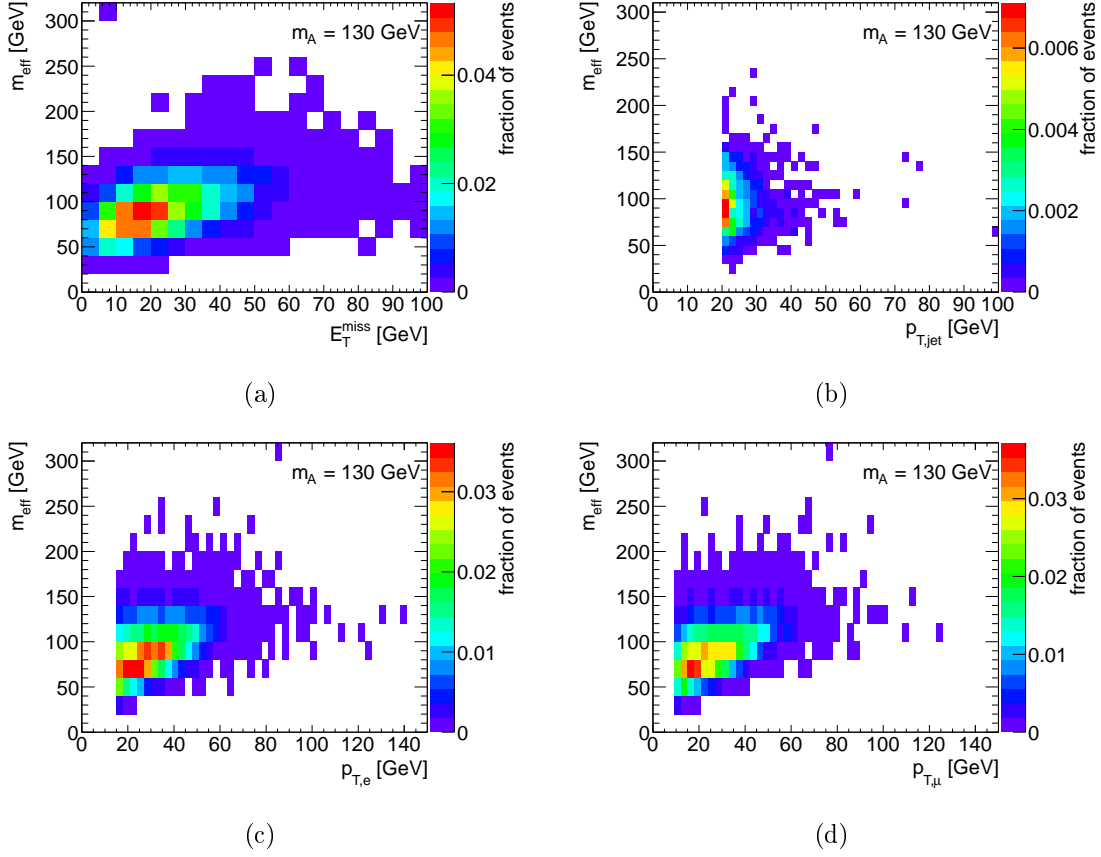


Figure 6.5: Dependency of the effective mass, m_{eff} , on the (a) missing transverse energy, (b) the transverse momentum of the leading jet and the transverse momentum of the (c) electron and the (d) muon for a MSSM Higgs boson with a mass of $m_A = 130$ GeV.

taneous luminosities without limitations.

In figure 6.5 the dependence of the effective mass on the variables mentioned is illustrated. Exemplarily, the distributions at the Higgs boson mass point of $m_A = 130$ GeV are shown. This mass point is chosen explicitly as the newly discovered boson at the LHC is measured to have a mass of $m \approx 126$ GeV [2]. Figure 6.6 and 6.7 represent the dependence of all afore defined mass reconstruction techniques in profile histograms. They are constructed from the two-dimensional distributions by averaging the mass spread along the y -axis for every bin on the x -axis. With this, one-dimensional distributions are obtained. Depicted is the dependence for the signal process with $m_A = 130$ GeV as well as for the background sources $Z^0/\gamma^* \rightarrow \tau^+\tau^-$ and $t\bar{t}$. The dependence at other mass points in the range $90 \text{ GeV} \leq m_A \leq 200 \text{ GeV}$ is similar and depicted in figures B.1 to B.4 in the appendix.

- **Missing transverse energy:** From figures 6.5(a) and 6.6(a) it can be seen that all mass reconstruction techniques show a linear dependence on the miss-

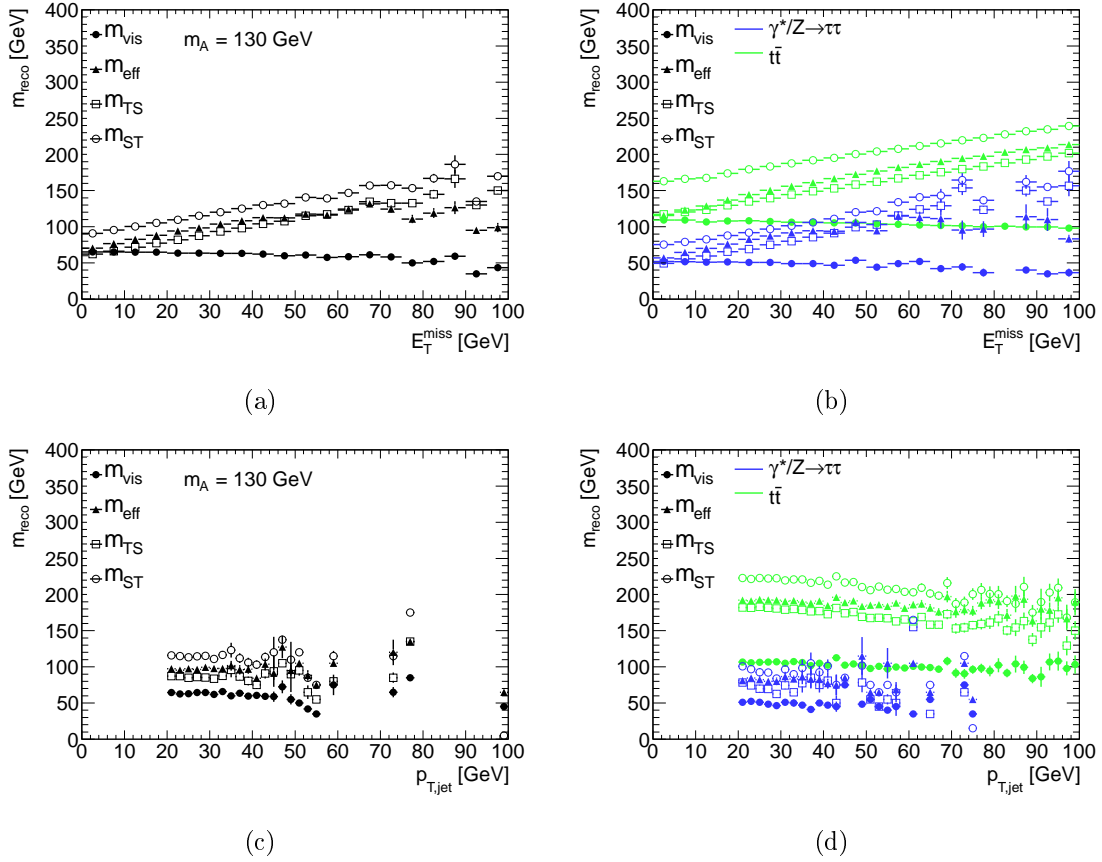


Figure 6.6: Dependency of different mass reconstruction techniques on the missing transverse energy (a) for a MSSM Higgs boson with a mass of $m_A = 130$ GeV (compare [97], figure 4.2) and (b) for the background sources $Z^0/\gamma^* \rightarrow \tau^+\tau^-$ and $t\bar{t}$. The dependency on the transverse momentum of the leading jet is depicted in figure (c) for the signal (compare [97], figure 4.3) and (d) for the background sources.

ing transverse energy. For the visible mass this is linearly decreasing, as described above. In contrast, the decrease is much smaller than expected. This suggests that the missing transverse energy implies a large uncertainty. The dependency of the effective mass is linearly increasing up to a value of $E_T^{\text{miss}} \approx 65$ GeV. For higher values a transition to a plateau can be seen. The value of the plateau is at mass value of $m_{\text{eff}} \approx 120$ GeV. The appropriate distributions for other mass points can be found in the appendix, figure B.1. For lower mass points $90 \text{ GeV} \leq m_A \leq 110$ GeV the plateau is already reached at $E_T^{\text{miss}} \approx 60$ GeV and its value reflects the generated mass. For higher mass points the beginning of the plateau is reached at higher values of E_T^{miss} and its value underestimates the generated mass. The early and late projected mass show a similar behaviour like the effective mass. Both have a linearly increasing dependency on the missing transverse energy with a transition to

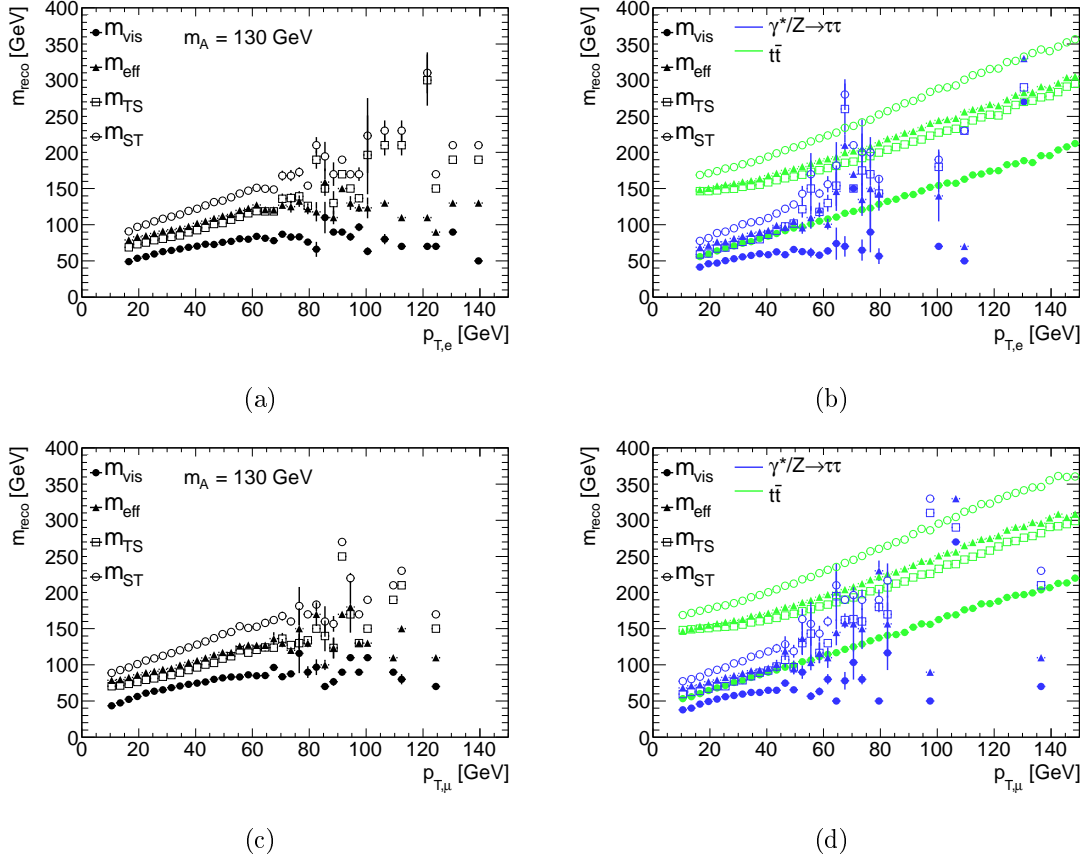


Figure 6.7: Dependency of different mass reconstruction techniques on the transverse momentum of the electron (a) for a MSSM Higgs boson with a mass of $m_A = 130$ GeV and (b) for the background sources $Z^0/\gamma^* \rightarrow \tau^+\tau^-$ and $t\bar{t}$. The dependency on the transverse momentum of the muon is depicted in figure (c) for the signal and (d) for the background sources.

a plateau for higher values of E_T^{miss} . For the early projected transverse mass, m_{TS} , the plateau starts at values of $E_T^{\text{miss}} \approx 80$ GeV; for the late projected transverse mass the plateau is reached already at $E_T^{\text{miss}} \approx 60$ GeV.

The same dependency is observed in reference [97] for a MSSM Higgs boson with a mass of $m_A = 120$ GeV.

- **Transverse momentum of leading jet:** As can be seen from figure 6.6(c) the reconstructed mass of all techniques described is not dependent on the transverse momentum of the leading jet. This is different from the expectation. For the b -quark associated Higgs boson production, jets induced from b -quarks in the final state balance the transverse momentum of the Higgs boson. With a transverse momentum being considerably larger than zero, the value of the measured missing transverse momentum rises, yielding different values for the reconstructed mass. However, with the conditions present at the

peak luminosities at the LHC it is not given that the leading jet is necessarily the b -quark induced jet but may also come from pile-up². Consequently, a particular dependency can not be predicted.

This is in contrast to the conclusion of reference [97], where a dependency on the p_T of the leading jet is observed. Further examination revealed that the implementation into computer code was slightly incorrect in reference [97], resulting in a different behaviour.

- **Transverse momentum of electron:** All mass reconstruction techniques show a linearly increasing dependency on the transverse momentum of the electron. Whereas for the visible mass this increasing dependency is small, evolving into a plateau at low values, it is steep for the late projected transverse mass. The latter mentioned does not form a plateau. The effective mass and the early projected transverse mass, on the other hand, do evolve into a plateau. The beginning is dependent on the selected mass point m_A as can be seen from figure B.3.

Again, this behaviour can be explained through the usage of the missing transverse energy which reflects the energy of the neutrinos inadequately.

- **Transverse momentum of muon:** The dependency on the transverse momentum of the muon is very similar to that from the electron. Only the late projected transverse mass behaves differently, by exhibiting a less steep dependence.

Comparing the left and the right column of figures 6.6 and 6.7 it is obvious that the variable dependence for the signal process and the background processes are similar. They reflect no dependence on the transverse momentum of the leading jet and a linear dependency on the other variables discussed. However, the offset and the slope of the linear functions are different.

6.6.2 Elimination of variable dependence

Beyond the examinations of reference [97] this study investigates a possible elimination of the variable dependence.

A dependence of the reconstructed mass on different event variables depending on the technique used indicates that the reconstruction technique is not robust. For this analysis, the largest effect comes from the use of the missing transverse energy, which obviously does not reflect the energy of the neutrinos present in the final state. Nevertheless, E_T^{miss} is the only variable with which the energy of particles leaving the detector undetected can be estimated. The dependence on event variables leads to the fact that the mass reconstruction methods result in mass distributions with a larger width. The broader the mass distributions, the less accurate will be the mass determination. The natural width of the MSSM Higgs bosons is of the order $\sim \text{GeV}$ [101], while the width of the mass distributions

²With pile-up multiple proton-proton interactions per bunch crossing are denoted (section 4.3).

is of the order ~ 30 GeV. An elimination of the variable dependency cannot compensate the deficit of the missing energy measurement, but will help to measure the mass with a higher accuracy. Regarding the challenges of the Higgs boson mass measurement, it is obvious that the natural width of the mass distribution is a minor factor. Instead, section 6.5 reveals that the separation of the signal process from background processes is most important.

This section examines whether an elimination of the dependency on the missing transverse energy and the transverse momentum of the leptons will improve the separation power by decreasing the width of the mass distributions. The elimination is realised by fitting the profile histograms as illustrated in figure 6.6 and 6.7 with a linear function $f(x)$ for each mass point:

$$f(x) = a_i \cdot x + b_i + m_i. \quad (6.12)$$

The variable m_i corresponds to the mass, m_A , the Higgs boson sample is generated with. For this analysis, the mass points $m_A = \{90, 110, 130, 150, 170, 200\}$ are chosen. The index i runs over the number of mass points, $i = 1, \dots, 6$. The fit functions for the given mass points are derived for each mass reconstruction method, separately. The fit itself is conducted using a χ^2 -test [102]. For the minimisation of the fit the **TMinuit2** package [103] is used. Since in the range of $[20, 60]$ GeV the dependency shows a linear behaviour on the variables E_T^{miss} , $p_{T,e}$ and $p_{T,\mu}$ the fit is restricted to this range.

To derive a fit function being valid for the whole mass range, $m_A = [90, \dots, 200]$, the mean of the fit parameters, $\langle a \rangle$ and $\langle b \rangle$, is determined via:

$$\langle a \rangle = \sum_{i=1}^6 a_i / \Delta_{a,i}^2 \cdot \left(\sum_{i=1}^6 \frac{1}{\Delta_{a,i}^2} \right)^{-1} \quad \Delta \langle a \rangle = \sqrt{\frac{1}{\sum_{i=1}^6 1/\Delta_{a,i}^2}} \quad (6.13)$$

$$\langle b \rangle = \sum_{i=1}^6 b_i / \Delta_{b,i}^2 \cdot \left(\sum_{i=1}^6 \frac{1}{\Delta_{b,i}^2} \right)^{-1} \quad \Delta \langle b \rangle = \sqrt{\frac{1}{\sum_{i=1}^6 1/\Delta_{b,i}^2}} \quad (6.14)$$

Here, $\Delta_{a,i}$ and $\Delta_{b,i}$ are the uncertainties on the fit parameters, whereas $\Delta \langle a \rangle$ and $\Delta \langle b \rangle$ are the uncertainties on the mean. The values derived are given in table B.1 in the appendix. With this, a fit function valid for the whole mass range is established:

$$g(x) = \langle a \rangle \cdot x + \langle b \rangle. \quad (6.15)$$

This procedure is applied to the mass reconstruction methods of the visible mass, the effective mass and the early and late projected transverse mass with respect to the variables $x \in \{E_T^{\text{miss}}, p_{T,e}, p_{T,\mu}\}$. An elimination of the variable dependence is achieved by applying an event-by-event correction of the mass calculated, m_{reco} , through:

$$m_{\text{corr}} = m_{\text{reco}} - g(x). \quad (6.16)$$

Figure 6.8 represents the mass distributions for the visible mass, the effective mass, the early and the late projected transverse mass after the elimination of the variable

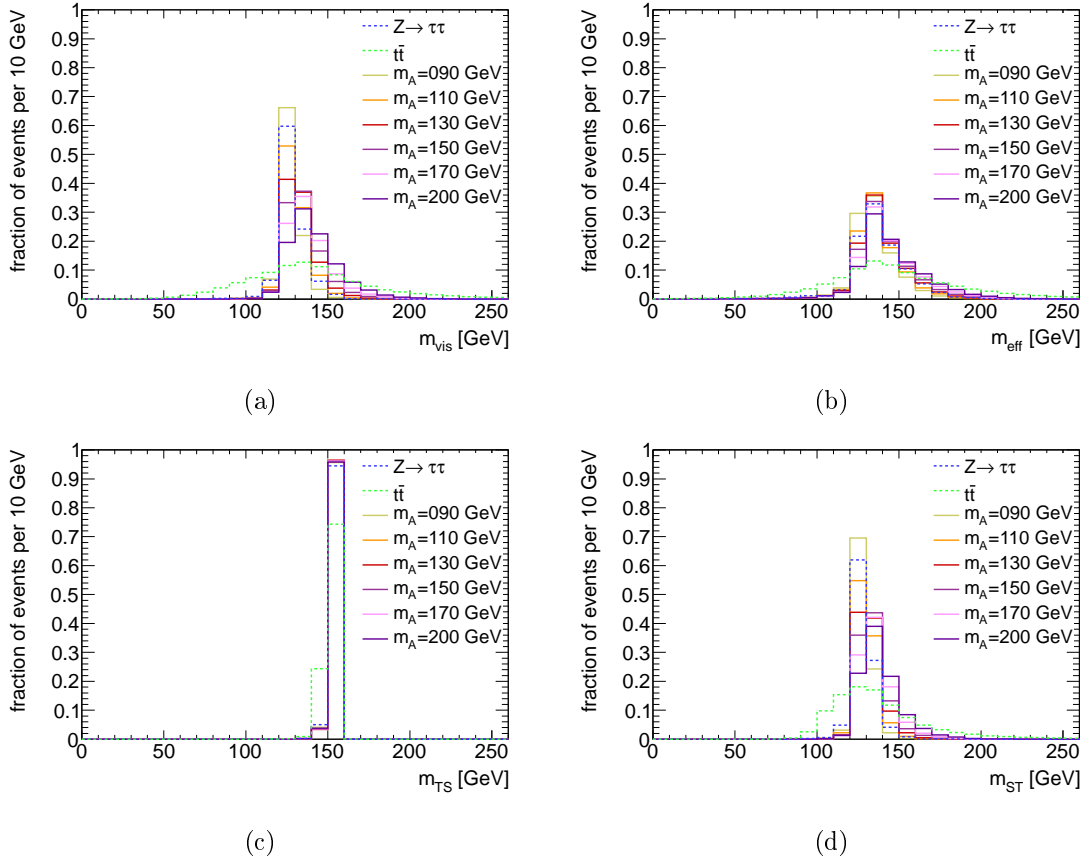


Figure 6.8: Distribution of the (a) visible mass, (b) the effective mass, (c) the early projected and (d) the late projected transverse mass after the elimination of the variable dependencies on the missing transverse energy and the transverse momentum of the electron and the muon.

dependencies. The result on the relative standard deviation of the distributions and the background separation power is quantified in table 6.3. The width of the distributions has decreased, as expected. For the visible, the effective and the late projected transverse mass it is reduced by a factor of approximately three, while for the early projected transverse mass a reduction of even 20 is achieved. However, the mean of the reconstructed mass is shifted towards a central value for all mass points analysed as well as for the background processes, $Z^0/\gamma^* \rightarrow \tau^+\tau^-$ and $t\bar{t}$. For all mass reconstruction techniques the mean yielded is located in the range $[125, 155]$ GeV, independent of the signal or background process. As a consequence, the separation power is not improved through the variable elimination. Furthermore, the mean of the reconstructed mass between different generated masses is less distinct. A mass calibration might be able to disentangle the reconstructed masses. However, the mass determination of observed Higgs boson events becomes very sensitive to small variations from uncertainties on the input variables. The evolution of the relative width and the separation power after the elimination

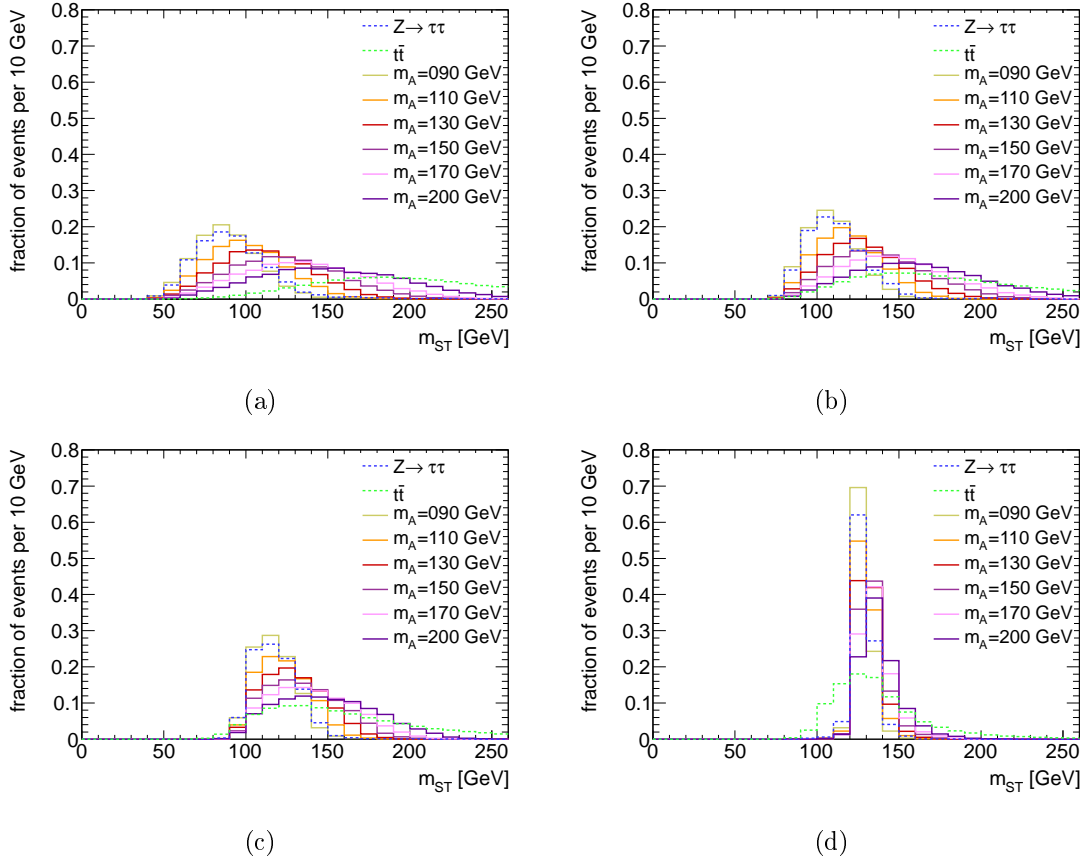


Figure 6.9: Evolution of the late projected transverse mass during the process of the dependency elimination; (a) original distribution and after the elimination of the (b) missing transverse energy dependency, (c) the dependency on the transverse momentum of the electron and (d) the transverse momentum of the muon.

of the variable dependence on the missing transverse energy and the transverse momentum of the electron can be found in tables B.2 and B.3, respectively. The evolution of the mass distribution after each step of the dependency elimination is given in figure 6.9 on the basis of the late projected transverse mass.

In summary, the elimination of the dependence of the reconstructed mass value on the missing transverse momentum, the transverse momentum of the electron and the muon does not lead to a better separation power between signal and background processes. It rather corrupts the signal selection and the mass determination and is therefore not used for the calibration of section 6.7.

Table 6.3: Quantitative mass reconstruction comparison for selected Higgs boson mass points after the dependency elimination of the transverse momentum of the muon. The statistical uncertainty on σ_{rel} can be neglected.

	mean (GeV)	bias (GeV)	σ_{rel}	$\Sigma_{Z \rightarrow \tau\tau}$	$\Sigma_{t\bar{t}}$
m_{vis}					
$m_A = 90.00$ GeV	127.00 ± 0.08	37.00 ± 0.08	0.06	1.00	1.12
$m_A = 130.00$ GeV	132.65 ± 0.09	2.65 ± 0.09	0.07	1.01	1.16
$m_A = 200.00$ GeV	141.69 ± 0.13	-58.31 ± 0.13	0.11	2.14	1.17
m_{eff}					
$m_A = 90.00$ GeV	134.52 ± 0.18	44.52 ± 0.18	0.12	1.00	1.06
$m_A = 130.00$ GeV	139.06 ± 0.16	9.06 ± 0.16	0.12	1.00	1.11
$m_A = 200.00$ GeV	145.55 ± 0.18	-54.45 ± 0.18	0.15	1.00	1.08
m_{TS}					
$m_A = 90.00$ GeV	154.80 ± 0.03	64.80 ± 0.03	0.02	1.00	1.11
$m_A = 130.00$ GeV	154.80 ± 0.02	24.80 ± 0.02	0.01	1.00	1.12
$m_A = 200.00$ GeV	154.58 ± 0.02	-45.42 ± 0.02	0.02	1.00	1.11
m_{ST}					
$m_A = 90.00$ GeV	127.83 ± 0.06	37.83 ± 0.06	0.04	1.00	1.23
$m_A = 130.00$ GeV	131.99 ± 0.07	1.99 ± 0.07	0.06	1.01	1.16
$m_A = 200.00$ GeV	138.63 ± 0.10	-61.37 ± 0.10	0.09	1.63	1.16

6.7 Calibration

As discussed in section 6.5 the mass reconstruction techniques examined yield a bias with respect to the generated mass. With this, a direct mass determination from observed Higgs boson events is not possible. However, this is irrelevant if it is possible to calibrate the reconstructed masses to the generated mass of the Higgs boson samples. Reference [97] presented that a calibration of the reconstructed mass is possible. In figure 6.10 the reconstructed mass is depicted with respect to the generated mass, m_{gen} , showing a linear behaviour on the latter. Here, the reconstructed mass is described by the mean of the mass distribution. Given the standard deviation of approximately 20%-30% of the mean (table 6.2), an event-by-event calibration is not sensible. It rather can be applied to the mass value which is determined from a mass distribution of an ensemble of selected Higgs boson events. A calibration can be achieved by fitting the mass dependency with a straight line:

$$f(m_{gen}) = a \cdot m_{gen} + b. \quad (6.17)$$

The fit is conducted using a χ^2 -minimisation [102]. For the minimisation of the fit the TMinuit2 package of [103] is used. For the mass dependencies the mass points $m_A = \{90, 100, 110, 120, 130, 140, 150, 170, 200\}$ are chosen. The reconstructed mass, m_{reco} , given by the mean of the distribution is then calibrated using:

$$m_{calib} = (m_{reco} - b) \cdot a^{-1}. \quad (6.18)$$

The uncertainty on the reconstructed mass, taken into account in the fit, is given by the uncertainty on the mean of the distribution. It is estimated as the standard deviation of the distribution divided by the square root of the number of entries. Table 6.4 represents the parameters obtained from the fit. The goodness of fit is quantified by the χ^2 of the test divided by the number of degrees of freedom of the fit. Given the values in table 6.4, the fit can be considered as good and therefore proves the possibility of calibrating the mass distributions.

Table 6.4: Fit parameters derived for the calibration by fitting a linear function $f(m_{gen}) = a \cdot m_{gen} + b$ (compare [97], table 5.1). The goodness of fit is quantified by χ^2/ndf , with $ndf = 7$. The statistical uncertainty on the parameter a can be neglected.

	a	b (GeV)	χ^2/ndf
m_{vis}	0.36	16.8 ± 0.2	1.61
m_{eff}	0.49	30.3 ± 0.4	1.00
m_{TS}	0.41	31.5 ± 0.5	1.06
m_{ST}	0.58	37.9 ± 0.4	0.88

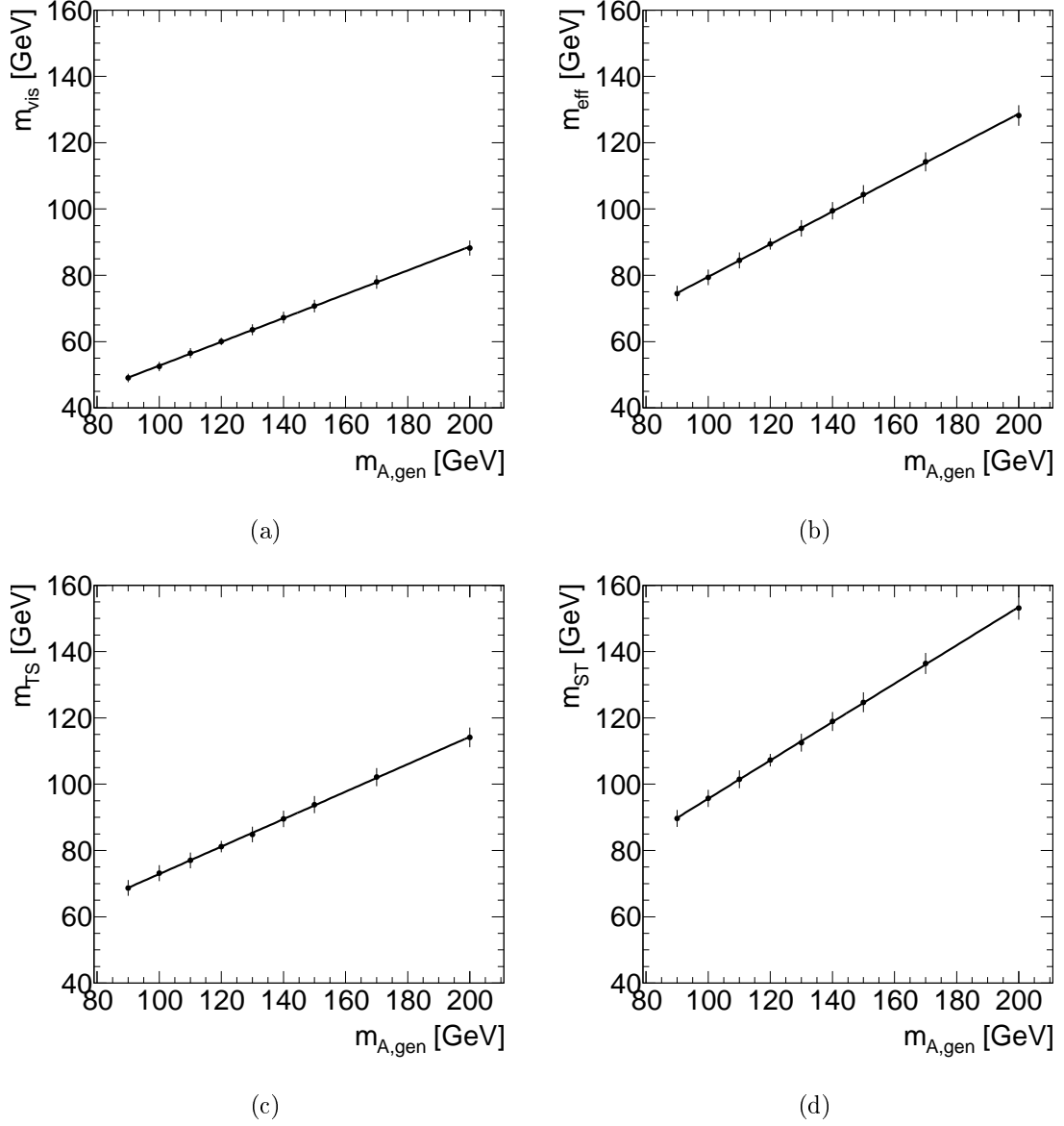


Figure 6.10: Calibration of the reconstructed mass, which is represented by the mean of the mass distribution. Depicted are the (a) visible mass, (b) the effective mass, (c) the early and (d) the late projected transverse mass (compare [97], figure 5.1). For visuality the statistical uncertainty on the reconstructed mass is multiplied by a factor of 10.

6.8 Discussion

Different mass reconstruction methods are compared using the relative standard deviation of the distributions obtained and the separation power with respect to the background sources $Z^0/\gamma^* \rightarrow \tau^+\tau^-$ and $t\bar{t}$. For different mass ranges of the Higgs boson different mass reconstruction techniques deliver the best performance. It is evident that the choice of a certain mass reconstruction technique depends on the mass of the hypothetical Higgs boson.

The analysis of a variable dependence reveals a linear dependence on the missing transverse momentum, as is seen in [97], and the transverse momenta of the electron and the muon. No dependency is observed for the transverse momentum of the leading jet, which is in contrast to reference [97]. An elimination of the variable dependence is achieved by fitting a straight line to the mean of the reconstructed mass as a function of the respective variable. However, the dependency elimination yields reconstructed masses which are shifted to a central value for all, the signal process at different mass points as well as the background sources. One of the reasons that the elimination of the variable dependency gives almost identical mass distributions for different processes or masses is the choice of the variables. The missing transverse energy as well as the transverse momentum of the electron and muon are input variables to the mass reconstruction methods discussed. As signal and background processes have similar decay kinematics, the equal treatment of the variables during the procedure of dependency elimination results in similar results. This effect can be circumvented by eliminating a dependency on variables which are distributed differently for signal and background processes. A possible variable might be the transverse momentum of the leading jet. However, as shown in section 6.6.2 the mass reconstruction methods discussed do not show a dependency on this variable for both, the signal and background processes.

Furthermore, as reflected in table 6.2, the reconstruction techniques yield a bias with respect to the generated mass. Nevertheless, a calibration can be achieved by fitting a straight line to the mean of the reconstructed mass as a function of the generated mass.

A Cross section measurement

A.1 Monte Carlo corrections

Table A.1: Correction factors concerning the electron reconstruction and identification efficiency.

η range	correction factor	p_T range (GeV)	correction factor
$-2.47 \leq \eta < -2.01$	0.905 ± 0.024	$0 \leq p_T < 25$	0.888 ± 0.034
$-2.01 \leq \eta < -1.52$	0.907 ± 0.023	$25 \leq p_T < 35$	0.966 ± 0.014
$-1.52 \leq \eta < -0.8$	0.919 ± 0.015	$35 \leq p_T < 45$	1.008 ± 0.009
$-0.8 \leq \eta < 0.0$	0.970 ± 0.009	$45 \leq p_T < 60$	1.038 ± 0.009
$0.0 \leq \eta < 0.8$	0.965 ± 0.007	$60 \leq p_T < \infty$	1.049 ± 0.011
$0.8 \leq \eta < 1.52$	0.915 ± 0.015		
$1.52 \leq \eta < 2.01$	0.966 ± 0.019		
$2.01 \leq \eta < 2.47$	0.870 ± 0.024		

A.2 Systematic uncertainty of the method for QCD multijet estimation

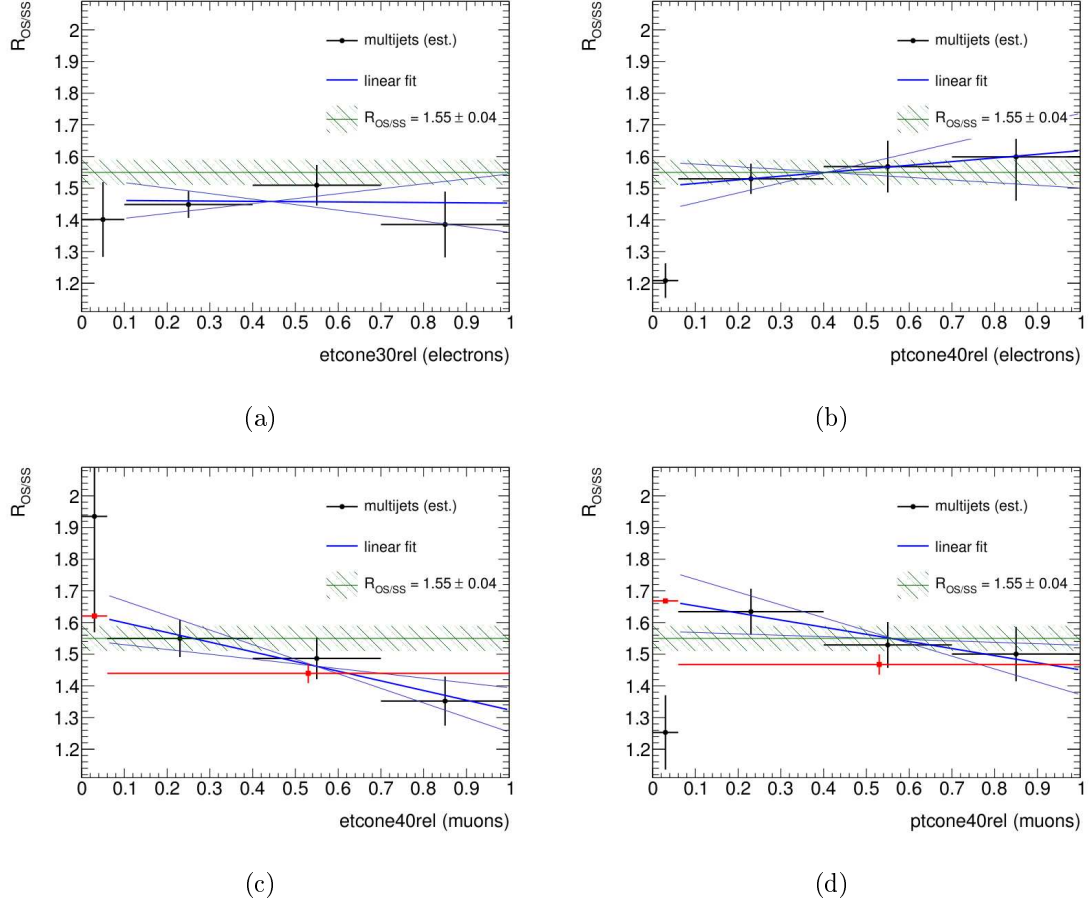


Figure A.1: Distribution of the ratio $R^{OS/SS}$ as a function of the isolation variables of the selected leptons [55]. The last three bins are fitted with a straight linear and extrapolated to the first bin. The red squares in the lower figures mark the results for $R_{ex}^{OS/SS}$ in the first bin and $R'^{OS/SS}$ in the last three bins.

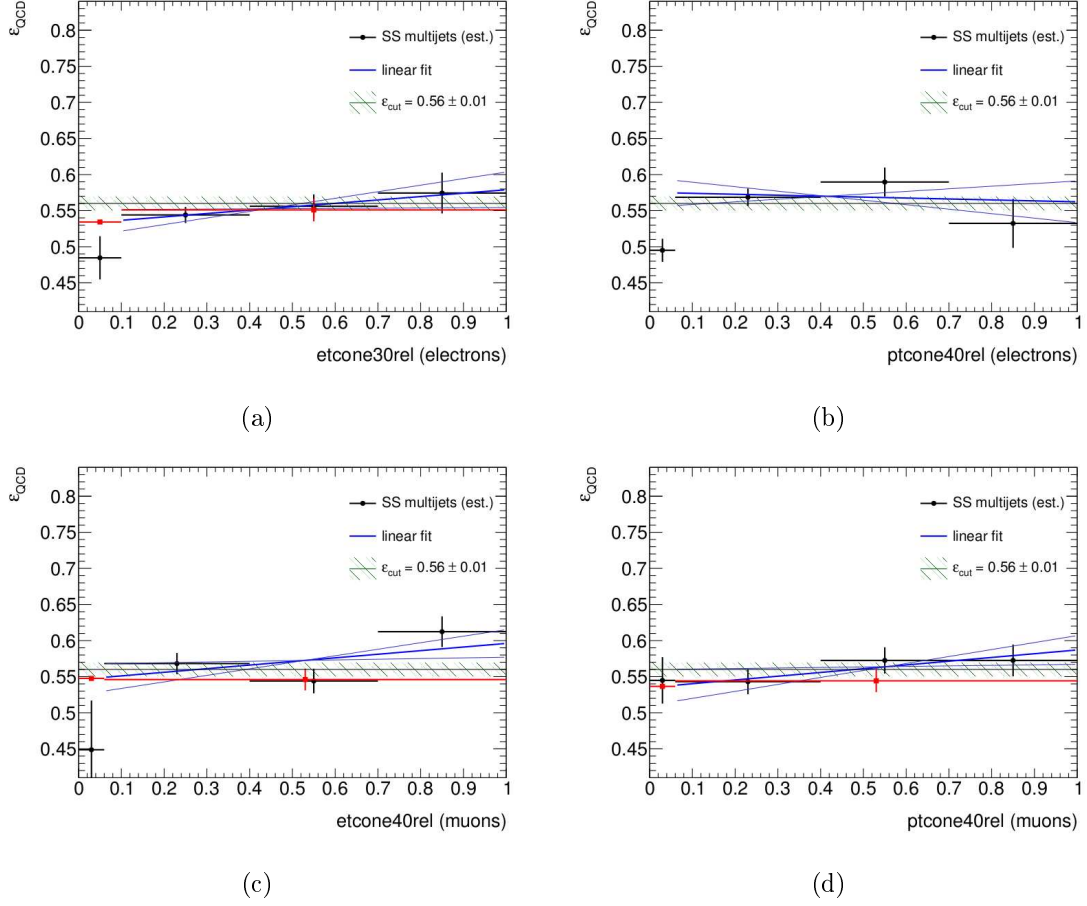


Figure A.2: Distribution of the selection efficiency ϵ_{QCD} as a function of the isolation variables of the selected leptons [55]. The last three bins are fitted with a straight linear and extrapolated to the first bin. If indicated, the red squares mark the results for $\epsilon_{ex,QCD}$ in the first bin and ϵ'_{QCD} in the last three bins.

B Comparison of mass reconstruction techniques

B.1 Dependency on event variables

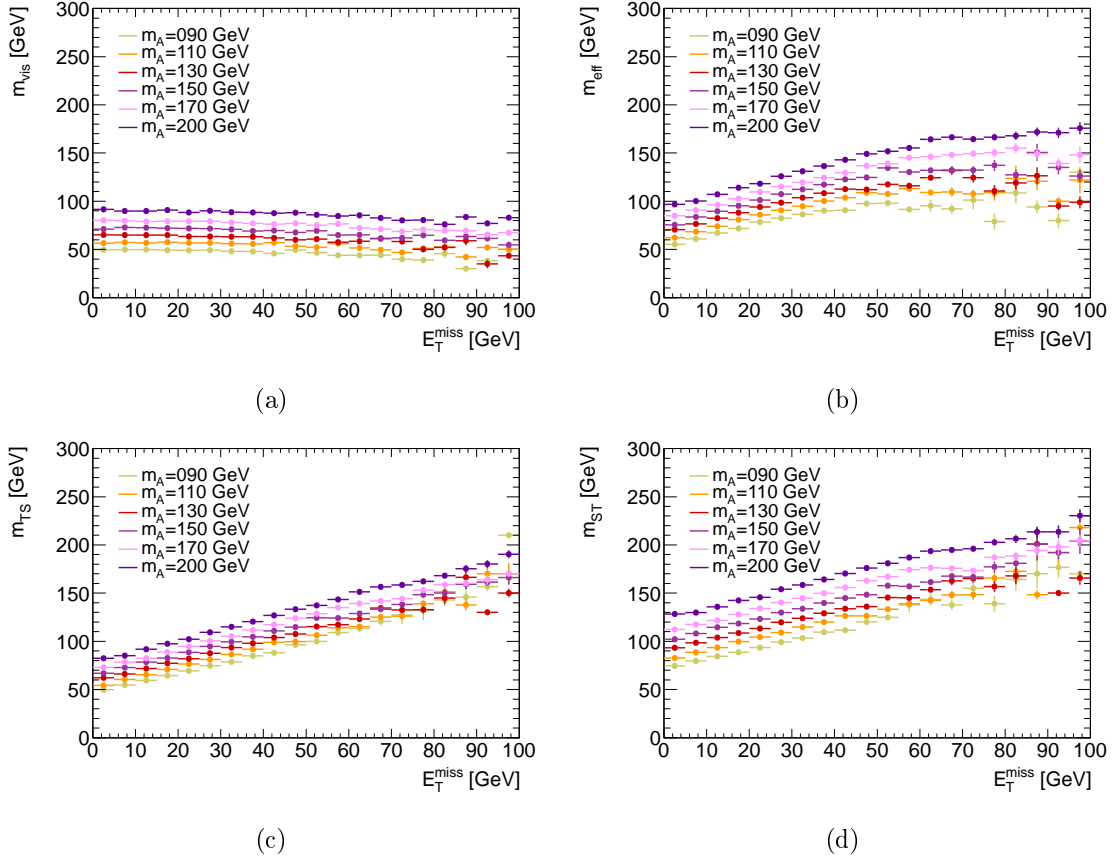


Figure B.1: Dependency of a mass reconstruction technique on the missing transverse energy, E_T^{miss} , for a MSSM Higgs boson in a mass range $90 \text{ GeV} \leq m_A \leq 200 \text{ GeV}$. The dependency is given for the visible mass (a), the effective mass (b), the early (c) and late (d) projected transverse mass.

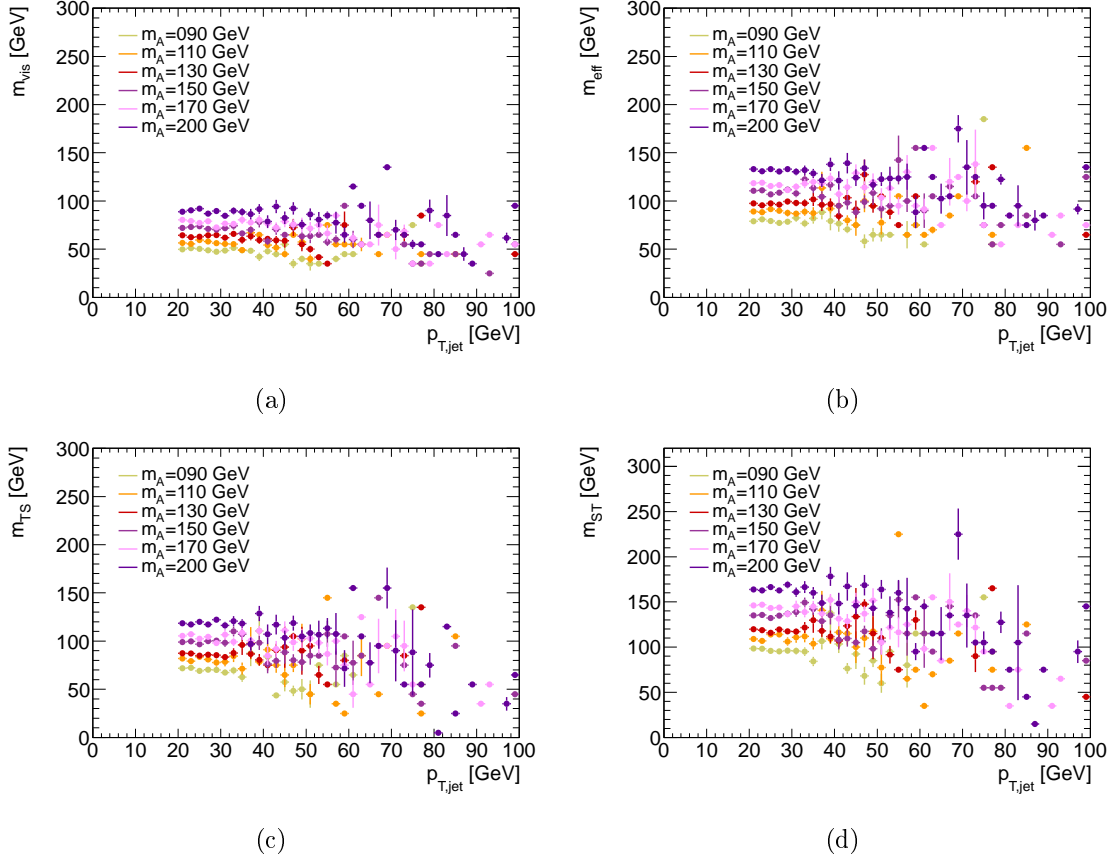


Figure B.2: Dependency of a mass reconstruction technique on the leading jet p_T for a MSSM Higgs boson in a mass range $90 \text{ GeV} \leq m_A \leq 200 \text{ GeV}$. The dependency is given for the visible mass (a), the effective mass (b), the early (c) and late (d) projected transverse mass.

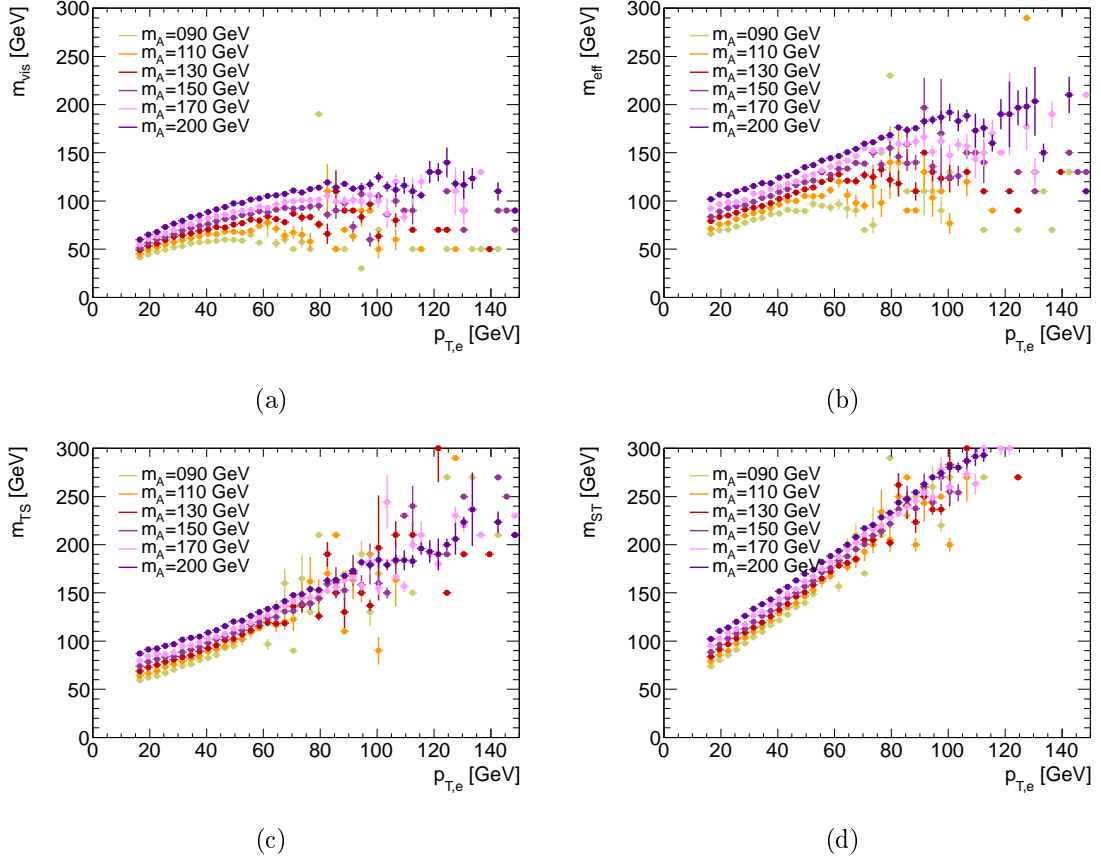


Figure B.3: Dependency of a mass reconstruction technique on the transverse momentum of the selected electron for a MSSM Higgs boson in a mass range $90 \text{ GeV} \leq m_A \leq 200 \text{ GeV}$. The dependency is given for the visible mass (a), the effective mass (b), the early (c) and late (d) projected transverse mass.

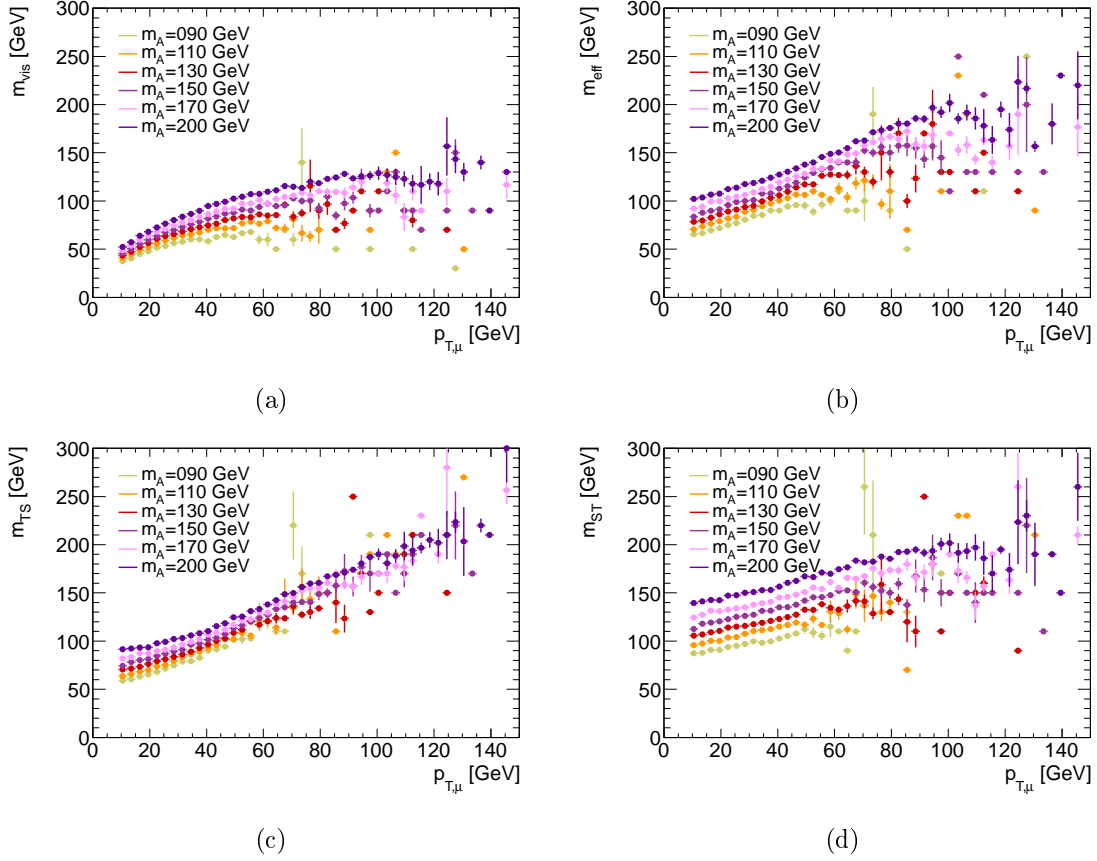


Figure B.4: Dependency of a mass reconstruction technique on the transverse momentum of the selected muon for a MSSM Higgs boson in a mass range $90 \text{ GeV} \leq m_A \leq 200 \text{ GeV}$. The dependency is given for the visible mass (a), the effective mass (b), the early (c) and late (d) projected transverse mass.

B.2 Elimination of variable dependence

Table B.1: Fit parameters derived for the elimination of variable dependence for different mass reconstruction techniques. The variables studied are the missing transverse energy, E_T^{miss} , the transverse momentum of the selected electron, $p_{T,e}$, and the selected muon, $p_{T,\mu}$

	E_T^{miss}		$p_{T,e}$		$p_{T,\mu}$	
	$\langle a \rangle$	$\langle b \rangle$	$\langle a \rangle$	$\langle b \rangle$	$\langle a \rangle$	$\langle b \rangle$
m_{vis}	-0.12 ± 0.01	-62.0 ± 0.3	0.72 ± 0.01	-23.9 ± 0.2	0.77 ± 0.00	-25.1 ± 0.2
m_{eff}	0.89 ± 0.01	-57.7 ± 0.4	0.94 ± 0.01	-32.9 ± 0.3	0.97 ± 0.01	-34.1 ± 0.3
m_{TS}	1.08 ± 0.01	-72.6 ± 0.3	0.99 ± 0.01	-31.1 ± 0.2	0.98 ± 0.00	-53 ± 0
m_{ST}	0.97 ± 0.01	-40.6 ± 0.4	1.21 ± 0.01	-39.1 ± 0.3	1.23 ± 0.00	-37.4 ± 0.1

Table B.2: Quantitative mass reconstruction comparison for selected Higgs boson mass points after the dependency elimination of the missing transverse energy. The statistical uncertainty on σ_{rel} can be neglected.

	mean (GeV)	bias (GeV)	σ_{rel}	$\Sigma_{Z \rightarrow \tau\tau}$	$\Sigma_{t\bar{t}}$
m_{vis}					
$m_A = 90.00$ GeV	113.60 ± 0.13	23.60 ± 0.13	0.10	1.00	1.74
$m_A = 130.00$ GeV	128.56 ± 0.16	-1.44 ± 0.16	0.14	1.38	1.00
$m_A = 200.00$ GeV	154.09 ± 0.23	-45.91 ± 0.23	0.19	5.90	1.02
m_{eff}					
$m_A = 90.00$ GeV	113.24 ± 0.21	23.24 ± 0.21	0.16	1.01	1.88
$m_A = 130.00$ GeV	129.71 ± 0.22	-0.29 ± 0.22	0.18	1.04	1.42
$m_A = 200.00$ GeV	157.35 ± 0.28	-42.65 ± 0.28	0.22	2.56	1.11
m_{TS}					
$m_A = 90.00$ GeV	118.30 ± 0.15	28.30 ± 0.15	0.11	1.00	2.17
$m_A = 130.00$ GeV	130.58 ± 0.17	0.58 ± 0.17	0.14	1.08	1.48
$m_A = 200.00$ GeV	152.15 ± 0.23	-47.85 ± 0.23	0.19	3.16	0.97
m_{ST}					
$m_A = 90.00$ GeV	109.70 ± 0.19	19.70 ± 0.19	0.15	1.00	2.28
$m_A = 130.00$ GeV	129.07 ± 0.23	-0.93 ± 0.23	0.19	1.18	1.45
$m_A = 200.00$ GeV	162.70 ± 0.31	-37.30 ± 0.31	0.24	4.39	0.96

Table B.3: Quantitative mass reconstruction comparison for selected Higgs boson mass points after the dependency elimination of the transverse momentum of the electron. The statistical uncertainty on σ_{rel} can be neglected

	mean (GeV)	bias (GeV)	σ_{rel}	$\Sigma_{Z \rightarrow \tau\tau}$	$\Sigma_{t\bar{t}}$
<i>m_{vis}</i>					
$m_A = 90.00$ GeV	118.78 ± 0.12	28.78 ± 0.12	0.09	1.00	1.05
$m_A = 130.00$ GeV	129.31 ± 0.14	-0.69 ± 0.14	0.12	1.09	1.25
$m_A = 200.00$ GeV	146.72 ± 0.19	-53.28 ± 0.19	0.17	4.55	1.08
<i>m_{eff}</i>					
$m_A = 90.00$ GeV	121.69 ± 0.20	31.69 ± 0.20	0.14	1.00	1.46
$m_A = 130.00$ GeV	132.39 ± 0.20	2.39 ± 0.20	0.16	1.00	1.25
$m_A = 200.00$ GeV	149.42 ± 0.24	-50.58 ± 0.24	0.20	1.70	1.08
<i>m_{TS}</i>					
$m_A = 90.00$ GeV	123.68 ± 0.11	33.68 ± 0.11	0.07	1.00	1.41
$m_A = 130.00$ GeV	129.88 ± 0.13	-0.12 ± 0.13	0.10	1.00	1.19
$m_A = 200.00$ GeV	140.29 ± 0.16	-59.71 ± 0.16	0.150	2.41	1.00
<i>m_{ST}</i>					
$m_A = 90.00$ GeV	117.37 ± 0.15	27.37 ± 0.15	0.11	1.00	1.52
$m_A = 130.00$ GeV	129.32 ± 0.18	-0.68 ± 0.18	0.15	1.00	1.00
$m_A = 200.00$ GeV	149.30 ± 0.24	-50.70 ± 0.24	0.20	3.76	0.97

Bibliography

- [1] CMS Collaboration, S. Chatrchyan et al., *Observation of a new boson at a mass of 125 GeV with the CMS experiment at the LHC*, Physics Letters B **716** (2012) 30–61, [arXiv:1207.7235 \[hep-ex\]](#).
- [2] ATLAS Collaboration, G. Aad et al., *Observation of a new particle in the search for the Standard Model Higgs boson with the ATLAS detector at the LHC*, Physics Letters B **716** (2012) 1–29, [arXiv:1207.7214 \[hep-ex\]](#).
- [3] ATLAS Collaboration, G. Aad et al., *A Particle Consistent with the Higgs Boson Observed with the ATLAS Detector at the Large Hadron Collider*, Science **338** (2012) no. 6114, 1576–1582.
- [4] CMS Collaboration, S. Chatrchyan et al., *A New Boson with a Mass of 125 GeV Observed with the CMS Experiment at the Large Hadron Collider*, Science **338** (2012) no. 6114, 1569–1575.
- [5] J. Beringer et al (Particle Data Group), *The Review of Particle Physics*, Physical Review D **86** (2012) 010001.
- [6] M. Gonzalez-Garcia and Y. Nir, *Neutrino masses and mixing: Evidence and implications*, Review of Modern Physics **75** (2003) 345–402, [arXiv:hep-ph/0202058 \[hep-ph\]](#).
- [7] O. Eberhardt, G. Herbert, H. Lacker, A. Lenz, A. Menzel, et al., *Joint analysis of Higgs decays and electroweak precision observables in the Standard Model with a sequential fourth generation*, Physical Review D **86** (2012) 013011, [arXiv:1204.3872 \[hep-ph\]](#).
- [8] CMS Collaboration, S. Chatrchyan et al., *Combined search for the quarks of a sequential fourth generation*, [arXiv:1209.1062 \[hep-ex\]](#).
- [9] P. W. Higgs, *Spontaneous Symmetry Breakdown without Massless Bosons*, Physical Review **145** (1966) 1156–1163.
- [10] P. W. Higgs, *Broken Symmetries and the Masses of Gauge Bosons*, Physical Review Letters **13** (1964) 508–509.
- [11] F. Englert and R. Brout, *Broken Symmetry and the Mass of Gauge Vector Mesons*, Physical Review Letters **13** (1964) 321–323.

- [12] G. Guralnik, C. Hagen, and T. Kibble, *Global Conservation Laws and Massless Particles*, Physical Review Letters **13** (1964) 585–587.
- [13] M. S. Carena, S. Heinemeyer, C. Wagner, and G. Weiglein, *Suggestions for benchmark scenarios for MSSM Higgs boson searches at hadron colliders*, Eur.Phys.J. **C26** (2003) 601–607, [arXiv:hep-ph/0202167](#).
- [14] M. Gomez-Bock, M. Mondragon, M. Muhlleitner, M. Spira, and P. Zerwas, *Concepts of Electroweak Symmetry Breaking and Higgs Physics*, [arXiv:0712.2419 \[hep-ph\]](#).
- [15] S. Myers, *The LEP Collider, from design to approval and commissioning.*, Tech. Rep. CERN-91-08, Geneva, 1991.
- [16] S. Holmes, R. S. Moore, and V. Shiltsev, *Overview of the Tevatron Collider Complex: Goals, Operations and Performance*, JINST **6** (2011) T08001, [arXiv:1106.0909 \[physics.acc-ph\]](#).
- [17] ALEPH, CDF, D0, DELPHI, L3, OPAL, SLD Collaborations, LEP Electroweak Working Group, Tevatron Electroweak Working Group, SLD Electroweak and Heavy Flavour Groups, *Precision Electroweak Measurements and Constraints on the Standard Model*, [arXiv:1012.2367 \[hep-ex\]](#).
- [18] LEP Working Group for Higgs boson searches, ALEPH Collaboration, DELPHI Collaboration, L3 Collaboration, OPAL Collaboration, *Search for the standard model Higgs boson at LEP*, Phys.Lett. **B565** (2003) 61–75, [arXiv:hep-ex/0306033 \[hep-ex\]](#).
- [19] CDF and D0 Collaborations and the Tevatron New Physics and Higgs Working Group, *Updated Combination of CDF and D0 Searches for Standard Model Higgs Boson Production with up to 10.0 fb⁻¹ of Data*, [arXiv:1207.0449 \[hep-ex\]](#).
- [20] CDF, D0 Collaboration, T. Aaltonen et al., *Evidence for a particle produced in association with weak bosons and decaying to a bottom-antibottom quark pair in Higgs boson searches at the Tevatron*, Physical Review Letters **109** (2012) 071804, [arXiv:1207.6436 \[hep-ex\]](#).
- [21] T. Gleisberg, S. Hoeche, F. Krauss, M. Schonherr, S. Schumann, et al., *Event generation with SHERPA 1.1*, JHEP **0902** (2009) 007, [arXiv:0811.4622 \[hep-ph\]](#).
- [22] T. Sjöstrand, S. Mrenna and P. Skands, *PYTHIA 6.4 physics and manual*, JHEP **05** (2006) 026, [arXiv:hep-ph/0603175](#).
- [23] S. Catani, F. Krauss, R. Kuhn, and B. Webber, *QCD matrix elements + parton showers*, JHEP **0111** (2001) 063, [arXiv:hep-ph/0109231 \[hep-ph\]](#).

-
- [24] B. Andersson, G. Gustafson, G. Ingelman and T. Sjöstrand, *Parton Fragmentation and String Dynamics*, Physics Reports **97** (1983) 31–145.
- [25] B. Andersson, *The Lund model*, Camb.Monogr.Part.Phys.Nucl.Phys.Cosmol. **7** (1997) 1–471.
- [26] T. D. Gottschalk, *A Realistic Model for $e^+ e^-$ Annihilation Including Parton Bremsstrahlung Effects*, Nuclear Physics B **214** (1983) 201.
- [27] J.-C. Winter, F. Krauss, and G. Soff, *A Modified cluster hadronization model*, European Physical Journal C **36** (2004) 381–395, [arXiv:hep-ph/0311085](#) [hep-ph].
- [28] ATLAS Collaboration, G. Aad et al., *The ATLAS Simulation Infrastructure*, European Physical Journal C **70** (2010) 823–874, [arXiv:1005.4568](#) [physics.ins-det].
- [29] The GEANT4 Collaboration, S. Agostinelli et al., *GEANT4: A simulation toolkit*, Nuclear Instruments and Methods in Physics Research Section A **506** (2003) 250.
- [30] J. Allison, K. Amako, J. Apostolakis, H. Araujo, P. Dubois, et al., *GEANT4 developments and applications*, IEEE Transactions on Nuclear Science **53** (2006) 270.
- [31] L. Evans and P. Bryant, *LHC Machine*, JINST **3** (2008) S08001.
- [32] O. S. Brüning, P. Collier, P. Lebrun, S. Myers, R. Ostojic, J. Poole, P. Proudlock, *LHC Design Report v.1 : the LHC Main Ring, v.2 : the LHC Infrastructure and General Services, v.3 : the LHC Injector Chain*, Tech. Rep. CERN-2004-003-V-1, CERN-2004-003-V-2, CERN-2004-003-V-3, CERN, Geneva, 2004.
- [33] *Summary of the analysis of the 19 September 2008 incident at the LHC*, <https://cdsweb.cern.ch/record/1135729>, Oct, 2008.
- [34] P. Lebrun, *Commissioning and First Operation of the Large Hadron Collider (LHC)*, Tech. Rep. CERN-ATS-2010-178, CERN, Geneva, Aug, 2010.
- [35] ATLAS Collaboration, G. Aad et al., *The ATLAS Experiment at the CERN Large Hadron Collider*, JINST **3** (2008) S08003.
- [36] CMS Collaboration, S. Chatrchyan et al., *The CMS experiment at the CERN LHC*, JINST **3** (2008) S08004.
- [37] ALICE Collaboration, K. Aamodt et al., *The ALICE experiment at the CERN LHC*, JINST **3** (2008) S08002.

- [38] LHCb Collaboration, J. Alves, A. Augusto et al., *The LHCb Detector at the LHC*, JINST **3** (2008) S08005.
- [39] C. Lefevre, *The CERN accelerator complex*, Dec, 2008.
- [40] ATLAS Collaboration, G. Aad et al., *Expected Performance of the ATLAS Experiment - Detector, Trigger and Physics*, arXiv:0901.0512 [hep-ex].
- [41] ATLAS Collaboration, *Luminosity Results*, 2010.
- [42] ATLAS Collaboration, G. Aad et al., *The ATLAS Inner Detector commissioning and calibration*, European Physical Journal C **70** (2010) 787–821, arXiv:1004.5293 [physics.ins-det].
- [43] Atlas Collaboration, G. Aad et al., *Performance of the ATLAS Trigger System in 2010*, European Physical Journal C **72** (2012) 1849, arXiv:1110.1530 [hep-ex].
- [44] ATLAS Collaboration, G. Aad et al., *Luminosity Determination in pp Collisions at $\sqrt{s} = 7$ TeV Using the ATLAS Detector at the LHC*, European Physical Journal C **71** (2011) 1630, arXiv:1101.2185 [hep-ex].
- [45] ATLAS Collaboration, G. Aad et al., *Expected electron performance in the ATLAS experiment*, Tech. Rep. ATL-PHYS-PUB-2011-006, CERN, Geneva, Apr, 2011.
- [46] ATLAS Collaboration, G. Aad et al., *Performance of the Reconstruction and Identification of Hadronic Tau Decays with ATLAS*, Tech. Rep. ATLAS-CONF-2011-152, CERN, Geneva, Nov, 2011.
- [47] M. Cacciari, G. P. Salam, and G. Soyez, *The Anti- k_t jet clustering algorithm*, JHEP **0804** (2008) 063, arXiv:0802.1189 [hep-ph].
- [48] W. Lampl, S. Laplace, D. Lelas, P. Loch, H. Ma, S. Menke, S. Rajagopalan, D. Rousseau, S. Snyder, and G. Unal, *Calorimeter Clustering Algorithms: Description and Performance*, Tech. Rep. ATL-LARG-PUB-2008-002. ATL-COM-LARG-2008-003, CERN, Geneva, Apr, 2008.
- [49] ATLAS Collaboration, G. Aad et al., *Readiness of the ATLAS liquid argon calorimeter for LHC collisions*, European Physical Journal C **70** (2010) , arXiv:0912.2642 [physics.ins-det].
- [50] ATLAS Collaboration, G. Aad et al., *Readiness of the ATLAS Tile calorimeter for LHC collisions*, European Physical Journal C **70** (2010) , arXiv:1007.5423 [physics.ins-det].
- [51] ATLAS Collaboration, G. Aad et al., *Jet energy measurement with the ATLAS detector in proton-proton collisions at $\sqrt{s} = 7$ TeV.*, Tech. Rep. CERN-PH-EP-2011-191, CERN, Geneva, Dec, 2011. arXiv:1112.6426 [hep-ex].

-
- [52] ATLAS Collaboration Collaboration, G. Aad et al., *Performance of Missing Transverse Momentum Reconstruction in Proton-Proton Collisions at 7 TeV with ATLAS*, European Physical Journal C **72** (2012) 1844, [arXiv:1108.5602 \[hep-ex\]](#).
 - [53] J. Kubar, M. L. Bellac, J. Meunier, and G. Plaut, *QCD corrections to the Drell-Yan mechanism and the pion structure function*, Nuclear Physics B **175** (1980) no. 2, 251 – 275.
 - [54] C. Anastasiou, L. Dixon, K. Melnikov, and F. Petriello, *High-precision QCD at hadron colliders: Electroweak gauge boson rapidity distributions at NNLO*, Physical Review D **69** (2004) 094008, [arXiv:hep-ph/0312266](#).
 - [55] ATLAS Collaboration, G. Aad et al., *Measurement of the $Z \rightarrow \tau\tau$ Cross Section with the ATLAS Detector*, Physical Review D **84** (2011) 112006, [arXiv:1108.2016 \[hep-ex\]](#).
 - [56] C. Gumpert, *Measurement of the Cross Section for the Process $pp \rightarrow \gamma^*/Z \rightarrow \tau^+\tau^-$ and a Search for Neutral MSSM Higgs Bosons with the ATLAS Detector*, diploma thesis, TU Dresden, 2011. CERN-THESIS-2011-200.
 - [57] S. Dittmaier, C. Mariotti, G. Passarino, R. Tanaka, et al., *Handbook of LHC Higgs Cross Sections: 2. Differential Distributions*, [arXiv:1201.3084 \[hep-ph\]](#). Report of the LHC Higgs Cross Section Working Group.
 - [58] ATLAS Collaboration, G. Aad et al., *Search for Neutral MSSM Higgs bosons in $\sqrt{s} = 7$ TeV pp collisions at ATLAS*, Tech. Rep. ATLAS-CONF-2012-094, CERN, Geneva, Jul, 2012.
 - [59] J. Butterworth, E. Dobson, U. Klein, B. Mellado Garcia, T. Nunnemann, J. Qian, D. Rebuzzi, and R. Tanaka, *Single Boson and Diboson Production Cross Sections in pp Collisions at $\sqrt{s}=7$ TeV*, Tech. Rep. ATL-COM-PHYS-2010-695, CERN, Geneva, Aug, 2010.
 - [60] K. Melnikov and F. Petriello, *Electroweak gauge boson production at hadron colliders through $\mathcal{O}(\alpha_s^2)$* , Physical Review D **74** (2006) 114017, [arXiv:hep-ph/0609070 \[hep-ph\]](#).
 - [61] S. Catani, L. Cieri, G. Ferrera, D. de Florian, and M. Grazzini, *Vector boson production at hadron colliders: A Fully exclusive QCD calculation at NNLO*, Physical Review Letters **103** (2009) 082001, [arXiv:0903.2120 \[hep-ph\]](#).
 - [62] ATLAS Collaboration, G. Aad et al., *The ATLAS Simulation Infrastructure*, European Physical Journal C **70** (2010) , [arXiv:1005.4568 \[hep-ex\]](#).
 - [63] S. Jadach, Z. Was, R. Decker, and J. Kühn, *The τ decay library TAUOLA, version 2.4*, Computer Physics Communications **76** (1993) no. 3, 361 – 380.

- [64] Frixione, S. and Webber, B. R., *The MC@NLO 3.3 event generator*, hep-ph/0612272 (2006) , arXiv:hep-ph/0612272.
- [65] G. Corcella, I. Knowles, G. Marchesini, S. Moretti, K. Odagiri, et al., *HERWIG 6: An Event generator for hadron emission reactions with interfering gluons (including supersymmetric processes)*, JHEP **0101** (2001) 010, arXiv:hep-ph/0011363.
- [66] P. Golonka and Z. Was, *PHOTOS Monte Carlo: A Precision tool for QED corrections in Z and W decays*, European Physical Journal C **45** (2006) 97–107, arXiv:hep-ph/0506026.
- [67] A. Martin, W. Stirling, R. Thorne, and G. Watt, *Parton distributions for the LHC*, European Physical Journal C **63** (2009) 189–285, arXiv:0901.0002 [hep-ph].
- [68] P. M. Nadolsky, H.-L. Lai, Q.-H. Cao, J. Huston, J. Pumplin, et al., *Implications of CTEQ global analysis for collider observables*, Physical Review D **78** (2008) 013004, arXiv:0802.0007 [hep-ph].
- [69] ATLAS Collaboration, G. Aad et al., *Charged particle multiplicities in p-p interactions at $\sqrt{s} = 0.9$ and 7 TeV in a diffractive limited phase-space measured with the ATLAS detector at the LHC and new PYTHIA6 tune*, Tech. Rep. ATLAS-CONF-2010-031, CERN, Geneva, Jul, 2010.
- [70] R. Gavin, Y. Li, F. Petriello, and S. Quackenbush, *FEWZ 2.0: A code for hadronic Z production at next-to-next-to-leading order*, Computer Physics Communications **182** (2011) 2388–2403, arXiv:1011.3540 [hep-ph].
- [71] S. Moch and P. Uwer, *Theoretical status and prospects for top-quark pair production at hadron colliders*, Physical Review D **78** (2008) 034003, arXiv:0804.1476 [hep-ph].
- [72] S. Moch and P. Uwer, *Heavy-quark pair production at two loops in QCD*, Nuclear Physics B - Proceedings Supplements **183** (2008) 75–80, arXiv:0807.2794 [hep-ph].
- [73] M. Aliev, H. Lacker, U. Langenfeld, S. Moch, P. Uwer, et al., *HATHOR: HAdronic Top and Heavy quarks crOss section calculatoR*, Computer Physics Communications **182** (2011) 1034–1046, arXiv:1007.1327 [hep-ph].
- [74] S. S. Wilks, *The large-sample distribution of the likelihood ratio for testing composite hypotheses.*, The Annals of Mathematical Statistics **9(1)** (1938) 60–62.
- [75] A. Krasznahorkay, D. Berge, J. Haller, S. Ask, D. Berge, N. Berger, T. Eifert, and A. Hoecker, *SFrame*, A C++ package for high energy physics.

-
- [76] Development of C++ based computer code in collaboration with colleagues at the Institut für Kern- und Teilchenphysik, TU Dresden.
- [77] ATLAS Collaboration Collaboration, G. Aad et al., *Luminosity Determination in pp Collisions at $\sqrt{s} = 7$ TeV Using the ATLAS Detector at the LHC*, European Physical Journal C **71** (2011) 1630, [arXiv:1101.2185 \[hep-ex\]](#).
- [78] M. Baak, C. Guyot, M. Hauschild, R. Hawkings, B. Heinemann, A. Höcker, M. Martinez-Perez, D. Malon, P. Onyisi, and E. Torrence, *Data Quality Status Flags and Good Run Lists for Physics Analysis in ATLAS*, Tech. Rep. ATL-COM-GEN-2009-015, CERN, Geneva, Mar, 2009.
- [79] <https://atlas-datasummary.cern.ch/lumicalc>.
- [80] ATLAS Collaboration, G. Aad et al., *Updated Luminosity Determination in pp Collisions at $\sqrt{s} = 7$ TeV using the ATLAS Detector*, Tech. Rep. ATLAS-CONF-2011-011, CERN, Geneva, Mar, 2011.
- [81] ATLAS Collaboration, G. Aad et al., *Electron performance measurements with the ATLAS detector using the 2010 LHC proton-proton collision data*, European Physical Journal C **72** (2012) 1909, [arXiv:1110.3174 \[hep-ex\]](#).
- [82] Atlas Collaboration, G. Aad et al., *Performance of the Electron and Photon Trigger in p-p Collisions at $\sqrt{s} = 7$ TeV*, Tech. Rep. ATLAS-CONF-2011-114, CERN, Geneva, Aug, 2011.
- [83] ATLAS Collaboration, G. Aad et al., *Data-Quality Requirements and Event Cleaning for Jets and Missing Transverse Energy Reconstruction with the ATLAS Detector in Proton-Proton Collisions at a Center-of-Mass Energy of $\sqrt{s} = 7$ TeV*, Tech. Rep. ATLAS-CONF-2010-038, CERN, Geneva, Jul, 2010.
- [84] M. Aharrouche et al., *Response uniformity of the ATLAS liquid argon electromagnetic calorimeter*, Nuclear Instruments and Methods in Physics Research A **582** (2007), [arXiv:0709.1094 \[physics.ins-det\]](#).
- [85] ATLAS Collaboration, G. Aad et al., *Measurement of the inclusive W^\pm and Z/γ^* cross sections in the electron and muon decay channels in pp collisions at $\sqrt{s} = 7$ TeV with the ATLAS detector*, [arXiv:1109.5141 \[hep-ex\]](#).
- [86] Atlas Collaboration, G. Aad et al., *Muon reconstruction efficiency in reprocessed 2010 LHC proton-proton collision data recorded with the ATLAS detector*, Tech. Rep. ATLAS-CONF-2011-063, CERN, Geneva, Apr, 2011.
- [87] Atlas Collaboration, G. Aad et al., *Muon Momentum Resolution in First Pass Reconstruction of pp Collision Data Recorded by ATLAS in 2010*, Tech. Rep. ATLAS-CONF-2011-046, CERN, Geneva, Mar, 2011.

- [88] Atlas Collaboration, G. Aad et al., *Jet energy scale and its systematic uncertainty in proton-proton collisions at $\sqrt{s} = 7$ TeV in ATLAS 2010 data*, Tech. Rep. ATLAS-CONF-2011-032, CERN, Geneva, Mar, 2011.
- [89] C. Bertella, A. Buckley, S. Chekanov, P. Giovaninni, G. A. Hare, N. Kanaya, D. Kar, S. Menke, J. Nielsen, J. Proudfoot, C. Roda, P. Starovoitov, I. Vivarelli, R. Yoshida, S. Wahrmund, and J. Zhang, *Studies of particle flow using calorimeter clusters in pp collisions at 900 GeV and 7 TeV with the ATLAS detector at the LHC*, Tech. Rep. ATL-COM-PHYS-2010-440, CERN, Geneva, Jun, 2010.
- [90] Atlas Collaboration, G. Aad et al., *In-situ pseudo-rapidity inter-calibration to evaluate jet energy scale uncertainty and calorimeter performance in the forward region*, Tech. Rep. ATLAS-CONF-2010-055, CERN, Geneva, Jul, 2010.
- [91] E. Barberio, M. Beckingham, D. Capriotti, S. Consonni, C. Gumpert, A. Kaczmarska, M. Kobel, S. Kuehn, K. Leonhardt, W. Mader, J. Novakova, X. Prudent, M. Schumacher, T. Shao, and N. Utecht, *Measurement of the cross section $\sigma \times BR(Z^0 \rightarrow \tau\tau)$ in the dilepton channel with the ATLAS detector: Supporting Note*, Tech. Rep. ATL-PHYS-INT-2012-038, CERN, Geneva, Apr, 2012.
- [92] Atlas Collaboration, G. Aad et al., *A combined measurement of the top quark pair production cross-section using dilepton and single-lepton final states*, Tech. Rep. ATLAS-CONF-2011-040, CERN, Geneva, Mar, 2011.
- [93] H1 and ZEUS Collaboration Collaboration, F. Aaron et al., *Combined Measurement and QCD Analysis of the Inclusive $e^+ - p$ Scattering Cross Sections at HERA*, JHEP **1001** (2010) 109, [arXiv:0911.0884 \[hep-ex\]](#).
- [94] ATLAS Collaboration, G. Aad et al., *Observation of $Z \rightarrow \tau\tau \rightarrow e\mu + 4\nu$ with the ATLAS Detector*, Tech. Rep. ATLAS-CONF-2011-045, ATLAS-COM-CONF-2011-040, CERN, Geneva, Mar, 2011.
- [95] CMS Collaboration, S. Chatrchyan et al., *Measurement of the Inclusive Z Cross Section via Decays to Tau Pairs in pp Collisions at $\sqrt{s} = 7$ TeV*, JHEP **1108** (2011) 117, [arXiv:1104.1617 \[hep-ex\]](#).
- [96] ATLAS Collaboration, G. Aad et al., *$Z \rightarrow \tau\tau$ cross section measurement in proton-proton collisions at 7 TeV with the ATLAS experiment*, Tech. Rep. ATLAS-CONF-2012-006, CERN, Geneva, Feb, 2012.
- [97] D. Kirchmeier, *Rekonstruktion des Massenspektrums von neutralen Higgsbosonen*, bachelor thesis, TU Dresden, 2012.
- [98] ATLAS Collaboration, G. Aad et al., *Search for neutral MSSM Higgs bosons decaying to $\tau^+\tau^-$ pairs in proton-proton collisions at $\sqrt{s} = 7$ TeV with the*

- ATLAS detector*, Tech. Rep. ATLAS-CONF-2011-132, CERN, Geneva, Sep, 2011.
- [99] A. Barr, T. Khoo, P. Konar, K. Kong, C. Lester, et al., *Guide to transverse projections and mass-constraining variables*, Physical Review D **84** (2011) 095031, [arXiv:1105.2977 \[hep-ph\]](#).
- [100] P. Konar, K. Kong, and K. T. Matchev, $\sqrt{\hat{s}}_{min}$: *A Global inclusive variable for determining the mass scale of new physics in events with missing energy at hadron colliders*, JHEP **0903** (2009) 085, [arXiv:0812.1042 \[hep-ph\]](#).
- [101] M. Frank, T. Hahn, S. Heinemeyer, W. Hollik, H. Rzehak, et al., *The Higgs Boson Masses and Mixings of the Complex MSSM in the Feynman-Diagrammatic Approach*, JHEP **0702** (2007) 047, [arXiv:hep-ph/0611326 \[hep-ph\]](#).
- [102] K. Pearson, *On the criterion that a given system of derivations from the probable in the case of a correlated system of variables is such that it can be reasonably supposed to have arisen from random sampling*, The London, Edinburgh, and Dublin Philosophical Magazine and Journal of Science **50**(5) (1900) 157–175.
- [103] F. Jamens, *C++ MINUIT User's Guide*.

Danksagung

Hiermit möchte ich mich bei all denen bedanken, die mich beim Erstellen dieser Arbeit unterstützt haben. Mein Dank gilt an erster Stelle meinem Betreuer Michael Kobel für die Herausgabe dieses interessanten Themas und die Möglichkeit in einem solch spannenden Wissenschaftsgebiet mitzuarbeiten. Michael Kobel stand mir mit seiner Unterstützung und Ratschlägen immer hilfreich zur Seite. Weiterhin möchte ich mich bei Wolfgang Mader und Xavier Prudent für die zahlreichen Gespräche und der Klärung wissenschaftlicher Fragen bedanken. Meinem Kollegen Christian Gumpert danke ich für seine vielen Tipps beim Programmieren, Peter Steinbach für die interessanten Diskussionen, sowie Felix Friedrich und Felix Socher für ein kritisches Lesen der Arbeit. Für das motivierende, heitere und angenehme Arbeitsumfeld am Institut möchte ich außerdem auch allen anderen Kollegen meinen Dank aussprechen.

Desweiteren möchte ich mich bei meinen Freunden bedanken, mit denen ich immer wieder eine schöne Zeit verbringen kann.

Mein besonderer Dank gilt meinen Eltern, die mich während meines Studiums finanziell und moralisch unterstützt haben. Desweiteren möchte ich mich bei meiner Schwester Anne bedanken, die mir eine beste Freundin ist.

Ganz spezieller Dank geht an meine Familie; meinen Mann, Thomas, sowie meinen Sohn, Johan. Beide mussten in der finalen Phase der Arbeit oft auf mich verzichten. Sie haben es immer geschafft ein wunderbar ausgleichender Gegenpol zu meiner Arbeit zu sein. Ich danke dir, Thomas, dass du so viel auf dich genommen hast, mich so wunderbar unterstützt und dass du mich immer wieder aufheitern und motivieren kannst.

Eidesstattliche Erklärung

Ich versichere hiermit, die vorliegende Arbeit selbständig und ohne unzulässige Hilfe Dritter angefertigt zu haben. Es wurden keine anderen als die angegeben Hilfsmittel und Quellen verwendet. Resultate, die aus fremden Quellen direkt oder indirekt übernommen wurden, sind als solche kenntlich gemacht worden. Die Arbeit wurde bisher weder im Inland noch im Ausland in gleicher oder ähnlicher Form einer anderen Prüfungsbehörde vorgelegt.

Weiterhin erkenne ich hiermit die Promotionsordnung der Fakultät Mathematik und Naturwissenschaften der Technischen Universität Dresden vom 07.01.2013 an. Die Arbeit wurde unter wissenschaftlicher Betreuung von Prof. Michael Kobel an der TU Dresden angefertigt.

Dresden, den 07.01.2013

Kathrin Kormoll